

Using Low-energy ^8Li Beta-detected NMR to Probe the Magnetism of Transition Metals

by

Terry J. Parolin

B.Sc., McGill University, 2000
M.S., CarnegieMellon University, 2002

A THESIS SUBMITTED IN PARTIAL FULFILLMENT OF
THE REQUIREMENTS FOR THE DEGREE OF

DOCTOR OF PHILOSOPHY

in

The Faculty of Graduate Studies

(Chemistry)

THE UNIVERSITY OF BRITISH COLUMBIA

(Vancouver)

December, 2011

© Terry J. Parolin 2011

Abstract

Low-energy, beta-radiation-detected nuclear magnetic resonance (β -NMR) is applied to probe the magnetism of Au and Pd. The measurements were carried out at the TRIUMF β -NMR facility using optically spin-polarized $^8\text{Li}^+$ as the probe.

The behaviour of $^8\text{Li}^+$ in Au was investigated using samples in the form of a foil and a 100 nm film evaporated onto a MgO (100) substrate. The results are in overall agreement with those obtained previously in Ag, Cu, and Al. Narrow, temperature-independent resonances are observed and assigned to ions stopping in the octahedral interstitial and substitutional lattice sites; the latter appearing only for temperatures above 150 K which is attributed to a thermally-activated site change. The spin-lattice relaxation rate of substitutional site ions is less than half as fast at ambient temperature as that in the other simple metals. The rate is independent of external field for fields greater than 15 mT. A Korringa analysis for the substitutional ions indicates no significant electron enhancement over that of a free electron gas. For all four metals, the enhancements obtained are smaller than those for the host nuclei. No depth dependence was found for the resonances in Au.

The highly exchange-enhanced metal Pd was studied using samples in the form of a foil and a 100 nm film evaporated onto a SrTiO_3 (100) substrate. Strongly temperature-dependent, negative shifts are observed that scale with the temperature dependence of the host susceptibility between room temperature and 110 K. The resonances appear as two partially resolved lines that exhibit similar behaviour with temperature. The linewidths are broad and double upon cooling. The data are indicative of ions stopping in a site of cubic symmetry. The spin-lattice relaxation rate increases

Abstract

linearly with increasing temperature and eventually saturates at higher temperatures, consistent with the prediction from spin fluctuation theory. In contrast to the simple metals, large Korringa enhancements are obtained in this host. Ferromagnetic dynamical scaling is observed to hold above 110 K. Features below this temperature indicate that the Li ions locally induce a further enhancement of the static susceptibility. The temperature dependence of the modified susceptibility is in keeping with the prediction for a weak itinerant ferromagnet just above the Curie temperature; however, there is no evidence of static order.

Preface

A figure in Chapter 2 contains data that has been published: T.J. Parolin, J. Shi, Z. Salman, K.H. Chow, P. Dosanjh, H. Saadaoui, Q. Song, M.D. Hossain, R.F. Kiefl, C.D.P. Levy, M.R. Pearson, and W.A. MacFarlane. NMR of Li Implanted in a Thin Film of Niobium. *Physical Review B* **80**, 174109 (2009). I assisted in much of the data collection, and performed the majority of the data analysis. I wrote the manuscript. Co-authors either assisted in data collection, helped in the execution of the beta-NMR experiments, or prepared/characterized the samples.

A version of Chapter 3 has been published: T.J. Parolin, Z. Salman, K.H. Chow, Q. Song, J. Valiani, H. Saadaoui, A. O'Halloran, M.D. Hossain, T.A. Keeler, R.F. Kiefl, S.R. Kreitzman, C.D.P. Levy, R.I. Miller, G.D. Morris, M.R. Pearson, M. Smadella, D. Wang, M. Xu, and W.A. MacFarlane. High Resolution β -NMR Study of $^8\text{Li}^+$ Implanted in Gold. *Physical Review B* **77**, 214107 (2008). I participated in the collection of some of the data. I carried out all the data analysis, with the exception of a sub-set of data that had been previously analyzed. I was responsible for writing the manuscript and creating the figures. I designed a substrate holder for use in the growth of a sample. Co-authors either assisted in data collection, helped in the execution of the beta-NMR experiments, performed sample characterization, or performed simulations that aided the interpretation of data.

A version of Chapter 4 was presented at a conference and published in the proceedings: T.J. Parolin, Z. Salman, J. Chakhalian, D. Wang, T.A. Keeler, M.D. Hossain, R.F. Kiefl, K.H. Chow, G.D. Morris, R.I. Miller, and W.A. MacFarlane. β -NMR of Palladium Foil. *Physica B* **374-375**, 419–422 (2006) [Proceedings of the 10th International Conference on Muon Spin Rotation, Relaxation and Resonance, Oxford, UK, 2005]. I collected and analyzed all

the data. I wrote the manuscript, and prepared and presented the associated poster. Co-authors either assisted in the collection of additional data or helped in the execution of the beta-NMR experiments.

A version of Chapter 5 has been published: T.J. Parolin, Z. Salman, J. Chakhalian, Q. Song, K.H. Chow, M.D. Hossain, T.A. Keeler, R.F. Kiefl, S.R. Kreitzman, C.D.P. Levy, R.I. Miller, G.D. Morris, M.R. Pearson, H. Saadaoui, D. Wang, and W.A. MacFarlane. β -NMR of Isolated Lithium in Nearly Ferromagnetic Palladium. *Physical Review Letters* **98**, 047601 (2007). I assisted in the collection of the data, performed all the data analysis, conducted sample characterization, and wrote the manuscript. Co-authors either assisted with data collection, helped in the execution of the beta-NMR experiments, prepared samples, or provided additional sample characterization.

The respective publishers grant permission for this material to be incorporated into this thesis.

Table of Contents

Abstract	ii
Preface	iv
Table of Contents	vi
List of Tables	ix
List of Figures	x
Acknowledgments	xii
Dedication	xiii
1 Introduction	1
1.1 Magnetic susceptibilities of transition metals	2
1.2 Conventional NMR of metals	7
1.2.1 Knight shift	9
1.2.2 Spin-lattice relaxation and the Korringa relation	17
1.3 Enhanced paramagnetism and the spin fluctuation model	21
1.3.1 Further notes on the susceptibility of Pd	35
1.4 An alternative: implanted probes	37
2 The β-NMR Technique (at TRIUMF)	48
2.1 Introduction	48
2.2 Production and polarization of ^8Li	48
2.2.1 Isotope production	48
2.2.2 Polarization of the ^8Li nuclear spin	49

Table of Contents

2.3	The β -NMR spectrometer	54
2.3.1	Some comments on beam spot tuning	57
2.4	Data collection and analysis	58
2.4.1	Resonance spectra	59
2.4.2	Spin-lattice relaxation spectra	63
2.5	Additional considerations for resonance spectra	66
2.5.1	Lineshapes and rf power-broadening	66
2.5.2	Demagnetization correction	67
2.5.3	Quadrupole splitting	69
3	β-NMR of ^8Li in Gold	72
3.1	Introduction	72
3.2	Results	72
3.3	Discussion	81
3.4	Conclusions	88
4	^8Li β-NMR of Palladium Foil	89
4.1	Introduction	89
4.2	Results and discussion	89
4.3	Conclusions	97
5	β-NMR of ^8Li in a Bulk Palladium Film	98
5.1	Introduction	98
5.2	Results	98
5.3	Discussion	116
5.4	Conclusions	123
6	Summary and Future Prospects	125
	Bibliography	132
 Appendices		
A	Basics of Beta Decay	152

Table of Contents

A.1	General concepts	152
A.2	Fermi's theory of beta decay	155
A.3	Parity violation in beta decay	160
A.4	Decay of ${}^8\text{Li}$	164
B	Ion Implantation in Metals	166
B.1	General concepts of ion implantation in solids	166
	B.1.1 Damage produced by ion implantation	171
B.2	Simulations of ${}^8\text{Li}^+$ implantation profiles using TRIM.SP . .	173

List of Tables

3.1	Summary of ${}^8\text{Li}^+$ K , A_{hf} , and \mathcal{K} in the simple metals	86
A.1	General classification of beta decay transitions	158
A.2	Physical properties of the ${}^8\text{Li}$ nucleus	165

List of Figures

1.1	Magnetic susceptibilities of selected d metals	8
1.2	Comparison of the temperature dependence of ^{105}K and χ_{Pd}	14
1.3	Sites of cubic symmetry in the fcc lattice	43
2.1	Optical pumping scheme for 8Li and schematic of polarizer layout	51
2.2	Components of the β -NMR spectrometer	56
2.3	Representative resonance spectrum	62
2.4	Representative spin-lattice relaxation spectra	64
2.5	Representative high-field resonance spectra with quadrupole splitting	70
3.1	Spectra recorded in Au foil as a function of rf power at room temperature	74
3.2	Determination of the Knight shift in a Au film	75
3.3	Resonances recorded in Au foil as a function of temperature	77
3.4	Temperature dependence of the Knight shifts, linewidths, and resonance amplitudes in Au foil	78
3.5	Resonances recorded in Au foil at low temperature for low rf power	80
3.6	Comparison of spin-lattice relaxation spectra recorded in a Au film and foil at room temperature	82
4.1	Resonances recorded in Pd foil as a function of temperature	90
4.2	Representative fits to resonances in Pd foil and the resulting Knight shifts as a function of temperature	92

List of Figures

4.3	$K - \chi$ plot for resonances in Pd foil	94
4.4	Temperature dependence of the linewidths and resonance amplitudes recorded in Pd foil	96
5.1	Resonances recorded in a Au-capped 100 nm Pd film as a function of temperature	100
5.2	Representative fits to resonances in the Pd film	101
5.3	Comparison of the temperature dependence of the Knight shifts in the Pd film and foil	103
5.4	$K - \chi$ plot for resonances in the Pd film	105
5.5	Linewidths, and resonance amplitudes and areas in the Pd film as a function of temperature	107
5.6	Linewidths in the Pd film as a function of temperature on a semi-logarithmic scale	109
5.7	Representative spin-lattice relaxation spectra recorded in Pd foil and temperature dependence of $1/T_1T$	111
5.8	Demonstration of ferromagnetic dynamical scaling of K_{av}^c and T_1^{-1} in Pd	113
5.9	Comparison of T_1^{-1} as a function of temperature from ^8Li β -NMR of Pd with that reported from ^{105}Pd NMR	115
5.10	Korringa ratio as a function of temperature in Pd	118
5.11	Temperature dependence of $ K_{av}^c ^{-1}$	121
A.1	Typical energy distribution of beta-electrons	153
A.2	Diagrammatic illustration of parity violation in β -decay	162
B.1	Representative $^8\text{Li}^+$ stopping profile	170
B.2	Representative results of TRIM.SP simulations of $^8\text{Li}^+$ implantation into Pd films	176
B.3	Quadratic interpolation of the range and straggling for $^8\text{Li}^+$ implanted into Pd	177

Acknowledgments

This would not have been possible without the contribution of many people over the course of numerous years. I would be greatly remiss if I did not attempt to acknowledge as many of them as possible.

First, I must acknowledge my supervisor Prof. Andrew MacFarlane for his overall guidance, patience, and staunch commitment to quality. Just as importantly, I would like to thank the members of the beta-NMR collaboration. Profs. Rob Kiefl and Kim Chow for their dedication to the technique, and overall interest in my projects. I especially would like to thank Zaher Salman for teaching me a lot, as well as Gerald Morris for his contribution to the design and continual improvement of the beta-NMR facility at TRIUMF. I would like to thank all of my fellow group members for their assistance in experiments: Susan Song, Dong Wang, Hassan Saadaoui, Masrur Hossein, Todd Keeler, Mike Smadella, and Oren Ofer. I would also like to recognize the numerous TRIUMF staff for their important contributions to the beta-NMR experiments: Phil Levy, Matt Pearson, Rahim Abasalti, Deepak Vyas, Syd Kreitzman, Donald Arseneau, Suzannah Daviel, and Bassam Hitti; as well as the ISAC operations staff.

It's a pleasure for me acknowledge Hanns-Ulrich Habermeier, Gunther Richter, Jacques Chakhalian, Alina Kulpa, and Pinder Dosanjh for preparing samples. Also, Anita Lam for her assistance in X-ray characterization.

I express my thanks to my family for their emotional and financial support over the years. I would also like to thank several friends for similar support— particularly toward the very end when life got real tough: Marta, Matt, Janna, Dolores, Nonie, David, and Ryan. Finally, I owe a big thanks to Prof. Chris Orvig.

Dedication

In memory of my mother and father.

Chapter 1

Introduction

Most elements in the Periodic Table are metals that are characterized by the presence of itinerant conduction electrons, yet they still show a diversity of many other properties. One in particular is magnetism. The origins of magnetic ordering have attracted enormous amounts of theoretical and experimental work over time, originally stemming from the desire to understand the ferromagnetism of the $3d$ elements Fe, Co, and Ni, see e.g., Ref. [1]. Perhaps the ultimate question that needs to be answered when considering magnetism is why and how does it occur in some metals but not in others? When it does occur in a given metal, how does it vary with temperature or pressure; or in the case of alloys, with the concentration of the constituents?

There is a need for experimental techniques that can sensitively measure the magnetism of real materials— whether they be metals or not— with greater precision and sophistication. Specifically, measurements that offer greater insight into magnetism with atomic scale resolution are highly desirable. Nuclear magnetic resonance (NMR) is particularly powerful in this regard; but has its limitations, especially in light of the increasing focus on materials at ever smaller length scales. The work presented here reports on the application of an exotic variant of NMR, called beta-radiation-detected NMR (β -NMR) in which implanted radioactive ions are used to probe the magnetism of materials. The focus is on the application of this technique to the study of metals, in particular Pd, a metal that is an “enhanced” paramagnet. Results are also presented from the β -NMR of Au, a member of the non-magnetic group 11 or “noble metals,” and as such provides a stark contrast to Pd. Taken together, the results demonstrate the utility of this technique for the study of magnetism in metals.

1.1 Magnetic susceptibilities of transition metals

The early theories of the electronic structure of metals were based on the independent electron approximation[2]. In this approach, a single electron is viewed as moving in the average potential of all the other electrons. This avoids having to treat the electrostatic Coulomb interaction amongst all the electrons in a solid, and so is an obvious simplifying approximation. Actually, the approximation is rather sufficient in describing properties of metals, but noticeably fails in the case of a partially filled d (or f) band where electron-electron interactions can generate magnetic ordering. This is illustrated by the discussion in Sec. 1.3 on enhanced paramagnetism. However, here, the general mechanisms of magnetic susceptibility of metals is discussed, largely on the basis of an independent electron gas.

The susceptibility of a material is defined as the ratio of the magnetization M induced by an external magnetic field H ,

$$\chi = \frac{M}{H}. \quad (1.1)$$

Diamagnetic refers to a negative value of χ , paramagnetic to a positive one.

The interest here is in the susceptibility of the conduction electrons in the d transition metals in general, i.e., excluding those that order ferromagnetically: Fe, Co, Ni, and some lanthanides. Unlike a free ion, electrons in metals are itinerant and respond collectively[2]. For a free, quantum-degenerate electron gas, the magnetization is essentially temperature-independent[2, 3]. This can be seen by contrasting the temperature-independent χ of a metal with the high-temperature susceptibility given by Curie's law for *ions* to the electrons of a metal[2]:

$$\chi = \frac{N_A(g_e\mu_B)^2}{3} \frac{J(J+1)}{k_B T}. \quad (1.2)$$

For the electron, $J = \frac{1}{2}$, and taking g_e to be 2, the above expression gives $\chi = N_A\mu_B^2/k_B T$. Like thermal excitations, the external field can only interact with the conduction electrons that are within $k_B T$ of the Fermi level, so the

1.1. Magnetic susceptibilities of transition metals

fraction of electrons that contribute to χ is[3] T/T_F . Scaling the result for χ by this ratio, the magnetization of the conduction electrons thus follows[3]

$$M \approx \frac{N_A \mu_B^2}{k_B T_F} H, \quad (1.3)$$

which is independent of temperature.

An accurate expression for the susceptibility of the conduction electrons was given by Pauli (who correctly treated them with Fermi-Dirac statistics)[2, 3], and so is termed the Pauli spin susceptibility χ_P , or Pauli paramagnetism. A simple but useful way to derive it[4] is to neglect the orbital response of the electrons to the external field (i.e., consider the spin only)[2, 4]. Then, to lowest order, the effect of the applied field is to shift the relative energy distribution of electrons with up and down spins[4]. The total energy of the electrons is now the kinetic energy plus the magnetic contribution of $\pm\mu_B H$ [3]. The electrons will adjust such that the chemical potential of the spin up and spin down electrons will be equal, i.e., the bands will have the same E_F [3, 4]. Because the gyromagnetic ratio of the electron is negative, there will be a net increase in the density of electron orbitals anti-parallel to the field, resulting in a moment parallel to the field[3, 4]. If $N_{+(-)}$ denotes the concentration of electrons with moments parallel(anti-parallel), then the magnetization density is[2, 3]

$$M = \mu_B(N_+ - N_-). \quad (1.4)$$

In terms of the shifted density of states $\mathcal{D}(E)$, the electron concentrations are given by

$$N_{\pm} = \int \mathcal{D}_{\pm}(E) f(E) dE, \quad (1.5)$$

where $f(E)$ is the Fermi function. Since the Fermi energy sets the scale for the change in $\mathcal{D}(E)$, and $\mu_B H \sim 10^{-4} E_F$ (even for Tesla fields) the density of states can be expanded leading to[2]

$$N_{\pm} = \frac{1}{2} \int \mathcal{D}(E) f(E) dE \pm \frac{1}{2} \mu_B H \int \mathcal{D}'(E) f(E) dE, \quad (1.6)$$

1.1. Magnetic susceptibilities of transition metals

where $\mathcal{D}'(E)$ represents the first derivative. Substituting into Eq. (1.4), the magnetization density is thus[2]

$$M = \mu_B^2 H \int \mathcal{D}'(E) f(E) dE, \quad (1.7)$$

which can be recast as

$$M = \mu_B^2 H \int \mathcal{D}(E) \left(-\frac{\partial f}{\partial E} \right) dE. \quad (1.8)$$

As $T \rightarrow 0$, $f(E)$ approaches an inverted step function at E_F [4, 5], and its derivative is well approximated by the negative of the Dirac delta-function: $-\partial f/\partial E = \delta(E - E_F)$, which leads to[2, 4, 5]

$$M = \mu_B^2 H \mathcal{D}(E_F). \quad (1.9)$$

By means of Eq. (1.1) the Pauli susceptibility is thus

$$\chi_P = \mu_B^2 \mathcal{D}(E_F); \quad (1.10)$$

i.e., it is linearly proportional to the density of states at the Fermi level.¹

The above derivation is made for $T \ll T_F$ — basically, practical temperatures[5]— and is valid until $T \approx T_F \sim 10^4$ K[2].

In the noble metals, like Cu, Ag, and Au, the Fermi energy lies just above the d band in the s band; χ_P is accordingly small in these metals[4]. In fact, *in general*, χ_P for most metals is quite small in comparison to the susceptibility of free ions. For an ion with unpaired spins, the tendency for spin moment alignment with a field is reduced by thermal disorder (Curie's law); while the paramagnetic susceptibility of the conduction electrons is greatly suppressed by the exclusion principle[2]. For instance, [Eq. (1.2)] for a paramagnetic ion of spin $\frac{1}{2}$ at room temperature, $\chi \sim 10^{-3}$ emu/mol; while for typical transition metals [Eq. (1.3)], $\chi_P \sim 10^{-5}$ emu/mol, i.e., hundreds of times smaller[2].

The magnetization of a Curie-law paramagnet follows an inverse- T de-

¹The density of states at the Fermi level will be denoted by \mathcal{D}_F .

pendence; while, in contrast, it was stated above that the magnetization of metals is essentially independent of T . The latter is an oversimplification; many metals do show a temperature-dependent χ_P , although often, but not always, over ranges of absolute T spanning a couple orders of magnitude. Since the d band is narrow with a higher density of states and $\mathcal{D}_F \sim k_B T$ when the Fermi level is in this band, χ_P is not only larger than for metals where E_F lies in the s band, but it also leads to a T -dependent χ_P [4]. The temperature dependence of χ_P is a consequence of the structure in the $\mathcal{D}^d(E)$, as well as electron interactions (Sec. 1.3).

In addition to χ_P , there are other sources of magnetism in a transition metal that arise from the orbital susceptibility of the electrons χ_{orb} .² Depending on the metal, this susceptibility may be negligible or considerable in relation to the spin susceptibility. In the above discussion of χ_P , only the spin of the electrons was considered, and the charge was neglected. However, the external field couples to the orbital motion of the electronic charge and this gives rise to a diamagnetic response, i.e., M that is antiparallel to H [2]. For a *free* electron gas, Landau found[2, 3, 4]

$$\chi_L = -\frac{1}{3}\chi_P; \tag{1.11}$$

termed the Landau diamagnetism.

The energy of these orbital levels can be found only by using a quantum mechanical approach (as Landau did for the free electron gas); however, evaluating the orbital motion of electrons in a periodic potential of a crystalline lattice, i.e., Bloch electrons, in the presence of the applied field is quite complicated[2, 4, 6, 7]. The potential can alter the orbital motion of the electrons, sometimes generating a paramagnetic contribution, and also sometimes introducing a contribution from spin-orbit (s-o) coupling[6]. Unlike χ_P , which is independent of applied field, the orbital effects are second-order in field. While the above Landau diamagnetism can be considered appropriate for nearly free electrons like those of the s band, when a realis-

²The paramagnetism arising from the magnetic moments of the nuclei is $\sim 10^{-3}$ times smaller than that from the electrons[3, 9], and is negligible.

tic d band structure is considered, the orbital susceptibility may acquire a paramagnetic contribution if the d band is partially filled. This effect (first pointed out by Kubo and Obata[8]) can be considered as the itinerant electron analog of the van Vleck susceptibility of ions[4, 5]: the applied field causes interband mixing of the electronic states below and above the Fermi level[4, 9], similar to the mixing of low lying excited states into the ground state by the applied field in free ions[2, 4]. This contribution, denoted χ_{vv} , is thus greatest when the Fermi level lies in the middle of the d band, as there are then many states which can be combined by the applied field[7]. As outlined below, NMR provides one means of separating the contributions of χ_{vv} and χ_P from the total susceptibility. Another is a magnetomechanical technique[9]. Such measurements found large values of the orbital paramagnetism relative to the spin magnetism in metals like V and Nb, and as expected, the opposite for the metals Pt and Pd[9, 10].

Calculations of χ_{orb} have been performed for transition metals by a generalization of the complicated expressions in combination with calculated band structures, including the effects of s-o coupling[7, 11]. The latter is a relativistic correction to the orbital susceptibility. The s-o coupling is generally regarded as an atomic property, and so it is often assumed that atomic values largely apply to the solid state. Its importance for the d metals thus follows that expected from trends in atomic s-o coupling down a group, i.e., it is weak in Ni, moderate in Pd, and strongest in Pt[7] as a consequence of the increasing relativistic motion of electrons with increasing nuclear charge. In addition to χ_L and χ_{vv} and its s-o contributions, the orbital susceptibility also includes a diamagnetic contribution χ_{dia} from the filled electron levels of the cores of the ions (or atoms) in the lattice[5, 7, 9, 10, 11]. This diamagnetism is analogous to that of the filled electron levels in a paramagnetic ion, and is termed the Langevin (or Larmor) susceptibility[2, 5]. In many cases, the diamagnetic and paramagnetic parts of χ_{orb} compensate, and χ_{orb} is overall small[7, 10, 11].

In considering the paramagnetism of a metal where the Fermi level lies in the d band, the total susceptibility is conventionally decomposed into the

sum of four major contributions[12], namely

$$\chi(T) = \chi_s + \chi_d(T) + \chi_{vv} + \chi_{\text{dia}}, \quad (1.12)$$

where χ_P has been split into individual contributions from the s and d bands. Only that of the d band explicitly varies with T . The other three contributions are independent of T , although in some cases χ_{vv} can show a dependence on T [4]. It is emphasized that the above is an approximation which is valid in the limit of completely independent s and d bands, i.e., in the limit of vanishing $s-d$ hybridization. In spite of this, it is at least a good starting point for the discussion of the susceptibility of transition metals. The total susceptibilities of select d metals as a function of temperature are displayed in Fig. 1.1 showing a representative range of behaviour. In the group 11 (noble) metals where the d band is completely filled and \mathcal{D}_F lies in the sp band, χ_P is small compared to the diamagnetic contribution and the overall observed susceptibility is negative[1, 7]. In stark contrast, the susceptibility of Pd is quite large. As the total contribution from χ_{orb} is at most a few percent, the large paramagnetism is due to the contribution of the d electrons and makes Pd rather unique among the transition metals. The origin of this large paramagnetism is discussed in greater detail in Sec. 1.3 below.

1.2 Conventional NMR of metals

As in the study of molecules, conventional NMR has been an invaluable tool in advancing the knowledge of the magnetic properties of solids. This is particularly true because it is a technique that can yield information about a sample on a local, or atomic, level. Two important experimental quantities measured by NMR are the frequency shift, and the (longitudinal) spin-lattice relaxation rate. These are outlined below with reference to examples of NMR in transition metals.

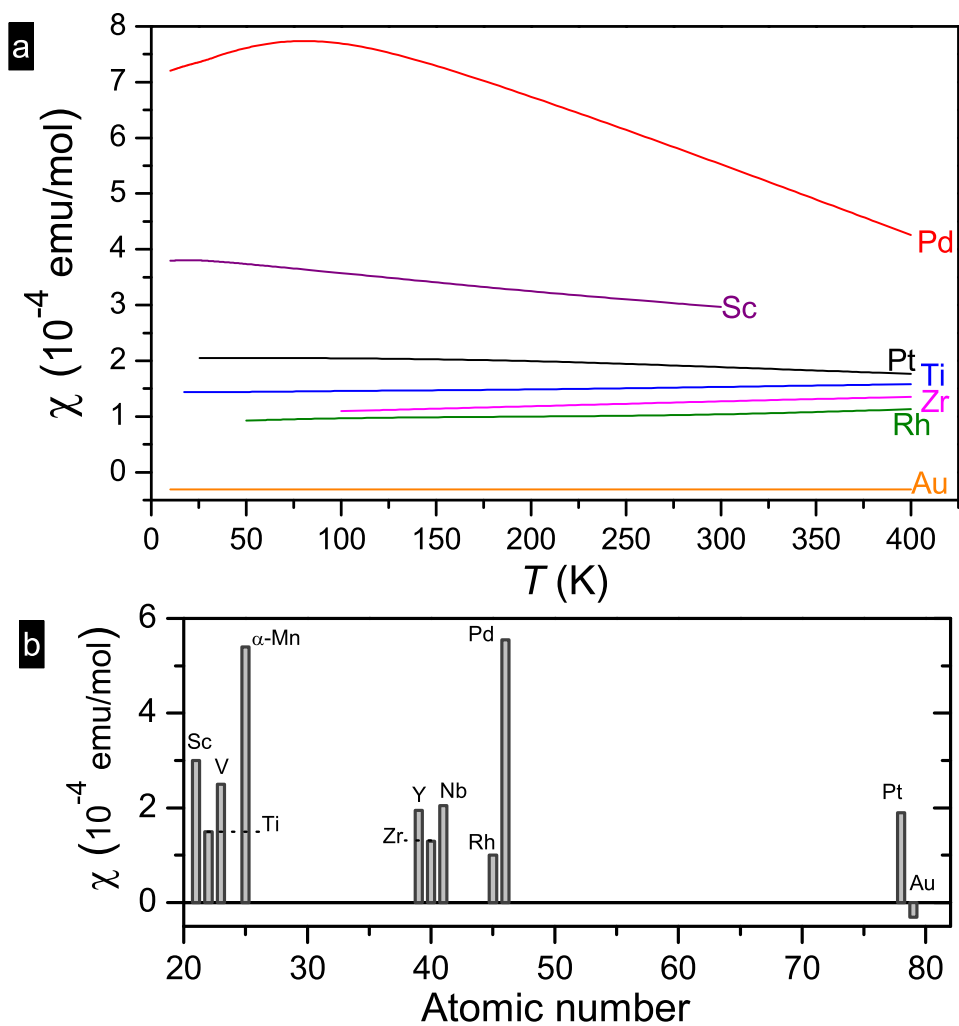


Figure 1.1: (a) Temperature dependence of the susceptibility of selected d metals: Ti and Rh, Ref. [3]; Pd, Refs. [13, 14, 15]; Sc, Refs. [16, 17]; Zr, Refs. [3, 4]; Pt, Ref. [18]; Au, Ref. [1]. (b) Comparison of the *room temperature* susceptibilities of the metals in (a), plus some others with large χ [4].

1.2.1 Knight shift

In conventional NMR, application of a static external magnetic field H_0 causes the degenerate nuclear magnetic levels of a spin $I > 0$ nucleus to be split into $(2I + 1)$ magnetic sublevels[2]; this is known as the nuclear Zeeman splitting. The levels can be designated by the nuclear spin quantum number m_I , with the axis of quantization taken to be along the direction of H_0 . The splitting between each sublevel is $\Delta E_{m_I} = \gamma_n \hbar H_0$, where γ_n is the nuclear gyromagnetic ratio which is proportional to the nuclear magnetic moment. Application of an alternating, radio frequency, magnetic field H_1 transverse to H_0 results in resonant absorption that is detected to give a spectrum[2]. The allowed transitions occur for $\Delta m_I = \pm 1$, at an angular frequency[20]

$$\hbar\omega = \Delta E_{m_I} = \hbar\gamma_n H_0. \quad (1.13)$$

In a metal, the nuclei are found to resonate at frequencies shifted from Larmor frequency $\nu_L (= \gamma_n H_0)$ for the free nucleus due to the interaction with the conduction electrons. This shift was first reported on by W. Knight and co-workers[22], and so is termed the Knight shift K [5, 12, 19, 20, 21]. It arises from the conduction electron (para)magnetism through the Fermi contact interaction, i.e., χ_P [Eq. (1.10)] effectively producing an additional field at the nucleus that adds to the applied field. This is a quantum mechanical interaction, since it originates from two particles being “at the same place”[5]. As such, this extra field experienced by the nucleus is termed the contact hyperfine (hf) field, and it is usually an order of magnitude larger than the chemical shifts observed in metal salts[20].

The Hamiltonian for the Fermi contact interaction for nuclear spin \mathbf{I}_i with electron spin \mathbf{S}_j reads

$$\mathcal{H}_{e-n} = \frac{8\pi}{3} \gamma_e \gamma_n \hbar^2 \sum_{i,j} \mathbf{I}_i \cdot \mathbf{S}_j \delta(\mathbf{r}_{ij}), \quad (1.14)$$

where γ_e is the electronic gyromagnetic ratio, and \mathbf{r}_{ij} are the position coordinates of the nucleus and electron. Since it is only electrons of s symmetry

1.2. Conventional NMR of metals

that have a finite probability of being found at the nucleus (i.e., they have no node at the nucleus), the hyperfine field from the contact interaction involves the square of the s -wavefunction at the nucleus $\psi_s(0)$ normalized to the atomic volume, averaged over electrons on the Fermi surface (and so this interaction is intrinsically isotropic);

$$K = \frac{8\pi}{3} \langle |\psi_s(0)|^2 \rangle_F \chi_P. \quad (1.15)$$

For this result, the Knight shift is defined as a fractional shift, $K \equiv \Delta H/H_0$; where ΔH is the extra field at the nucleus, and the dependence on H_0 is thus normalized out. In terms of experimentally measured frequencies,

$$K = \frac{\nu}{\nu_0} - 1. \quad (1.16)$$

Here ν is the resonance frequency in the metal, and ν_0 is the reference frequency relative to which K is determined. It is therefore important that the reference be nonmetallic and nonmagnetic. Usually, diamagnetic ionic salts (or solutions of them) of the nucleus of interest are used; ν_0 is then typically very close to ν_L , differing by the chemical shift which is small in comparison to shifts arising from the paramagnetic contributions of the conduction electrons. Values of K are typically expressed in per cent or parts per million (ppm), depending on their magnitude.

Eq. (1.15) can be re-expressed in terms of a constant times the susceptibility

$$K = A_{\text{hf}} \chi_i. \quad (1.17)$$

The term A_{hf} is the hyperfine coupling constant that represents the additional hf field at the nucleus. The above equation indicates that a knowledge of both the electronic magnetic susceptibility and the extent of its coupling to the nucleus is required to quantitatively understand the Knight shifts in metals. Often A_{hf} is estimated from the hf splitting measured in the free atom, but this is at best a first approximation. In principle, χ can be measured by magnetometry, e.g., using a SQUID, or estimated from values of the electronic contribution to the specific heat; however, such measurements

give the macroscopic, bulk susceptibility which contains other contributions beside χ_P . The attractiveness of the NMR technique is that it can probe samples at the microscopic level, and reveal the differing hf fields experienced by various nuclei in the material.

In Eq. (1.17), the Pauli susceptibility has been replaced by χ_i , since in the study of transition metals, the measured shift is decomposed into contributions from the various terms in Eq. (1.12); each with a distinct coupling constant. As previously mentioned, the diamagnetic component is small in comparison to the others, and often assumed to be of equivalent magnitude to the atomic chemical shift of the diamagnetic reference salt (although deviations are not uncommon)[5]. Equations (1.12) and (1.17) indicate that for metals with filled d bands like the simple metals, K will be essentially temperature-independent. In metals with near half-filled d bands (e.g., V and Nb), the orbital paramagnetic susceptibility is large and gives the dominant contribution to the observed shift[12, 21]. This shift may be T -dependent with $\partial K(T)/\partial\chi(T)$ usually positive[12]. In these cases, the contributions from χ_s and χ_d largely cancel[12, 23]. This arises from the mechanism by which χ_d affects K , and is crucial for metals with nearly filled d bands (e.g., Pt and Pd); the shifts are observed to be strongly T -dependent and *negative*[12, 21].

The d wavefunctions vanish at the nucleus, so their effect on the spin density is due to the mechanism of “core-polarization”[12], whereby the spin polarization of the unfilled d shells is mixed into the core s electron wavefunctions. An analogous situation is encountered for hf fields of atoms or paramagnetic ions, i.e., a configuration interaction that mixes excited states into the ground state[12, 21, 24, 25]. This indirect polarization takes place through an electron-exchange interaction like that occurring between electrons in the d band that is responsible for the enhanced susceptibility of Pd discussed below. This is like saying that s electrons with spin parallel to the polarized d electrons experience a reduced electrostatic repulsion due to the Pauli principle and are overall less repelled by one another than by electrons with spins antiparallel[24]. The result is differing spatial distributions of the core electrons of opposite spin; s electrons with spins parallel to the d elec-

trons are attracted away from the nucleus, indirectly giving rise to a negative spin density (i.e., antiparallel to the d polarization) at the origin producing a negative contact hf coupling[21, 24]. The small number of valence (i.e., non-core) s electrons are polarized indirectly by the d spins also, but give a positive contribution at the origin[24]. The contribution from χ_s of the valence electrons is therefore considered the *direct* contact interaction, and yields a positive shift. As \mathcal{D}_F^s is small (and practically T -independent), the contribution from $\chi_d(T)$ can cancel or exceed the direct contribution[12]; this is especially true in transition metals with large susceptibilities, like Pt and Pd.

The dipolar coupling between the electron and nuclear spins can add to the field at the nucleus, and hence to the shift. The contribution from the coupling of the nuclear moment to the electron spin of a d or p orbital electron can thus be anisotropic and depends on the direction of H_0 relative to the crystalline axes[12, 20, 21]. For cubic metals, these couplings gives no contribution, but may be non-zero at sites where the symmetry of the spin density is reduced. As conventional NMR is frequently performed on powdered samples rather than single crystals, any anisotropy of the electronic dipolar-nuclear coupling can give rise to structure of the resonance line. However, the dipolar coupling field is normally an order of magnitude smaller than the contact or core-polarization contributions, and generally produces a broadening of the resonance[20, 21].

The temperature dependence of K from ^{195}Pt NMR was reported by Clogston *et al.*[26]. The measured shifts were used in combination with the measured total χ of Pt to separate the different contributions in Eq. (1.12). They observed a linear dependence of K with χ (from room T and below) and displayed this in a $K - \chi$ plot (or ‘‘Jaccarino-Clogston’’ plot) in which T is an implicit parameter[12]. The shifts³ were found to be negative and $\sim -3\%$ in the T range investigated. The analysis thus involved

³These early metal NMR measurements were performed in field-swept mode, i.e., the field was varied with the transverse radio-frequency field held constant. The K values correspond to Eq. (1.16) with the frequencies replaced by the resonant fields for the metal sample and the reference.

estimations of χ_s and χ_{dia} . The s electrons were treated as free electron-like, and $s - d$ (and $s - s$) exchange interactions were neglected. Accordingly, χ_s was taken to be small and T -independent; χ_{dia} was estimated on the basis of the susceptibilities of Pt salts; χ_{vv} was determined by a method of extrapolation of the data on the $K - \chi$ plot, and found to contribute $\sim \frac{1}{5}$ of the observed K , but positive in magnitude (and not dependent on T). Overall, the negative χ_{dia} together with the small, positive χ_s nearly cancel the contribution from χ_{vv} , an indication that the observed shifts, with $\partial K(T)/\partial \chi(T) < 0$, must be dominated by the d spins. This was taken as clear support for the model of polarization of the core s electrons by the d spins as the mechanism for the large, negative, T -dependent shifts in metals with nearly filled d bands[12]. In a later NMR study of Pt a $K - \chi$ plot analysis was performed for temperatures extending to ~ 1300 K[27] and the results were in agreement with the earlier report[26], especially with respect to the cancellation of the diamagnetic and orbital paramagnetic contributions, reinforcing the importance of the d electrons.

Subsequently, Seitchik, Gossard, and Jaccarino performed a similar study of Pd metal, the first observation of ^{105}Pd NMR[14]. As in Pt, T -dependent, negative Knight shifts were observed that scaled linearly with the susceptibility, including its maximum at around 85 K (see Fig. 1.2). The Knight shift was observed to vary between -3% to -4% over the T range; however, unlike in the analysis for Pt, the nuclear moment of ^{105}Pd was not known very accurately at the time, and so the zero of shift could not be determined with great certainty. This precluded the graphical determination of χ_{vv} from the $K - \chi$ plot. Instead, it was estimated to be $\sim 25 \times 10^{-6}$ emu/mol, along with χ_s (6×10^{-6} emu/mol) and χ_{dia} (-25×10^{-6} emu/mol). Their estimated value of the orbital susceptibility is similar to the values later reported[7, 9]; however, more recent fully relativistic calculations[11] put $\chi_{\text{vv}} \sim 40 \times 10^{-6}$ emu/mol.

The sum of the above three estimates amount to just $\sim 1\%$ of the total χ of Pd. Nonetheless, χ_s and χ_{vv} were determined to give a contribution of +0.36% *each* to the observed K , independent of T . Thus, analogous to Pt, it was concluded that the enhanced d spin contribution dominates the

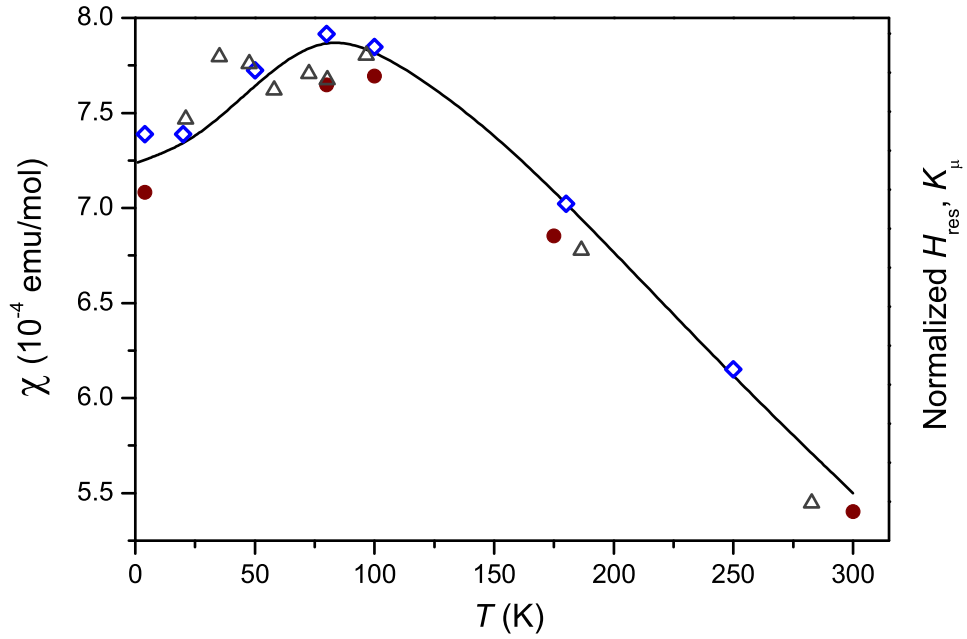


Figure 1.2: Temperature dependence of ^{105}Pd NMR resonant fields superimposed on the susceptibility of pure Pd: (\bullet), Refs. [14, 21]; (\diamond), Ref. [32]. The temperature dependence of the positive muon Knight shift in Pd is also shown (\triangle), Ref. [198]. In order to display all the experimental data on the same plot, the NMR resonant fields and muon shifts have been normalized to their respective values at room temperature.

observed Knight shifts through core-polarization and is responsible for the temperature dependence of K . Although χ_s is a tiny fraction of the total χ , A_{hf}^s was evaluated to be an order of magnitude larger than A_{hf}^d , so the direct contact contribution is not entirely negligible.

More recently, Krieger and Voitländer performed a calculation of K for Pd[28]. They evaluated the contribution from all s, p , and d levels and indeed found that polarization of core electrons gives the majority, negative contribution, as the direct contact contribution is +0.18%. Their total K (for $T = 0$) is -3.34%, which is adequate compared with the 4 K experimental result of -4.1(5)%[21] considering the uncertainty in the zero of shift. However, no (positive) orbital contribution to K was included in the calculations of Ref. [28], which only reduces the agreement with experiment.

The hyperfine field, as a low energy property, is a quantity that provides a strict test for first-principles calculations. Generally, calculated values are smaller than experimental ones. The dominance of the core-polarization contribution in strong paramagnets is also found in magnetically ordered metals, like Fe. Reducing the discrepancy with experiment requires treatment of this contribution beyond what is typically achievable with common *ab initio* methods[11, 29, 30]. Additionally, $s - d$ hybridization is increased in the $4d$ and $5d$ metals, which can make a contribution irrespective of the exchange coupling. For instance, Terakura *et al.* pointed out that the direct contact contribution in Pd should be both larger and negative ($\sim -1\%$) due to $s - d$ hybridization[31].

Takigawa and Yasuoka also carried out measurements of the resonant fields in metallic Pd, but for more T points[32] (select values from their measurements are also shown in Fig. 1.2). They report results very similar to those of Seitchik *et al.* upon decomposing the shift into the various contributions. Just as in the earlier study, they considered the dominant contribution to be from the core-polarization from d electrons and allowed for this to be the only T -dependent term. Using values of the hyperfine fields from first-principles band structure calculations[33], they estimated the direct contribution to be +0.12%, but used a very similar value for the diamagnetic contribution and the same (+0.36%) orbital contribution as

Seitchik *et al.*[14]. From the T -dependence of their shifts, these authors[32] determined a comparable d spin (i.e., core-polarization) hf coupling, but a smaller direct coupling than in Ref. [14]; however, the coupling constants extracted agree with the earlier report that A_{hf}^s is an order of magnitude larger than A_{hf}^d .

In considering more appropriate values for the ^{105}Pd reference frequency, van der Klink and Brom[5] performed an analysis of the contributions to K that leads to a total shift of -3.44%. They employ a direct contribution based on requiring A_{hf}^s be of similar order to that of Pt, and obtain +0.62% with an orbital contribution of +0.36%. The latter value is the same as in the earlier two studies[14, 32], but the direct part required is a factor of 2 larger. Although this is the most modern analysis, estimations based on comparison to values for Pt are questionable; a larger direct contribution is expected for increased $s - d$ hybridization.

Given that there is really only “one” (i.e., total) χ , it is apparent that any such decomposition of experimental K ’s requires considerable estimation by means of calculation or comparison to other metals. However, a rather clear consensus on the sign and order of magnitude for the three contributions (s , d , and orbital) is broadly found.

NMR has also been extensively applied to the study of metallic alloys. In particular, those formed from a magnetic impurity in an otherwise non-magnetically ordered host (e.g., CuFe) have been of interest with respect to the mechanism(s) and degree of polarization of the host by the magnetic moment of the impurities[34]. These systems are not discussed in detail here, but one result from the NMR of such alloys is worth mentioning in regard to adventitious contamination of a metal sample by dilute, magnetic impurities: K of the host nuclei is not affected by the presence of the magnetic impurities[26, 35]; the resonance line is instead broadened proportional to the impurity susceptibility. This also holds for a host with an enhanced susceptibility, like Pt, as evidenced from ^{195}Pt NMR in samples alloyed with dilute (< 0.1 at.%) Co; the shift was not found to vary, while the linewidth showed a linear increase with increasing Co concentration[36]. In such (dilute) systems, the linewidth of the host resonance was calculated

to approach a Lorentzian lineshape[37], which was indeed observed in the NMR of *CuMn*[35] and *PtCo*[36] alloys.

1.2.2 Spin-lattice relaxation and the Korringa relation

In order to discuss the spin-lattice relaxation, the generalized magnetic susceptibility must be recalled:

$$\chi(\mathbf{q}, \omega) = \chi'(\mathbf{q}, \omega) + i\chi''(\mathbf{q}, \omega), \quad (1.18)$$

where $\chi'(\mathbf{q}, \omega)$ and $\chi''(\mathbf{q}, \omega)$ are the real and imaginary components, respectively. $\chi(\mathbf{q}, \omega)$ defines the response of the system to a generalized exciting field that varies periodically with angular frequency ω and with a spatially periodic fluctuation of wavevector \mathbf{q} ($|\mathbf{q}| = 2\pi/\lambda_i$). The uniform, static limit of the real component is identified with the Pauli susceptibility (of non-interacting electrons), cf. Eq. (1.10),

$$\chi'(\mathbf{0}, 0) = \frac{1}{2}\gamma_e^2\hbar^2\mathcal{D}_F. \quad (1.19)$$

As discussed above, the Knight shift is proportional to the real component, while it is the imaginary (dissipative) component that is important for the spin-lattice relaxation rate.

For transition metals, the Fermi contact interaction produces a large hf field at the nucleus, and so the spin-lattice relaxation process occurs predominantly through this interaction. Specifically, the longitudinal relaxation of the nuclear magnetization (in non-magnetically ordered metals) that arises from transverse fluctuations associated with Eq. (1.14). The general mechanism is that of mutual spin-flip scattering of an electron off the nucleus. A Bloch s electron in the initial state of wave vector \mathbf{k} with spin orientation s_e undergoes a transition to the final state \mathbf{k}', s'_e , and the nucleus simultaneously makes a transition from state m_I to m'_I [19, 20]. The nucleus gives the electron an energy small in comparison with $k_B T$, so only electrons near E_F with empty states nearby in energy can participate in the relaxation[20]. The relaxation rate thus depends on temperature through the width of the

“tail” of the Fermi distribution[20]. The number of available states increases as the width with increasing T , so the rate is directly proportional to T . The observation of a spin relaxation linear with temperature is one important method of establishing that a material (i.e., solid) is metallic[38].

The transverse fluctuations on which the relaxation rate depend are given by an integral over wavevectors of the imaginary part of the dynamical susceptibility[12, 39, 40],

$$\frac{1}{T_1} = \frac{32}{9} \gamma_n^2 \langle |\psi_s(0)|^2 \rangle_F^2 k_B T \frac{1}{\omega_L} \int \mathbf{q}^2 \chi''(\mathbf{q}, \omega_L) d\mathbf{q}. \quad (1.20)$$

In the above expression, the frequency of interest is specifically the nuclear Larmor frequency, which corresponds to the low frequency limit for typical electronic magnetic fluctuations. The integral can be evaluated for a free electron gas:

$$\frac{1}{\omega_L} \int \mathbf{q}^2 \chi''(\mathbf{q}, \omega_L) d\mathbf{q} = 2\pi^3 \gamma_e^2 \hbar^3 \mathcal{D}_F^2. \quad (1.21)$$

Substitution of this result into Eq. (1.20) results in

$$\frac{1}{T_1 T} = \frac{64}{9} \pi^3 \hbar^3 k_B \gamma_e^2 \gamma_n^2 \langle |\psi_s(0)|^2 \rangle_F^2 \mathcal{D}_F^2. \quad (1.22)$$

Since the relaxation depends on the electron-nuclear contact interaction, $\langle |\psi_s(0)|^2 \rangle_F$ is the same as that appearing in Eq. (1.15),

$$\langle |\psi_s(0)|^2 \rangle_F^2 = \frac{9}{64\pi^2} \frac{K^2}{\chi_P^2}. \quad (1.23)$$

Inserting this quantity into Eq. (1.22) gives

$$\frac{1}{T_1 T} = K^2 k_B \pi \hbar^3 \gamma_e^2 \gamma_n^2 \frac{\mathcal{D}_F^2}{\chi_P^2}. \quad (1.24)$$

Using χ_P given by $\chi'(\mathbf{0}, 0)$ from Eq. (1.19) yields a very useful relation in NMR:

$$T_1 T = \frac{\hbar}{4\pi k_B K^2} \left(\frac{\gamma_e}{\gamma_n} \right)^2. \quad (1.25)$$

The above expression shows that the relaxation rate due to the conduction

electrons is inversely proportional to the square of the shift, or by extension [Eq. (1.17)], to the square of the hf coupling. Eq. (1.25) is known as the Korringa relation[5, 19, 20, 21, 41], which upon re-arrangement can be expressed as a dimensionless ratio

$$\mathcal{K} = \frac{T_1 T K^2}{S_0}, \quad (1.26)$$

where S_0 is a single constant into which all the constants in Eq. (1.25) have been incorporated, and is specific to a given nucleus (through γ_n).

The Korringa relation provides a convenient way to estimate the shift given a measurement of the relaxation rate, or vice-versa[20]; however, it is emphasized that the relation is strictly valid for *non*-interacting electrons. In such an ideal case the ratio \mathcal{K} as defined in Eq. (1.26) is unity, but for real metals deviations are observed. These are often attributed to the breakdown of the relation due to neglect of electron-electron interactions on the dynamic susceptibility[5], although only the electron-nuclear mechanism is considered, so the neglect of other relaxation processes may also contribute to deviations[20]. Values of \mathcal{K} different from 1 are found even for the “simple” metals such as the alkalis or the noble metals[5, 20]. For instance, \mathcal{K} is 1.6 for Li, and 1.9 for Cu[21]. For metals with strong electronic correlations, significant deviations from ideality are found; e.g., for Pd $\mathcal{K} = 9.4$ [21]. In this regard, \mathcal{K} is frequently used as a phenomenological measure of the tendency toward magnetic ordering. As defined in Eq. (1.26), $\mathcal{K} > 1$ is taken to be indicative of ferromagnetic correlations, and $\mathcal{K} < 1$ of anti-ferromagnetic correlations.⁴

An additional aspect of the spin-lattice relaxation rate of the transition metals (those with E_F in the d band) that must be taken into account is the orbital degeneracy factor (viz. e_g and t_{2g} levels)[12, 42]. This factor, denoted F_d , represents a reduction, or “inhibition,” of the relaxation due to

⁴Often the inverse of Eq. (1.26) is used, in which case the type of ordering attributed to the magnitude of \mathcal{K} is reversed.

the core polarization by an amount

$$F_d = \frac{1}{3}f^2 + \frac{1}{2}(1-f)^2, \quad (1.27)$$

where, here, f is the fractional character of the triply degenerate orbital at E_F ; F_d correspondingly varies from 0.2 to 0.5. For Pd, calculations[33] give $f = 0.78$. A similar dependence on the atomic orbital admixture also applies to the orbital or dipolar contributions to the relaxation rate[42, 43]. The conduction electron mechanism is generally taken to be the dominant source of nuclear spin relaxation with the orbital contribution playing a less important role (except for metals with a half-filled band where it can be significant); the dipolar contribution is most generally the least effective[43].

Thus, for the case of T_1^{-1} dominated by d electrons the Korringa relation is more specifically written as,

$$(T_1 T)_d^{-1} = \frac{4\pi k_B}{\hbar} \left(\frac{\gamma_n}{\gamma_e} \right)^2 K_{\text{cp}}^2 F_d K(\alpha_0). \quad (1.28)$$

Here the inverse of the enhancement \mathcal{K}^{-1} has been replaced by the term $K(\alpha_0)$. In this way the Korringa factor is used to quantify the degree of electron-electron interactions in a metal. This was originally considered by Moriya[39] for metals where d electron interactions give rise to large susceptibility enhancements (citing Pd as a specific example), but can equally be applied to simple metals since even these metals show deviations from ideality ($\mathcal{K} = 1$)[44, 45]. The quantity α_0 thus reflects the degree of susceptibility enhancement (it can be taken to be equivalent to the Stoner parameter I_0 , discussed in Sec. 1.3 below) and varies from 0 to 1[39, 44, 45]. According to the present definition of \mathcal{K} , $\alpha_0 \rightarrow 1$ as the enhancement increases. This theory is strictly valid for the ground state, i.e., for $T \simeq 0$. However, care must be taken when applying this approach to real systems, since it was later shown that crystallographic disorder or non-magnetic impurities can alter \mathcal{K} (typically be increasing T_1^{-1}), thus making definitive conclusions about the degree of enhancement difficult[46, 47]. Additionally, all other mechanisms of relaxation (e.g., orbital) must also be taken into account before drawing

any conclusions about electron interactions from the Korringa ratio[48].

1.3 Enhanced paramagnetism and the spin fluctuation model

Referring to Fig. 1.1, it is seen that Pd has a very large and temperature-dependent magnetic susceptibility in contrast to the other metals. Note the temperature-independent and overall diamagnetic susceptibility of Au, typical of the noble metals. Pd has the largest χ of any transition metal that does *not* order magnetically in the pure, bulk state. The peculiar maximum or “knee” at $T \approx 85$ K prompted the authors of one of the earliest measurements of its susceptibility to state that their results “proved to be much more interesting than was expected”[49]. As seen in Fig. 1.1(a), Sc also exhibits such a maximum for $T \approx 30$ K. The susceptibilities of these two metals and that of Pt are characteristic of what is known as *exchange-enhanced* paramagnetism. Fig. 1.1(b) shows that Pd, followed by Sc, are the most exchange-enhanced of the nonmagnetic *d*-metals[50] (α -Mn orders antiferromagnetically at low T); however, there are also many metallic alloys and compounds that fall into this class of magnetic materials (examples are given below). Sc possess a hexagonal close-packed (hcp) crystal structure giving rise to anisotropy of its susceptibility, i.e., $\chi_c \neq \chi_a$ [16, 17], which in this case arises from the orbital motion of the electrons caused by the s-o coupling[51] (the data in Fig. 1.1 is for a polycrystalline sample).⁵ The crystal structures of alloys/compounds are also often complex. By comparison, Pd crystallizes in the face-centred cubic (fcc) lattice structure, which greatly simplifies matters.

It is emphasized that neither Pd, nor Sc, in their pure bulk states, show any type of magnetic ordering at any temperature. This is in contrast to the well-known magnetic *3d* metals[1]: Fe, Co, and Ni that order ferromagnetically below their respective Curie temperatures T_C ; Mn and Cr order anti-

⁵Sc is also like V and Nb in regards to the orbital term dominating, thus producing an anisotropic K [23].

1.3. Enhanced paramagnetism and the spin fluctuation model

ferromagnetically below their respective Néel temperatures T_N .⁶ Nonetheless, on account of their high susceptibilities, an intriguing characteristic of many enhanced paramagnetic materials is the ease with which they may be promoted to order magnetically via some external parameter, such as the application of an external magnetic field, doping with small amounts of magnetic impurities, or a change in lattice constant. This imparts a degree of potentially useful “tunability” to their magnetic behaviour. For the particular case of Pd, the ease of inducing *ferromagnetic* ordering has been well documented over many decades. Thus, the ground state of pure Pd can be considered proximal to a ferromagnetic instability, i.e., it is often described as a *nearly* ferromagnetic metal. Similarly, this statement holds for Sc and to a lesser extent for Pt. Strong paramagnets such as these require treatment analogous to systems that show magnetic ordering; a summary of this theory is now given.

Historically, the development of the theory of metallic magnetism focussed on the *3d* ferromagnets with the emphasis on calculating their T_C values from first principles[1]. In contrast to isolated moments in insulators (where the Heisenberg model[2, 4] works well), a model based on well-defined, localized moments fails for metals. This is because the electrons responsible for the magnetism are the itinerant, conduction electrons that arise from the strong hybridization between neighbouring atoms in a metal, i.e., the band structure[1]. One of the earliest attempts to incorporate features of the band structure was a theory proposed by Stoner[53]. As discussed below, this theory is not correct at finite T , but has merits for understanding the $T = 0$ magnetic properties of metals and introduced a highly useful concept for discussing exchange enhancement.

To start, the susceptibility at $T = 0$ is considered. Eq. (1.10) shows that χ_P is directly proportional to \mathcal{D}_F . By performing a detailed band-structure calculation, one can evaluate \mathcal{D}_F and thus obtain a value of χ_P .

⁶The heavier lanthanides, Gd–Tm, also undergo transitions to magnetically ordered states. A coupling between the highly localized, unpaired *4f* electrons mediated by the *spd* conduction electrons is responsible for the magnetism of these elements[52], and is equivalent to the mechanism of magnetic ordering in many dilute alloys.

1.3. Enhanced paramagnetism and the spin fluctuation model

For metals like Pd, such a computation will yield a susceptibility that is too small in comparison with that measured experimentally for $T \rightarrow 0$. The simplest phenomenological approach is to assume the presence of a molecular exchange field, denoted by the positive constant I_0 [1, 54]. This is a hypothesized internal interaction that acts like an effective magnetic field that tends to align the spins parallel to each other[3]; in other words, it increases the spin polarization. So, in the presence of an applied field H_0 , the magnetization will follow

$$M = \chi_0(H_0 + I_0M), \quad (1.29)$$

where χ_0 is the susceptibility in the absence of the exchange, i.e., the *non-interacting* susceptibility[54]. The exchange field can thus be seen as a source of positive feedback, that for large enough $I_0\chi_0$, can induce a spontaneous magnetic polarization even in the absence of an applied field[54]. Ultimately, the exchange interaction has its origin in the repulsion due to the Coulomb interaction (spin-independent) together with the Pauli exclusion principle (spin-dependent)[2, 4, 54].

At this simplest level of an *intraatomic* exchange interaction, the susceptibility can be calculated by what is known as the random-phase approximation (RPA)[2, 55], leading to the expression for the enhanced susceptibility[56],

$$\chi(\mathbf{q}, \omega) = \frac{\chi_0(\mathbf{q}, \omega)}{1 - \bar{I}\chi_0(\mathbf{q}, \omega)}. \quad (1.30)$$

The term \bar{I} in the denominator above is known as the Stoner parameter; it is given by the product $I_0\mathcal{D}_F$, and defines the *Stoner enhancement factor*,

$$\mathcal{S} = (1 - \bar{I})^{-1}, \quad (1.31)$$

Thus, in the “static” limit ($\mathbf{q} \rightarrow 0, \omega \rightarrow 0$), the interacting susceptibility is that of the Pauli susceptibility [Eq. (1.10)] enhanced by the factor \mathcal{S} , i.e., $\chi_P = \mathcal{S}\chi_0$ [1, 4, 56].

Additionally, Eq. (1.31) further provides a quite general condition for

1.3. Enhanced paramagnetism and the spin fluctuation model

characterizing the proximity to a magnetic instability; namely, as $\bar{I} \rightarrow 1$, $\mathcal{S} \rightarrow \infty$, or alternatively, $\chi \rightarrow \infty$ signaling the onset of ordering. $\bar{I} \geq 1$ is thus known as the Stoner criterion[1, 4]. In this regard, Stoner’s criterion is the simplest condition for a magnetic instability. It is only concerned with the value of the DOS directly *at* E_F , thus neglecting the structure of the rest of the DOS; and it is for $T = 0$, so any possible effect of finite temperature on the DOS is also neglected[57].

For Pd, the susceptibility enhancement over that from band structure calculations[58, 59] usually leads to $\mathcal{S} \sim 9$ ($\bar{I} \simeq 0.9$).⁷ The Pauli susceptibility directly depends on \mathcal{D}_F , and so provides a strong test for such calculations[60]. This is very true for Pd as E_F lies in a region at the top of the d band where the density of states (DOS) is a rapidly decreasing function of energy. E_F lies *just* above a sharp peak in the DOS (~ 25 meV)[58, 59, 60, 61, 62]. \mathcal{D}_F is accordingly high and very sensitive to the position of E_F [63]. Considering the transition metals, the parameter \bar{I} for Pd is only exceeded by those of the $3d$ ferromagnets and Sc[1, 63]. Indeed, the fcc band structure is shared by the ferromagnet Ni; however, the key difference is that in the paramagnetic state E_F of Ni lies even closer to the sharp peak at the top of the band[1].

From theory, the enhancement of the static susceptibility of Pd is strongest around $\mathbf{q} \sim 0$ and $\omega \sim 0$, and decreases quickly with increasing \mathbf{q} (with a Lorentzian form) or ω toward χ_0 [56, 64, 65, 66]. This is the typical behaviour for a ferromagnet. In contrast, antiferromagnetic order is characterized by enhancements at a finite wavevector $\mathbf{Q} \neq 0$ [1]; see e.g., Refs. [51, 65, 66, 67, 68]. I_0 is found to have a weak dependence on \mathbf{q} , and is regarded as a local atomic property[1, 63] (and typically taken temperature-independent). This means the susceptibility is uniformly enhanced[1].

While the “Stoner model” of itinerant electron magnetism[69] in combination with *ab initio* band structure calculations is quite good for the ground state (i.e., $T = 0$); problems are encountered in the application to finite temperatures[70]. Most notably, the model fails to correctly predict the transition temperature[1, 71]. For example, the Stoner model pre-

⁷The more precise values commonly employed for Pd are $\mathcal{S} = 9.4$ or $\bar{I} \simeq 0.89$.

1.3. Enhanced paramagnetism and the spin fluctuation model

dicts T_C values for the $3d$ ferromagnets that are at least four times larger than experiment[70]. This is because the disappearance of the static, ordered magnetic moments must occur from single particle excitations (spin-flips) requiring too high an energy $\sim T_F$ [1]. Additionally, the model fails to adequately describe the Curie-Weiss (CW) behaviour of the susceptibility frequently observed above the transition temperature; while in the ordered state, it also does not properly describe the temperature dependence of the magnetization[71].

Eventually the viewpoint shifted to a focus on collective excitations; Doniach and Engelsberg showed that such collective modes make corrections to the energy calculated in the single-particle Stoner (RPA) model when the exchange enhancement is large[72]. Known as spin fluctuations, they represent long wavelength, low energy, collective excitations of enhanced spin density. The characteristic energy is thus reduced by the low energy of the spin fluctuations as compared to the single-particle excitations (by a factor \mathcal{S})[72, 73], leading to a renormalization of the finite T susceptibility and other thermodynamic properties[72, 73]. In particular, better agreement with experiment is obtained for T_C by treating the transition as fluctuation-driven, and the CW behaviour at high T is also correctly predicted[74, 75]. The spin fluctuations are also known to inhibit Bardeen-Cooper-Schrieffer (BCS) type superconductivity[76], and are invoked to explain the absence of superconductivity in elements such as Pd and Sc in their equilibrium states[77].

With time, an increasing number of structurally ordered alloys were discovered that exhibit very large enhancement factors, e.g., TiBe₂ for which $\mathcal{S} \sim 60$ [67]. Other well-known examples include Ni₃Al (and the related Ni₃Ga), ZrZn₂, Sc₃In, MnSi, and (Sc,Y,Lu)Co₂. Several of these systems order ferromagnetically, but the T_C s are rather low (often of the order of tens of Kelvin); while those that do not order are clearly strongly enhanced paramagnets, i.e., nearly ferromagnetic. All are metallic, and the itinerant electrons are responsible for the magnetic properties. In the paramagnetic state, χ often exhibits an initial quadratic temperature dependence at low temperature; while at higher temperatures, the susceptibilities are univer-

1.3. Enhanced paramagnetism and the spin fluctuation model

sally seen to transition to a CW behaviour that is observable over a wide T range[71, 78]. Moreover, for those systems that do order, the effective magnetic moment μ_{eff} obtained from the Curie constant is always larger than the saturated moment μ_{sat} obtained below T_C [71, 78]. The term “weak” (or unsaturated) ferromagnet is used to describe these materials. The Heisenberg local moment description is invalidated by the ratio $\mu_{\text{eff}}/\mu_{\text{sat}} \gg 1$; while again, the high characteristic energy scale of the Stoner model makes it inappropriate[71, 78]. From the 1970s onward, the importance of spin density fluctuations was becoming clear, and increasing efforts were made to self-consistently incorporate spin fluctuation (SF) corrections to the RPA ground state for itinerant electron magnets. Such a theoretical framework was notably advanced by Moriya and co-workers[71], and Lonzarich and co-workers[54, 78]. The basic notions of the model are sketched below[79, 80] (essentially following the formulation of Ref. [54]).

Spin fluctuation effects can be incorporated into the equation for magnetization by means of the Ginzburg-Landau framework of phase transitions[81]. In this approach the free energy \mathcal{F} is expanded as a power series of an order parameter (that may fluctuate about a mean value). This formalism is strictly valid near the phase transition. For the case of a transition to a magnetically ordered state, \mathcal{F} is expanded in terms of the magnetization \mathbf{M} ,

$$\mathcal{F}(\mathbf{M}) = \mathcal{F}_0 + \frac{a}{2}\mathbf{M}^2 + \frac{b}{4}\mathbf{M}^4 + \frac{g}{6}\mathbf{M}^6 + \dots \quad (1.32)$$

The term \mathcal{F}_0 represents the free energy of the non-interacting system. The magnetic equation of state in the limit of $T \rightarrow 0$ takes the form,

$$\mathbf{H} = \frac{\partial \mathcal{F}(\mathbf{M})}{\partial \mathbf{M}} = a\mathbf{M} + b\mathbf{M}^3 + g\mathbf{M}^5 - c\nabla^2\mathbf{M}. \quad (1.33)$$

The expansion (Landau) coefficients a , b , c , and g are taken to be independent of \mathbf{M} in the case of weak ferromagnets/enhanced paramagnets. The coefficient a represents the inverse of the enhanced susceptibility from the Stoner (RPA) model, i.e., in the absence of the fluctuations: $a = (\chi_0^{-1} - I_0)$.⁸

⁸This means that a is technically T -dependent through the (Stoner) single-particle

1.3. Enhanced paramagnetism and the spin fluctuation model

In the paramagnetic state, a is positive; while it changes to negative in the ferromagnetic state. The coefficient b may be of either sign. In the case that it is positive, the higher-order term (with coefficient g) is often neglected as this term is small for weak magnets; however, in the case of negative b this term must be retained. The term involving the coefficient c represents the spatial gradient of the magnetization. It is added to take into account spatial variations of the fluctuations, and is thus related to the \mathbf{q} dependence of the susceptibility. In essence, the fluctuations are assumed to vary in real space on a scale longer than the electron interactions; this lowest-order gradient term is introduced to account for the non-locality. The sign of c is positive in the case of ferromagnetism, and negative in the case of antiferromagnetism.

The temperature dependence of the magnetic equation of state is taken to arise from the thermally-induced spin fluctuations. They can be viewed as introducing a random magnetization of zero mean to each term on the right-hand side of Eq. (1.33). The terms non-linear in \mathbf{M} generate corrections due to the added magnetization. The effect of the SFs is thus to impart a temperature dependence to the susceptibility, i.e., a renormalization of the $T = 0$ coefficients[74]:

$$a \rightarrow \tilde{a}(T) = (\chi_0^{-1} - I_0) + \frac{5}{3}b\langle \mathbf{m}^2 \rangle + \frac{35}{9}g\langle \mathbf{m}^2 \rangle^2, \quad (1.34)$$

and

$$b \rightarrow \tilde{b}(T) = b + \frac{14}{3}g\langle \mathbf{m}^2 \rangle. \quad (1.35)$$

The quantity $\langle \mathbf{m}^2 \rangle \equiv \xi^2$ represents the sum contribution from the thermal variance of the Fourier components of the spin density fluctuation, $\xi^2 = \sum_{\mathbf{q}} \langle \mathbf{m}^2(\mathbf{q}) \rangle$; $\langle \mathbf{m}^2(\mathbf{q}) \rangle$ is calculated from

$$\langle \mathbf{m}^2(\mathbf{q}) \rangle = \frac{2}{\pi} \int_0^\infty N_\omega \chi''(\mathbf{q}, \omega) d\omega, \quad (1.36)$$

where N_ω is the Bose function. The coefficient b is identified as the mode-mode coupling parameter which describes the coupling amongst the spin excitations; due to the high energy involved, this dependence is typically ignored.

1.3. Enhanced paramagnetism and the spin fluctuation model

fluctuation modes.

The above equation indicates that the generalized dynamic susceptibility $\chi''(\mathbf{q}, \omega)$ is a required input. The following model has been proposed for itinerant d electrons[71, 82]

$$\chi^{-1}(\mathbf{q}, \omega) = \chi^{-1}(\mathbf{q}, 0)[1 - i\omega/\Gamma(\mathbf{q})]; \quad (1.37)$$

where $\chi^{-1}(\mathbf{q}, 0) = \chi^{-1}(\mathbf{0}) + cq^2$ is the static, *non-interacting* susceptibility expanded to lowest order in \mathbf{q} , and $\Gamma(\mathbf{q}) = \gamma_m q \chi^{-1}(\mathbf{q}, 0)$ defines the \mathbf{q} -dependent relaxation rate of the fluctuations. This model is obtained under the assumptions that the fluctuations are small in amplitude, \mathbf{q} and ω are small, and the lattice is cubic (i.e., isotropic). In practice, only the susceptibility is taken to be renormalized by the inclusion of SFs, not the parameters c or γ_m . In this model the fluctuations decay (exponentially) with a rate $\Gamma(\mathbf{q}) \propto |\mathbf{q}|$, a process technically referred to as “Landau damping.” This form of the relaxation reflects the expectation that fluctuations at the critical wavevector will slow down, or “freeze,” as the transition to the ordered state is approached. Inelastic neutron scattering (INS) provides a direct means of studying magnetic excitations, like SFs, since the scattering intensity is related to $\chi''(\mathbf{q}, \omega)$, and it offers the possibility to resolve any \mathbf{q} dependence of the fluctuation spectrum. INS experiments suggest that the above model employing a single relaxation rate is adequate for describing d metals or their alloys[83, 84, 85, 86].

The resulting imaginary component of $\chi(\mathbf{q}, \omega)$ takes the form

$$\chi''(\mathbf{q}, \omega)/\omega \approx \chi(\mathbf{q}, 0) \frac{\Gamma(\mathbf{q})}{\omega^2 + \Gamma(\mathbf{q})^2}, \quad (1.38)$$

which is that of a Lorentzian. Overall, the susceptibility is thus given as

$$\chi^{-1}(\mathbf{q}, \omega; T) = \tilde{a}(T) + cq^2 - \frac{i\omega}{\Gamma(\mathbf{q})}. \quad (1.39)$$

Essentially, as $\langle \mathbf{m}^2(\mathbf{q}) \rangle$ depends on the renormalized $\chi''(\mathbf{q}, \omega)$, the equa-

1.3. Enhanced paramagnetism and the spin fluctuation model

tions can be solved self-consistently.⁹ Thus, the model yields an equation for the temperature dependence of the susceptibility in terms of the $T = 0$ parameters, a , b , g , c , and γ_m . These can, in principle, be obtained from experiment. The parameters a , b (and g) can be obtained from the $T = 0$ limit of magnetization measurements (i.e., as a function of external field), while c and γ_m can be determined from inelastic neutron scattering measurements, or in some cases by NMR as well (see below).

As emphasized by Moriya[71], the CW form of the high- T susceptibility observed over a broad range of temperatures in enhanced paramagnets (or equivalently, weak magnets above the transition temperature) originates from thermal disorder. From $T = 0$, the mean-square amplitude of the spin fluctuations ξ^2 increases essentially linearly with T [74, 75], but is bounded by a saturation value determined by the band structure. The temperature at which the amplitude is considered saturated is denoted by T_{sf} ; above this point, the spin fluctuations are treated as analogous to local moments. So, according to the SF model, the paramagnetic state contains some degree of short-range order, albeit fluctuating, in sharp contrast to the Stoner model, where the state above T_C is nonmagnetic.

The SF model has largely been accepted as the present theoretical basis for treating weak itinerant magnetism. The model can satisfactorily account for many observed properties in materials close to magnetic instabilities[54, 71, 78, 87], such as the transition temperature, the temperature dependence of the magnetization or susceptibility, the ratio $\mu_{\text{eff}}/\mu_{\text{sat}}$, the electronic contribution to the specific heat, and the influence of the magnetism on the resistivity. The model allows for quantitative predictions to be made once the Landau coefficients are known or approximated. The SF model can equally be applied to the finite- T behaviour of the “strong” $3d$ ferromagnets as well[75], where notably the overly large values of T_C from the Stoner theory are considerably reduced to be in broadly better agreement with experiment[1, 88]. The importance of SF effects has also been stressed in the phenomenon of metamagnetism (external field-induced

⁹The model is commonly referred to as the self-consistent renormalization (SCR) theory of spin fluctuations.

1.3. Enhanced paramagnetism and the spin fluctuation model

magnetism)[89]. Although detrimental to the BCS-type, SFs have been considered as possible mediators for a more “exotic” type of superconductivity; one which thus co-exists with magnetism[54, 90, 91].

Long known to be an enhanced paramagnet, palladium was one of the prototype systems in the earliest studies of spin density fluctuations[64, 72, 76]; their important role in its magnetic properties is quite well-accepted[66, 80, 92, 93]. Earlier methods of experimentally “seeing” their presence in palladium was through their additional contribution to electron scattering in low temperature transport measurements[94]. Takigawa and Yasuoka[32] show that χ_{Pd} obeys the CW law from about 250 K up to at least ~ 1700 K (the melting point of Pd is 1828 K). In addition, they observed a T -linear $^{105}\text{Pd } T_{1d}^{-1}$ at low temperatures that tended toward saturation above about 275 K. The rate above T_{sf} was not consistent with a fixed-spin, local moment relaxation as estimated from the high- T CW analysis of χ [cf. Eq. (1.2)]; instead it was considered to be consistent with the prediction from the SF model of a monotonic increase of ξ^2 with T , followed by saturation above T_{sf} giving rise to thermally-induced, local moment-like behaviour[71]. Their estimate of $T_{\text{sf}} \sim 250$ K[32] is in keeping with the value generally taken for Pd[95]. By comparison, this is an order of magnitude larger than that of many weak ferromagnets[95]. A recent *ab initio* calculation of χ_{Pd} [93] explicitly shows the linear increase of ξ^2 with temperature; tending toward saturation above about 200 K.

As mentioned above, INS can most directly probe SFs. Doniach pointed out many years ago that SFs should be observed in Pd by this technique[56], but it wasn’t until very recently that this was actually achieved[84]. The excitation energies of the spin fluctuation spectrum in Pd are quite low and were found to extend over a broad range spanning an order of magnitude. The authors applied the model of $\chi''(\mathbf{q}, \omega)$ given by Eq. (1.37) and found it to provide a “reasonable global description” to the SF spectrum[84].

At this point, the maximum in χ_{Pd} is considered in a little more detail. Indeed, such maxima are (almost) ubiquitous in enhanced paramagnets and there have been various explanations put forth as to their origin. The question is still not firmly resolved, and it is quite likely that there is not one

universal origin.

One line of thought attributes the maxima to T -dependent corrections to the susceptibility due to scattering of electrons on the Fermi surface in the presence of strong electron interactions[96, 97, 98, 99, 100, 101]. However, throughout the years, there were often disagreements as to the exact form and degree of importance of these corrections.

Within the SF model, a maximum in the susceptibility can arise if the mode coupling parameter b is negative[71, 78]. Additionally, Yamada has highlighted the role of negative mode-mode coupling in metamagnetism[89], and in potential magnetovolume anomalies[102]. In such a case, Eq. (1.32) must be carried out to include the \mathbf{M}^6 term[54]. This was recently illustrated by the susceptibilities of Ni_3Al and Ni_3Ga . The former is a weak ferromagnet, while the latter does not order and is instead a strongly enhanced paramagnet. Smith found that the magnetization and susceptibility of Ni_3Al can be described using an expansion involving just the two Landau parameters a and positive b ($g \equiv 0$); while the susceptibility of Ni_3Ga was best described with b negative, thus requiring all three parameters[79]. The extended form of the expansion is a means of incorporating any low temperature corrections; viewed as altering the effective interaction between the fluctuation modes[103].

Within the SF model, the expansion coefficients can be derived microscopically from the form of the band structure[71, 78]. This opens the possibility of calculating these parameters *ab initio*[67, 80, 104, 105]. The band structure itself is material-specific, and so features in the electronic dispersion may play a role. For instance, if there are peaks, or singularities, in the DOS close to E_F , these can result in divergent quantities making application of the model problematic[67]. The non-interacting DOS controls the \mathbf{q} dependence of the generalized susceptibility, and so directly influences the SF spectrum[104].

According to the Stoner theory, $\chi(T)$ of an enhanced paramagnet follows a T^2 variation with a coefficient that is determined by the difference between the second and first derivatives of \mathcal{D}_F with respect to E [58, 59, 69]. A DOS that gives rise to a positive second derivative can lead to $\chi(T)$ initially in-

1.3. Enhanced paramagnetism and the spin fluctuation model

creasing with T , thus exhibiting a maximum[69]. This criterion is indeed found from the DOS of Pd[58, 59, 69], while \mathcal{D}_F itself decreases by approximately 6% between 0 K and room temperature (due to thermal vibrations of the atoms, i.e., phonons)[61]. Within the SF model, the mode coupling parameter b is also determined by this same difference in the derivatives of \mathcal{D}_F [71, 78, 106], where a positive second derivative is generally indicative of a negative b . Thus, within this model, the maximum in χ_{Pd} may require the use of the extended expansion, as mentioned above. However, E_F of Pd lies just above a peak in the DOS. A strongly peaked DOS near the band edge (dictated by the lattice structure) has been identified as being an important condition for stabilizing ferromagnetism in general[57, 107]. In particular, E_F appears in a region of the DOS that is rapidly varying and near to an inflection point[80, 109]. In calculations, this results in extreme sensitivity of results to the placement of E_F [58, 59, 60, 108, 109]. The second derivative of \mathcal{D}_F is correspondingly a difficult quantity to calculate precisely[59, 80].

At the maximum, χ_{Pd} is $\sim 10\%$ larger than at $T \simeq 0$. It is conceivable that such a small increase requires only a weak temperature dependence, as, e.g., that found for \mathcal{D}_F [61]. For instance, in TiBe₂, E_F lies just below a sharp peak in the DOS and it was concluded that the enhanced $\chi(T)$ (which varies more strongly with T than that of Pd) could be adequately described by a T -dependent E_F accompanied by thermal “smearing” of the DOS[67]. The possibility has been suggested that $\chi_{\text{Pd}}(T)$ can be completely described within the Stoner (single particle) model for enhanced paramagnets if a very accurate band structure is employed[109]. One method of improving the agreement of the Stoner susceptibility with experiment is to allow for the effective, mean-field exchange parameter I_0 to be temperature-dependent. In the past, such an approach has indeed been considered for the susceptibility of enhanced paramagnets like Ni₃Ga[110] and Pd[108, 111]. Most recently, Zellermann *et al.*[109] employed this approach and succeeded in reproducing $\chi_{\text{Pd}}(T)$ up to 800 K with the maximum appearing about 20 K lower than experiment. In this case, it is found that the interaction parameter needs only a thermal variation $\sim 1\%$ up to room T [109, 111], indicative of the general adequacy of the Stoner model[109]. A weakly T -dependent

1.3. Enhanced paramagnetism and the spin fluctuation model

I_0 may be viewed as an alternative way of dealing with small uncertainties in the DOS and thus \mathcal{D}_F and its derivatives. In Ref. [109], the small variation of this quantity was interpreted as due to a renormalizing effect of the collective thermal excitations; highlighting the close relation between the single particle and collective effects, as the latter is strongly dependent on the former.

In light of this, it is interesting to mention the renormalizing effects that are attributed to the zero-point (zp) fluctuations in the spin fluctuation models. In the earlier treatments[71, 78], they were assumed to produce a T -independent renormalization of the interaction constant, $I_0 \rightarrow \tilde{I}_0$; which may be equivalently viewed as a renormalization of the DOS[78]. Subsequently, recent elaborations on the SF model have considered the role of the zp fluctuations in more detail and have emphasized their influence on the mode coupling parameter in particular[87, 112, 113, 115, 116, 117]. Miyai and Ohkawa have argued that the CW susceptibility observed in itinerant ferromagnets (especially those with on-site interactions strong enough that the moments can be considered as “almost localized”) stems not only from thermal spin fluctuations, but also from a temperature-dependent mean-field interaction which occurs when there is a sharp peak in the DOS in the vicinity of E_F [118].

To close, the use of NMR to probe the spin fluctuation spectrum of a metal is briefly summarized. In Sec. 1.2.2 above, T_1^{-1} was shown to depend on the transverse fluctuations of the imaginary part of the dynamical susceptibility [cf. Eq. (1.20)][39],

$$\frac{1}{T_1 T} = \frac{\gamma_n^2 k_B}{\mu_B^2 \hbar} \sum_{\mathbf{q}} |A_{\text{hf}}(\mathbf{q})|^2 \frac{\chi''(\mathbf{q}, \omega_L)}{\omega_L}. \quad (1.40)$$

For definiteness $A_{\text{hf}}(\mathbf{q})$ is taken to be independent of \mathbf{q} . As the NMR frequency is small, one can take the limit $\omega_L \rightarrow 0$. Similarly, for the case of \mathbf{q} , one considers small values around the critical wavevector, as required by the SF theories ($\mathbf{q} \sim 0$ for a ferromagnetic instability). Using the form described by Eq. (1.38) leads to $\chi''(\mathbf{q}, \omega_L)/\omega_L \propto \chi(T)/\Gamma_0$; where $\chi(T)$ is

1.3. Enhanced paramagnetism and the spin fluctuation model

the static uniform susceptibility [i.e., $\chi(\mathbf{0}, 0)$], and Γ_0 represents the energy scale of the SF spectrum.

As $(T_1 T)^{-1}$ is typically dominated by the d electron (SF) contribution, if the corresponding $K - \chi$ plot is found to be linear (at least over some T range), then $K_d(T) \propto \chi_d(T)$ and

$$(T_1 T)_d^{-1} \simeq \kappa K_d(T) + y; \quad (1.41)$$

where y is a constant off-set that accounts for the contributions from all other less important relaxation processes. Ignoring the constants gives $\kappa \propto (\gamma_n^2 A_{\text{hf}}^d)/\Gamma_0$ (recalling the A_{hf}^d can be determined from the slope of the $K - \chi$ plot). This implies that a plot of $1/(T_1 T)_d$ vs. K_d with T as the implicit variable directly yields a slope that is inversely proportional to the energy width of the SF spectrum. This linearity is a consequence of the dynamic properties of metals close to, or possessing, a magnetically-ordered state (an analogous scaling exists for antiferromagnets)[71, 119]. This behaviour is clearly distinct from the Korringa relation [Eq. (1.26)], which is applicable to simple metals that are far from a magnetic instability. The dynamical scaling predicts a diverging zero-field T_1^{-1} as the critical T is approached, reflecting the divergence in $\chi(T)$ as the ordered state is approached[119].

The earliest report of $1/(T_1 T)_d$ scaling with χ_d was from Ti NMR of TiBe₂[120], and has later been observed in a variety of metallic systems with ferromagnetic[121, 122, 123, 124, 125, 126] and antiferromagnetic[85, 127] SFs; the former including Pd[32]. The quantity Γ_0 is equivalent to the product $c\gamma_m$, and is expressed as a temperature denoted T_0 [71, 113]. The use of NMR in this regard has encountered a very well-known issue associated with the implementation of the SF theory itself; namely, the need to define a cut-off wavevector q_c . This quantity enters directly in converting Γ_0 to T_0 , or vice-versa. For instance, Corti *et al.* obtained a value of T_0 from Si NMR of MnSi that was a factor of four smaller than the value obtained from INS[123]. The authors could obtain agreement if the value of q_c used in converting Γ_0 was made four times larger than prescribed by the standard SF model[123]. A similar conclusion about the need for a larger q_c was

also recently reported from NMR measurements in a different system[125]. Since the SF models are based on small \mathbf{q} expansions, the need to use a large q_c signifies a problem with the SF model in its original form. This is a notable difficulty in applying the SF models as there is no exact definition of q_c [80, 86, 105], and the results are sensitive to the \mathbf{q} range employed[71, 109].

1.3.1 Further notes on the susceptibility of Pd

It is noted that χ_{Pd} does not show any dependence on applied field[128, 129, 130, 131], and that this is valid for fields as high as 40 T[95]. A tiny non-linearity, i.e., increase, at high fields and low temperatures was reported with a correction factor $\sim 10^{-14}/\text{G}^2$ [128]. This amounts to less than 1% correction, and can safely be neglected[129, 130]. This is consistent with the absence of a metamagnetic transition for Pd, in accord with calculations[92, 132, 133]. In Ref. [132] the critical field for this transition was predicted to be ~ 300 T.

The electronic structure, and therefore the magnetism of Pd is very sensitive to the underlying lattice structure[134]. Since E_F lies in a strongly varying part of the DOS, even tiny changes in the lattice parameter can have a large effect on \mathcal{D}_F [62]. One notable consequence of this is the prediction that pure Pd will be ferromagnetic for a lattice expansion $\sim 5\%$ [135, 136, 137, 138]. An expanded lattice results in a narrowing of the d band and thus increased \mathcal{D}_F that, together with the high value of I_0 , will satisfy the Stoner criterion for ferromagnetism. One experimental result attributed to this effect was reported for thin Pd layers epitaxially strained in the form of Au/Pd/Au sandwiches. Although the strained Pd did not exhibit ferromagnetism, the low temperature susceptibility was significantly enhanced: $\mathcal{S} \sim 10^2 - 10^4$ [139]. It was concluded that the anisotropic nature of the strain due to the two-dimensional nature of the samples plays an important role in this enhancement[140, 141, 142, 143]. In this regard, it has been suggested that a strained lattice will also significantly reduce the critical field necessary for a metamagnetic transition[132]. Indeed, according to Hjelm[133], lattice expansions of 2–5% cause the magnetization to increase

strongly as the applied field is increased from 0 to 50 T; for an expansion of 5%, he predicts the critical field to be only 10 T. The potential influence of lattice deformation on the susceptibility is important to keep in mind when studying thin films of Pd, e.g., the β -NMR measurements presented in Chapter 5.

Briefly, it is well-documented that the susceptibility of Pd is also sensitive to the presence of impurities; in particular, all *non*-magnetic impurities are known to cause $\chi(T)$ to *decrease*. Overall, as the impurity concentration is increased, the magnitude of χ is reduced and the maximum becomes less pronounced; eventually for sufficient impurity concentration, the maximum is completely eliminated and the susceptibility becomes temperature-independent[11, 144, 145, 146, 147, 148, 149]. In general, the susceptibility is reduced by a few per cent for every at.% of impurity. For example, in the case of dilute Ag impurities, the initial reduction in the susceptibility is by about 3% per at.% Ag, and the maximum in χ is essentially eliminated for ~ 5 at.%[11, 148]. This reduction in the susceptibility applies to impurities in the form of substitutional alloys, as well as interstitial impurities. The latter is best illustrated by the susceptibilities of the hydrides[15, 150], as Pd readily absorbs H (or deuterium) into the octahedral interstices. The susceptibility is reduced by approximately 1.5% for each % of H(D) absorbed, essentially independent of temperature[150]. As the concentration is increased above 60%, the maximum in χ is eliminated, resulting in a T -independent susceptibility that eventually becomes diamagnetic[15]. A similar reduction in χ has also been observed when B is introduced into the octahedral sites[151]. A notable exception is dilute Rh impurities. In the concentration range between 1 and 10 at.%, these substitutional alloys show enhanced susceptibilities compared to that of the pure host, with a χ that increases continually upon cooling below room temperature[13, 148]. Alloys with Rh concentrations between 3 and 8 at.% exhibit a susceptibility at 4 K that is almost twice as large as that of Pd[148]. However, as the Rh concentration is increased above 10 at.%, the susceptibilities of the alloys again become reduced in comparison to Pd[13].

In contrast, since the susceptibility of Pd is so strongly enhanced, it has

long been known that magnetic impurities like Fe and Ni readily generate a ferromagnetic polarization of the conduction electrons, even in very dilute concentrations[152]. A *single* magnetic impurity is sufficient to generate a region of ferromagnetic polarization that encompasses a significant number of surrounding host atoms. The localized moment together with the moment induced on the atoms within the polarized region (or “cloud”) give rise to what is termed a “giant moment”[152, 153]. Fe impurities give rise to the largest giant moments in Pd, with reported values of the effective moment in the range of 7–15 μ_B , depending on the concentration[153]. Neutron diffraction measurements estimate the spatial extent of an Fe-induced giant moment to be of the order of a nanometer in Pd[154]. A similar effect occurs when magnetic impurities are introduced into Pt, but the size of the giant moments are about half as large[153]. Thus, for sufficient concentrations of magnetic impurities, the giant moments can percolate throughout the volume of the host giving rise to a highly dilute alloy that can order ferromagnetically. For Fe in Pd this occurs for concentrations ~ 0.1 at. %[152, 155]. At this low concentration, T_C is only around 5 K, but it increases sub-linearly with increasing Fe, and appears to saturate at about 400 K in the more concentrated alloys (~ 20 at. %)[155]. In the case of Ni, a higher concentration ~ 2 at. % is required to drive Pd ferromagnetic; however, in this case it is not isolated Ni atoms, but rather small Ni clusters that are responsible for the induced ferromagnetism[156].

1.4 An alternative: implanted probes

While NMR is an attractive method to study the electronic structure of materials (as it is in the study of molecules and liquids), it is not without limitations. Specifically, signal-to-noise, i.e., low sensitivity imposes restrictions. In conventional NMR the signal is detected through changes in the population of nuclear spin levels; the initial polarization produced by an external magnetic field and follows a thermal (Boltzmann) distribution. The signal is frequently detected via the voltage induced in a pick-up coil (that scales with ω_L). As the degree of nuclear polarization is low, detection us-

ing a macroscopic circuit requires there be a large number of spins; typically $\sim 10^{18}$. Besides the requirement of a sufficient amount of sample, in the case of metals (i.e., conductors) there is a second consideration. The radio-frequency (rf) magnetic field used to induce the spin population changes can only penetrate into a metal a certain distance which is both material- and frequency-dependent and is called the rf “skin depth” [157]. For metals, this is typically of the order of microns. Consequently, NMR experiments on metallic systems are most generally performed on samples in the form of randomly-oriented powders.

In some cases, using fine-powdered samples can be desirable, since at very small length scales the electronic structure is often distinct from that of the macroscopic scale, and NMR can be used as an effective tool to study such “finite-size effects” (see e.g., Ref. [5]). However, in real devices, materials are often used in the form of thin films or multilayers. In this geometry both a free surface and interfaces exist. Most generally, one can expect that the electronic structure of a material will also be distinct from that of the bulk in the vicinity of a surface or interface [158]. The change may be localized to a single atomic layer, or it may exhibit a “healing length” in which it recovers back to the bulk state over a distance of spanning several layers, perhaps in an oscillatory fashion. While NMR does probe the electronic structure of a material with atomic scale resolution, there is inherently a small number of spins in the surface or interfacial regions, and this severely limits the application of the technique to such samples. In the field of materials, NMR is largely restricted to be a bulk probe of matter. This is troublesome since there is an ever growing interest in materials of reduced dimensions (i.e., size) for applications in electronics and catalysis, etc. Analogous to powders, as a film becomes thinner, the surface or interface becomes an increasing fraction of the total volume and in many cases the electronic modification is intimately connected with this increase. There have been some successful applications of NMR to the study of the interface between two different metals [159], but such studies are certainly quite rare. One method of extending the technique to the study of surfaces is to perform NMR measurements on adsorbates that have been pre-polarized [160].

1.4. An alternative: implanted probes

A powerful alternative to conventional NMR in this regard is the use of radioactive probes[161]. The outstanding advantage to such techniques lies in the method of detection. Broadly, in these spectroscopies the signal is detected through high-energy radiation emitted by a radioactive nucleus as it undergoes decay. This in turn improves the signal-to-noise by orders of magnitude. Consequently, far fewer spins are required making nuclear probe techniques well suited for the study of samples consisting of a small number of atoms. The probe nuclei are either implanted into the sample, or in some cases, incorporated directly during synthesis. Frequently, this allows for the possibility of studying condensed matter in a depth-resolved manner. The implanted probes are sensitive to the *local* electronic structure of the host through the various hyperfine interactions, in a fashion analogous to the hf interactions of the host nuclei in conventional NMR (discussed above in Sec. 1.2).

In the present investigations one such nuclear technique, namely that of beta-detected nuclear magnetic resonance β -NMR, has been applied to the study of metallic paramagnetism. The technical and experimental details are presented in Chapter 2 and Appendices A and B. Briefly, a low-energy beam of ${}^8\text{Li}^+$ ($I = 2$) is optically polarized in-flight and subsequently implanted into a sample. A variable, static, external magnetic field is applied longitudinal to the nuclear spin and a magnetic resonance is detected by the application of a small, transverse, rf magnetic field. The technique relies on the anisotropic distribution of electrons emitted in beta-decay of the probes. When the rf field is on resonance with the nuclear spin splitting, the polarization is destroyed as the spin precesses in the rf field resulting in a loss of the measured beta-electron count rate asymmetry. β -NMR can be performed using $\sim 10^6$ implanted spins; so, the probes are in the highly dilute limit and interactions between them can be safely neglected.

The technique of β -NMR is very similar to the technique of muon spin rotation/relaxation spectroscopy μ SR[161, 162]. Typical μ SR involves the implantation of 2–4 MeV positive muons into a sample. In contrast, the β -NMR spectrometer used for the present studies was specifically designed to permit electrostatic deceleration of the low energy (~ 30 keV) ion beam,

and thus allow for variable implantation depths. This translates into the ability to perform measurements on small length scales; for many materials this ranges between $\sim 10 - 10^2$ nm. Thus, systematic investigations as a function of distance from a free surface, or from a buried interface are readily possible. In this regard, low-energy β -NMR[163] is similar to low-energy μ SR[164]. As the static external field is not used to generate nuclear spin polarization, the technique can in principle be performed for any value of the applied field, including zero field (which in the case of $I > \frac{1}{2}$ allows for low-energy beta-detected nuclear quadrupole resonance β -NQR[165]).

One of the earliest, and still employed, applications of the β -NMR principle is for the determination of the nuclear magnetic[166] or quadrupole moments of an isotope[167]. The total hf field sensed by the implanted probe is made up of contributions analogous to those of the host nuclei in conventional NMR[161]: Fermi contact, as well as orbital, dipolar, and potentially electric field gradients (EFGs). The Fermi contact interaction is expected to be the source of the largest hf field at the nucleus and originates from the coupling of the probe to the host electrons. For the case of a light ion like ${}^8\text{Li}^+$ in a transition metal, the dominant coupling is expected to arise between the Li $2s$ orbital and the d band of the host[168]. In this way a Knight shift and T_1^{-1} due to this coupling can be defined. The former can be evaluated according to Eq. (1.16) using ν_0 measured in a suitable reference material, i.e., a diamagnetic insulator. Measurements of T_1^{-1} can be made without the need for an rf magnetic field by monitoring the loss of probe polarization with time following implantation. The dipolar interaction is discussed below, while the perturbation due to a EFG is discussed in the following Chapter. For a light probe, the orbital interaction arises from the motion of its electrons and is thus analogous to the chemical shift in conventional NMR. Specifically, from ${}^6,7\text{Li}$ NMR, these shifts are small; typically in the range of -10 to +10 ppm[169].

The coupling between the probe and host can be quantified by a hf

1.4. An alternative: implanted probes

coupling constant defined as

$$A_{\text{hf}} = \frac{g_e \mu_B N_A}{z} \frac{K}{\chi_P}. \quad (1.42)$$

In this form, A_{hf} is expressed in units of kG/μ_B . The variable z represents the co-ordination number of the probe's final stopping site in the host lattice, so A_{hf} is a quantity that is expressed per atomic neighbour. This highlights an important difference between conventional NMR and implanted probe techniques like β -NMR, where following implantation, a light ion may come to rest at distinct lattice sites in the host. For instance, it may occupy a regular lattice site arising from host vacancies created during the implantation process, in which case it is considered a substitutional impurity. Alternatively, it may remain in an interstitial site. This is an advantage of using implanted nuclear probes as they offer access to the electronic structure of the interstitial regions— which are more difficult to study by conventional NMR. The strength of the hybridization is, in the simplest picture, a function of z and the distance between the probe and the neighbouring host atoms, in addition to the details of the electronic structure of the probe and host. The NMR observables K , T_1^{-1} , linewidths, and (where applicable) EFGs, will thus depend sensitively on the probe's stopping site. Additionally, A_{hf} is sensitive to factors like the degree of electronic screening in the immediate vicinity of the probe by the electrons of the host, and to the extent of local host lattice relaxation around the probe. Results from measurements of the hf field at implanted probes provide stringent tests for electronic structure calculations[170, 171, 172]. One can perform a Korringa analysis [i.e., Eq. (1.26)] on the Knight shift and T_1^{-1} measured for an implanted probe and compare the degree of electronic enhancement at the probe with that for the matrix nuclei obtained by conventional NMR (when available)[173, 174]. For the case of ${}^8\text{Li}$, $S_0 = 1.20 \times 10^{-5} \text{ s K}$ in Eq. (1.26).

One of the main challenges in interpreting results from a light implanted probe is thus the unambiguous determination of the final stopping site(s). Muons are interstitial probes and heavy ions are generally substitutional, but lighter nuclei like ${}^8\text{Li}$ and ${}^{12}\text{B}$ can possibly occupy both interstitial and

1.4. An alternative: implanted probes

substitutional sites. In this respect, the dipolar interaction can be useful. Specifically, the nuclear dipole-dipole interaction between the probe spin and host spins may be the dominant mechanism giving rise to a broadening of the resonance. The magnitude of the interaction depends on the lattice site, as well as the crystallographic orientation. By using single crystal samples the direction of H_0 can be varied with respect to the crystal axes and the resulting linewidths compared with those predicted from van Vleck's expression for dipolar line broadening due to unlike spins[20, 175],

$$\sigma_{\text{dip}}^2 = \frac{1}{3} \gamma_I^2 \gamma_S^2 \hbar^2 S(S+1) \sum_i \frac{(3 \cos^2 \theta - 1)^2}{r_i^6}, \quad (1.43)$$

where \mathbf{r} is the distance vector from the probe spin I and the host spin S , θ the angle between \mathbf{r} and H_0 , and the sum runs over a given number of neighbouring lattice shells. However, if the host spins possess a quadrupole moment, the above equation does not necessarily hold because the presence of a charged probe generates an EFG on the surrounding host nuclei that influences the orientational dependence of the dipolar widths[176]. Eq. (1.43) is applicable only for sufficiently strong H_0 , i.e., such that the magnetic Zeeman energy is larger than the electric quadrupole energy for the neighbouring host spins[176, 177]. The dipole-dipole interaction provides the basis for an alternative method by which the stopping site can indeed be unambiguously determined. Briefly, when the host spins are quadrupolar, the EFG induced by the probe permits the possibility that, for particular finite values of H_0 , the energy of the $|\Delta m_I| = 1$ transition for the probe and host spins are equal. When this condition is satisfied, the probe and host spins can undergo mutual spin flips resulting in the transfer of polarization from the probe to the host spin system, a process termed cross-relaxation[178, 179]. The resonance-like loss of probe polarization at specific values of H_0 provides a "fingerprint" of the stopping site for a given crystal orientation with respect to the applied field.

In the application of implanted probe NMR to the study of fcc metals resonances are almost always observed without satellites, being indicative

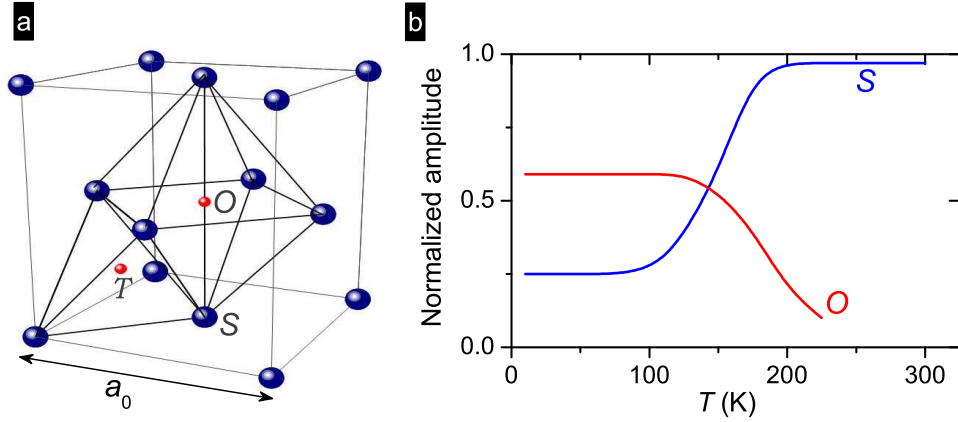


Figure 1.3: (a) Three possible stopping sites of cubic symmetry for an implanted probe in the fcc lattice: the tetrahedral (\mathcal{T}) and octahedral (\mathcal{O}) interstitial sites, and the substitutional sites (\mathcal{S}). (b) Temperature dependence of the resonance amplitudes assigned to $^8\text{Li}^+$ occupying the \mathcal{S} and \mathcal{O} sites in a 50 nm Ag film, as reported in Ref. [184].

of high symmetry (cubic) stopping sites where the EFG vanishes or is very tiny. In the fcc lattice there are three such stopping sites for a light probe: the substitutional \mathcal{S} sites ($z = 12$), the octahedral \mathcal{O} interstices ($z = 6$), and the tetrahedral \mathcal{T} interstices ($z = 4$); see Fig. 1.3(a). The \mathcal{T} sites are smaller than the \mathcal{O} sites, and the energy of the lattice is much higher when a probe occupies the former over the latter[171]. For this reason, the \mathcal{O} sites are generally favoured over the \mathcal{T} sites as potential interstitial locations for light implanted ions.

The following general picture regarding the stopping sites for light ions has emerged. Implantation at low temperatures results in probes predominantly coming to rest in \mathcal{O} sites where they remain immobile. As the temperature is raised, a thermally-induced site change occurs resulting in increasing occupation of the \mathcal{S} sites. After this site migration, the probes are still immobile in the \mathcal{S} sites; this site change does not mark the onset of long-range diffusion. The population of the sites at a given T depends on the specific probe-host combination. The conclusion that the \mathcal{O} site is the low temperature location for ^{12}B and ^{12}N in Cu and Al was made on the basis

of dipolar linewidths[180, 181]. By means of the cross-relaxation method, a definitive assignment of ^{12}B to the O site in Cu and Al was made[182], as well as its thermal migration to the S in Cu[179]. On account of the r^{-6} dependence of σ_{dip} it was concluded that ^{12}B and ^{12}N in the O site of Cu or Al produces a local lattice expansion $\sim 10\%$ [181, 183]. Similarly, when a smaller ion occupies the S site, a local lattice contraction may be expected[179], as was indeed reported for ^{12}B in ZnSe[177]. The local lattice relaxation about an implanted ion is thus a significant factor contributing to the hf interactions sensed by the probe[168, 170, 171, 181, 183].

Results from ^8Li β -NMR of fcc metals Ag[184], Cu[185], Al[186], and Ni[172] have been interpreted in terms of these site occupations as a function of temperature. At low T , resonances at two distinct frequencies are observed. The higher frequency resonance is assigned to ions in the O sites, since as T is increased, this resonance gradually decreases in amplitude concomitant with an increase in the amplitude of the lower frequency line, thus assigned to S ions. In many hosts, for T on the order of room temperature, only resonances from ions in the S site are observed. This is illustrated in Fig. 1.3(b) by the normalized amplitudes of the resonances recorded in a Ag film as a function of T [184]. Correspondingly, this site change behaviour is manifest in the spin-lattice relaxation rates: T_1^{-1} is observed to be linear with T — consistent with the Korringa mechanism described in Sec. 1.2.2 above— with a gradual decrease in slope over the T interval where the ions undergo the $O \rightarrow S$ site change[185, 186, 187]. The occupation of S sites arises from ions that have encountered a host vacancy created during the implantation process, since this resonance can be observed even at low T . It is pointed out that the site change may not be due to migration of the Li itself; instead, S sites may be generated through combination with a thermally-migrating host vacancy created during the ion implantation. Regardless, the supply of host vacancies available to a probe most generally must have been created during the implantation process as the energy required for the formation of an intrinsic self-vacancy in metals is quite high[188].

The goal of the research presented herein is to apply the technique of low-energy β -NMR to study of the magnetism of pure transition metals, thereby

demonstrating the utility of this technique in extending the application of NMR for investigations of this important property. Specifically, to illustrate the applicability of β -NMR to the study of magnetism in systems where conventional NMR is difficult or most generally not possible, like samples in the form of films, or for metals like Pd. To this end, results of ^8Li β -NMR of non-magnetic Au are also presented and serve as a contrast to those of the enhanced paramagnetism of Pd. The samples studied are chosen to be representative of the bulk properties of these metals in order to establish a firm understanding of the behaviour of the $^8\text{Li}^+$ probe in the bulk metallic state. The term bulk is employed here to mean samples sufficiently thick that no finite-size effects are expected (in general, greater than ~ 10 nm). This serves as an important prerequisite to any future β -NMR investigations of samples of reduced geometry.

In the case of Au, the study completes the ^8Li β -NMR of the group 11 (or noble metals) and the results can be compared with those obtained in Ag[184] and Cu[185]. There exists no previous ^8Li β -NMR study of Au as a function of temperature. In Ref. [166] a resonance and T_1^{-1} measurement were made at room T towards the determination of the ^8Li magnetic dipole moment; a separate room T measurement of T_1^{-1} was also later reported for ^8Li in this host[189]. A β -NMR study of Au using ^{12}B was performed for temperatures in the range of 100 – 300 K[173].

The study of these simple, non-magnetic metals in their pure, bulk form is important as they are often used as spacer layers in magnetic multilayer heterostructures. For example, the magnetic coupling between two ferromagnetic layers separated by a non-magnetic metal layer can be tuned by changing the thickness of the latter. Such heterostructures can thus be used for spin-dependent transport applications. The depth resolution capabilities of low-energy β -NMR make it quite well-suited for the study of the magnetic interactions in such multilayers. Indeed, the spatial dependence of the induced magnetism in a Ag layer in contact with a ferromagnetic Fe layer has already been successfully studied by low-energy β -NMR[190].

Owing to its chemical inertness, Au is frequently used as a capping layer for thin film samples. A powerful application of low-energy β -NMR is the

study of magnetism at surfaces by implanting the probes in a thin, non-magnetic metal overlayer and monitoring the magnetic behaviour proximally[191]. This has recently been accomplished for the case of a Ag overlayer on a high-temperature superconductor[192]. The more frequent use of Au protective layers make it potentially more attractive for such studies. A detailed study of the ^8Li resonances in pure Au is thus clearly required for such an application.

A very different situation is to be expected in the case of an enhanced paramagnet like Pd. The electronic structure of this metal is highly sensitive to its lattice structure, and recently ferromagnetism has been reported for samples in the form of thin films[193] and small particles[194]. Conventional NMR of Pd is most generally not feasible in these cases, and so low-energy β -NMR is an ideal alternative. However, this same sensitivity of Pd requires an initial clear understanding of the response of this metal to the implanted ion itself.

Just as in the case of Au, there have previously been only two room temperature β -NMR measurements of ^8Li in Pd, i.e., Refs. [166, 189]. Based on their determination of the ^8Li magnetic moment, the authors of Ref. [166] concluded that K is negative for this probe in Pd, and that \mathcal{K} at 300 K is $\simeq 6$. The remaining implanted probe studies of Pd have been performed with ^{12}B and ^{12}N [195, 196] or μ^+ [197, 198]. In Ref. [196], the ^{12}B and ^{12}N measurements were performed for temperatures in the range of 100 – 600 K and a linear $K - \chi$ scaling was observed for both probes; the shift of ^{12}N was found to be positive for all T , while that for ^{12}B changed from negative to positive at $T \approx 400$ K. Additionally, for both probes the observed shifts were notably enhanced over that predicted from the measured T_1^{-1} and the Korringa relation. In the case of μ^+ , the reported shifts are negative[197, 198]. In Ref. [198] data were collected for T extending up to 900 K, and an overall linear $K - \chi$ scaling was also observed, except for T below the maximum, where the shifts do not appear to track the decrease in χ as closely. The results of the positive muon K for T below room temperature are also included for comparison in Fig. 1.2.

A close similarity between the magnitude of K in Pd and the magnitude

of the hf field in Ni as a function of the impurity valence for Cu, Al, Sn, and μ^+ has been observed experimentally[170, 197]. This similarity illustrates that the hf fields in a strongly enhanced paramagnet are physically similar[170]. Calculations predict the hf field for ^8Li impurities at all three cubic lattice sites in Ni to be negative[171]. Indeed, in the β -NMR of ^8Li in Ni, two resonances were observed both with negative K , being assigned to ions in the O and S sites[172]. Briefly, the negative hf field at a non-transition impurity in a ferromagnetic host can largely be rationalized in terms of a core polarization-like process for the bonding electrons between the probe and host via the $s - d$ hybridization[170].

The above serves as a general summary of important aspects of the β -NMR of metals. The following Chapter is devoted to further details of the technique.

Chapter 2

The β -NMR Technique (at TRIUMF)

2.1 Introduction

In the previous chapter, the advantages of using implanted radioactive ions as probes of matter in over-coming the limitations of convention NMR to study thin films, or surfaces and interfaces was discussed. As β -NMR is a rather “exotic” technique, the present chapter is devoted to a description of this spectroscopy with respect to the TRIUMF facility.

The most basic requirement of β -NMR is the ability to produce an isotopically pure beam of the desired radioactive ion. This need is met at the TRIUMF’s ISAC (Isotope Separator and ACcelerator) facility. Following a brief sketch of the production of the radioactive ion beam (RIB), the principles of the optical polarization of the ^8Li probe will be described, and then the basics of β -NMR data collection and analysis will be detailed. This chapter ends with a discussion of three topics important to β -NMR: rf power-broadening of resonances, the macroscopic demagnetization correction to the shift of a resonance, and the effect of a quadrupolar interaction on the resonance spectrum.

2.2 Production and polarization of ^8Li

2.2.1 Isotope production

RIBs are produced at ISAC using the 500 MeV proton beam from the TRIUMF cyclotron (the actual accelerated species are H^- ions; the electrons

are stripped by graphite foils before the protons enter the beam line). The proton beam is used to drive a secondary RIB using the ISOL (isotope separation on-line) technique. The high-energy protons bombard a target (typically SiC or Ta) and induce various spallation reactions. The isotopes produced diffuse out of the target, promoted by maintaining the target at a high temperature (~ 2500 °C). The nuclides are then ionized by contact with a heated tungsten extraction tube (this works well for species with low ionization energies, like the alkalis). The target is typically held at a voltage of 28–30 keV. The nuclides thus escape the target with this energy, having a spread of 1–2 eV. This small energy spread is important for subsequent transport and optical polarization with high efficiencies. The production of radioactive isotopes is accompanied by high radiation fields, and therefore, the entire target stations are located underground, shielded from the experiment hall.

After extraction from the target and ionization, a beam of the desired isotope is obtained using mass separators. These are essentially a series of magnetic fields that causes a deflection of the ions' path based on their mass-to-charge ratio. This occurs in stages; in the first a coarse separation is achieved, while in the second, a pair of magnets provides a very high resolution of mass separation. The resolution of the ISAC mass separators is more than enough for a light isotope like ^8Li (there are no stable isobars with this mass number for which ^8Li is the longest-lived radioactive species).

Upon exiting the mass separators, the ion beam is then directed above ground to the appropriate experiment station. Transport of the beam is accomplished using electrostatic focussing and “steering” elements. The entire beam line is maintained under high vacuum.

2.2.2 Polarization of the ^8Li nuclear spin

β -NMR relies on the ability to regularly achieve a high degree of nuclear polarization. In this regard, the process of polarizing the probes underpins the technique. The radioactive ion beam for β -NMR is polarized by optical pumping using circularly polarized light; a process suggested by A. Kastler

2.2. Production and polarization of ${}^8\text{Li}$

in the early 1950s, that is particularly suited to atoms like alkalis[199, 200]. At ISAC this nuclear polarization is accomplished using in-flight, collinear optical pumping[201]. The overall process involves three main steps[201]: neutralization of the ${}^8\text{Li}^+$ ions; optical pumping of the neutral atoms using a counter-propagating, circularly polarized, resonant laser beam; followed by re-ionization of the atoms. The important points of the process are described below, aided by the optical pumping scheme for the ${}^8\text{Li}$ atom and the layout of the ISAC polarizer, shown in Fig. 2.1 (a) and (b), respectively.

The ${}^8\text{Li}^+$ ions are first neutralized resulting in a beam of ${}^8\text{Li}^0$ (valence electron configuration $2s^1$). This is achieved by passing the beam through a cell of Na vapour, typically held at about 480°C . ${}^8\text{Li}^+$ has a large cross section for charge exchange with Na[163], and under typical conditions the beam is neutralized with $\sim 50\%$ efficiency. The neutral beam then drifts through the optical pumping region (1.7 m in length) in the presence of a small, longitudinal magnetic holding field of 1 mT, maintaining the nuclear polarization axis. Situated in the drift region is an electrostatic deflection plate that removes any ions that exit the Na cell without becoming neutralized.

Atomic excitation occurs along the drift region through the interaction of the beam with the counter-propagating laser that is right- or left-handed circularly polarized with respect to the magnetic holding field/beam momentum axis. Atomic excitation occurs by irradiating the Li $D1$ transition between the ${}^2S_{\frac{1}{2}}$ ground state and the ${}^2P_{\frac{1}{2}}$ first excited state that occurs at a wavelength of 671 nm. The optical pumping is carried out by a single-frequency dye laser that is itself pumped by a Nd:YAG laser. The laser laboratory is located under the experiment hall and the light is directed by mirrors up to the beam line. A linear polarizer in combination with a remotely-controlled quarter-wave plate allow for switching of the helicity (positive or negative) of the excitation light (i.e., right- or left-handed circular polarization) before it enters the beam line.

As shown in Fig. 2.1(a), both the ${}^2S_{\frac{1}{2}}$ ground state and ${}^2P_{\frac{1}{2}}$ first excited state are split by interaction of the single valence electronic spin with the ${}^8\text{Li}$ nuclear spin ($I = 2$) giving rise to two hyperfine levels that correspond

2.2. Production and polarization of ^8Li

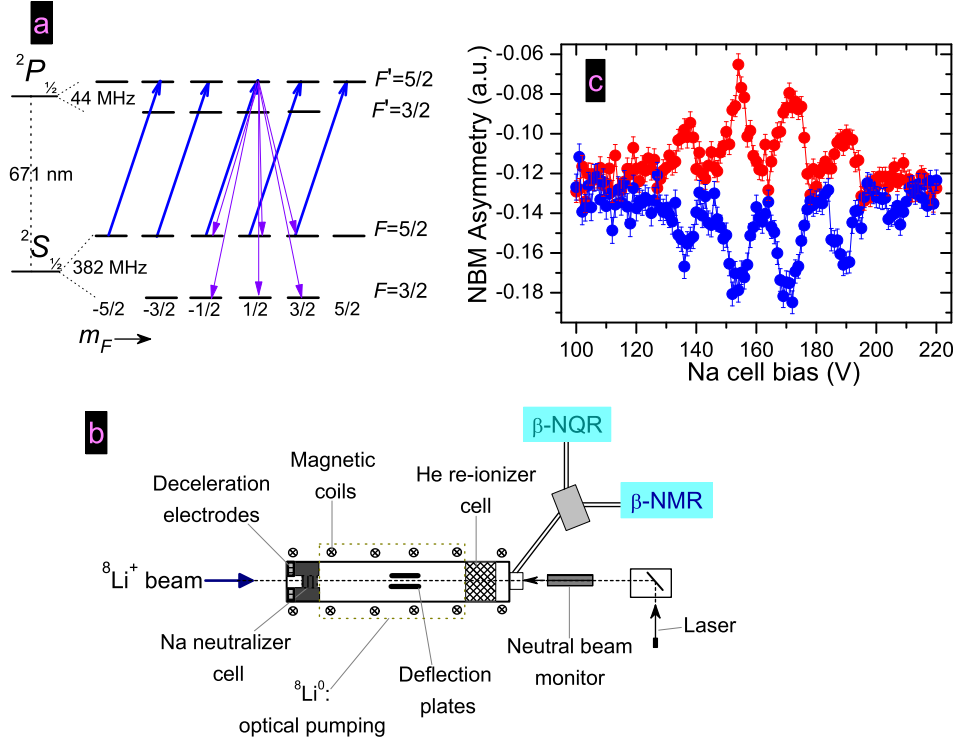


Figure 2.1: (a) Optical pumping scheme for the $D1$ line of ^8Li showing the $2S_{1/2}$ ground state and the $2P_{1/2}$ first excited state. The excitation induced by the laser is shown by heavy arrows, and the spontaneous emission by the thin arrows (for clarity, the latter is shown for only one excited state). Adapted from Ref. [202]. (b) Schematic layout of the ISAC collinear optical polarizer. (c) Representative asymmetry versus voltage scan used to tune the Na cell deceleration electrodes to maximize polarization of the beam.

2.2. Production and polarization of ^8Li

to the spin state of the valence electron: $F = (I + J)$; $F^{(l)} = \frac{3}{2}, \frac{5}{2}$. The splitting is 382 MHz in the ground state and 44 MHz for the excited state. In the presence of the ~ 10 G external holding field, the hyperfine levels are further split into four ($F = \frac{3}{2}$) and six ($F = \frac{5}{2}$) sublevels, according to their magnetic quantum numbers m_F . Since the field is small, these sublevels are almost degenerate with respect to the hyperfine splitting[202]. Absorption of a photon of, e.g., positive helicity, excites the Li atom from the ground state according to the selection rule $\Delta m_F = +1$, and the atoms decay by spontaneous emission according to the selection rule $\Delta m_F = 0, \pm 1$. After many cycles of excitation and emission, the angular momentum carried by the absorbed photons is transferred to the atoms[199, 200, 202]. The resonant atoms are thus “pumped” towards increasing atomic (and nuclear) polarization, i.e., increasing m_F . The lifetime for spontaneous fluorescence of the excited state is about 50 ns, which is short compared to the transit time through the optical pumping region ($\sim \mu\text{s}$). Consequently, when the atoms reach the end of this region, they have undergone multiple pumping cycles and are highly polarized; the majority occupy the ($F = \frac{5}{2}, m_F = +\frac{5}{2}$) state corresponding to the nuclear spin state $m_I = +2$ [163, 202], which is antiparallel to the beam momentum. Thus, if the excitation light is of negative helicity ($\Delta m_F = -1$), the nuclear spin state is $m_I = -2$, parallel to the beam momentum as a result of pumping to the ($F = \frac{5}{2}, m_F = -\frac{5}{2}$) state [i.e., for this case the heavy arrows in Fig. 2.1(a) point to the left].

The last step is to re-ionize the beam by passing it through a cell of He gas, ionizing the $^8\text{Li}^0$ with an efficiency of $\sim 50\%$. This allows for electrostatic steering/focussing of the now spin-polarized $^8\text{Li}^+$ beam. The nuclear polarization is preserved during the stripping process. Two 45-degree electrostatic bends that preserve the longitudinal nuclear polarization are located immediately after the He cell. Any Li not re-ionized are unaffected by the first of these bends, and instead continue in a straight path into the neutral beam monitor (NBM). This apparatus is comprised of a metal foil in a 20 mT longitudinal holding field. There is an aperture in the foil through which the laser beam passes into the beam line. Two detectors in a backward-forward geometry (same as that of the β -NMR spectrometer

described in following Section), are used to monitor the polarization and relative intensity of the neutral beam, and as such, the NBM provides an important diagnostic of the ${}^8\text{Li}^+$ beam used in the experiments.

A couple of important aspects of the optical pumping process also deserve mention. In order to maximize the nuclear polarization, pumping of both hyperfine levels of the ${}^2S_{\frac{1}{2}}$ ground state simultaneously is required, and this is achieved by modulating the frequency of the laser[201, 202]. The laser is passed through an electro-optic modulator (EOM) operating at the hyperfine splitting to generate first-order sidebands at that frequency and broaden the effective bandwidth of the pumping light. Additionally, the resonant absorption frequencies of the Li atoms become Doppler-broadened since they are emitted from the target with a distribution of thermal energies. For an ion beam of energy E_i , with a width of ΔE_i , the Doppler width of the absorption frequency $\Delta\nu^*$ can be described by[163] $\Delta\nu^*/\nu^* \propto \Delta E_i/\sqrt{E_i}$. Recall from above, for the ${}^8\text{Li}$ beam $E_i=28\text{--}30$ keV with $\Delta E_i \approx 2$ eV, and so accelerating the beam reduces the relative Doppler broadening thus reducing the required laser power[163]. However, Doppler broadening also occurs due to the multiple collisions with the Na atoms of the neutralizer which can be ~ 100 MHz[201]. This broadening is significant enough to prevent the resolution of the first excited state hyperfine splitting[202]. To overcome this, after the laser passes through the first EOM, it then passes through two more EOMs operating in series at 28 and 19 MHz which generate higher-order sidebands. The result is multiple sidebands with a spacing ~ 10 MHz, and this allows for the Doppler-broadened absorption spectrum to be covered by the excitation light[201].

In order to maintain a high degree of nuclear polarization the laser frequency must remain stable over the course of spectra collection. This is accomplished by the use of an interferometry (etalon) feed-back system based on the frequency difference between the dye laser and a frequency-stabilized HeNe laser. This prevents the excitation frequency from drifting more than a few MHz per day[201]. Once the laser is tuned and stabilized, the atomic beam energy is fine-tuned in order to match the Doppler shifted absorption resonance to the laser frequency. This is done by scanning the beam en-

2.3. The β -NMR spectrometer

ergy through the use of deceleration electrodes located at the entrance of the Na cell. Fig. 2.1(c) shows an example of such a scan, where the asymmetry from the two laser helicities (proportional to the optically-generated nuclear polarization) measured at the NBM is plotted against the deceleration bias voltage applied to the electrodes. The multiple peaks originate from scanning of the ground state hyperfine levels across the sidebands of the excitation laser; the largest peaks corresponding to the pumping of both levels[201, 202], which determines the bias value for maximal polarization. Should the laser need to be re-tuned, the Na cell bias scan is re-performed to determine the new optimal voltage. The example in Fig. 2.1(c) is quite typical; the applied deceleration voltage is generally ~ 0.1 kV, a small correction to the nominal Li beam energy.

The continuous-wave laser power used is typically ~ 100 mW. Nuclear polarization $\sim 70\%$ is routinely obtained; while values as high as 80% are attainable, but at the expense of overall ion beam intensity. This value of the nuclear polarization produced is expressed in terms of the normalized nuclear magnetic sublevel population[202]

$$\mathbf{P} = \frac{1}{I} \sum_m m p_m, \quad (2.1)$$

where m is the nuclear magnetic quantum number and p_m is the population of the corresponding sublevel. The vector polarization being defined with respect to the longitudinal holding field taken along the \hat{z} direction. As described in the next Section, the same longitudinal geometry applies to the spectrometer; the optically-generated nuclear polarization along this direction is denoted by P_0 .

2.3 The β -NMR spectrometer

The spectrometer is of longitudinal design, i.e., the beam axis (and nuclear polarization) are collinear with the external magnetic field H_0 ; see Fig. 2.2(a). The spectrometer operates under ultra-high vacuum (UHV, $\lesssim 10^{-9}$ Torr). This is an important requirement, otherwise the Li ions (and emitted

2.3. The β -NMR spectrometer

β -electrons) would stop in contaminant, residual gases (easily condensed at cryogenic temperatures). This spectrometer is also known as the “high-field” spectrometer as H_0 can be as large as 9 T. The field is produced by a high-homogeneity superconducting solenoid. Broadly, in addition to the solenoid, the other important components of the spectrometer are the He cold-finger cryostat (3–310 K), a coil to apply the radio-frequency H_1 (associated frequency generator and amplifier), and two fast plastic scintillator detectors. The layout of the spectrometer is sketched in Fig. 2.2(a); a schematic may be found in Ref. [163]. Side-view images of the spectrometer, and an axial view image of the cryostat (outside the UHV chamber) are also displayed in Fig. 2.2.

The two detectors are located upstream (backward) B , and downstream (forward) F of the sample. As the probes’ momentum is longitudinal to H_0 , the ions must enter the spectrometer and reach the sample by passing through a 1.5 cm aperture in the B detector. Both detectors are made from (Bicron BC412) plastic. Note Fig. 2.2(a) is not to scale; in reality the B detector is outside the solenoid, further away from the sample than the F detector. Thus, the solid angles subtended by the detectors are different, resulting in different efficiencies. However, the presence of a high magnetic field has a focussing effect on both the incoming $^8\text{Li}^+$ and the emitted betas, resulting in a circular motion of the particles perpendicular to the field; i.e., a helical trajectory[157] that confines them along the axis of the solenoid. This effectively increases the solid angle of the B detector such that the efficiencies of the two detectors are similar when the applied field is above about 1 T.

These are telescope scintillator detectors. The photons generated when β -electrons strike the plastic are transmitted via lucite light-guides to photomultiplier tubes (PMTs). These in turn convert the optical signal into an electrical pulse to be digitized for computer storage. The detectors and their light-guides are housed in stainless steel, with thin stainless steel windows (0.05 mm thick) through which the MeV β -electrons can easily pass. This casing isolates the detectors from the UHV.

The cryostat is attached to a motorized bellows that allows it to be

2.3. The β -NMR spectrometer

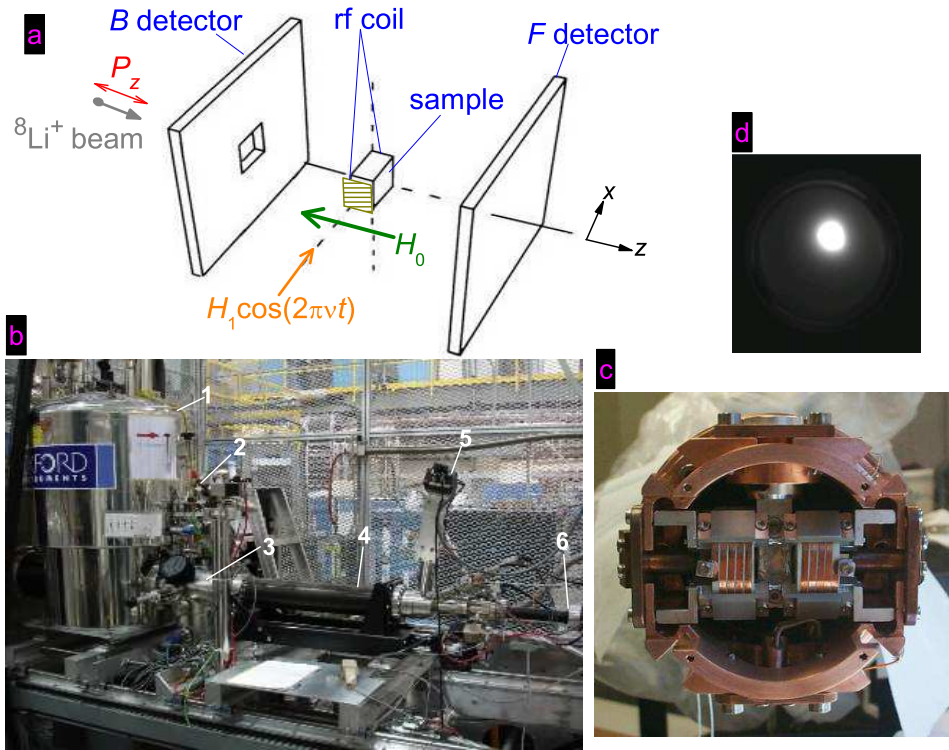


Figure 2.2: (a) Schematic of the β -NMR spectrometer components. (b) The spectrometer, taken inside the HV isolation cage with the cryostat retracted from the bore of the magnet; 1: superconducting solenoid; 2: sample load-lock; 3: UHV chamber; 4: cryostat bellows; 5: liquid He transfer line inlet; 6: Front detector PMT (in this image the Back detector is upstream of the solenoid and is not visible). (c) Axial view of the end of the cryostat (outside UHV) showing the sample position and the rf coil around it. (d) Representative beam spot imaged on a sapphire disk at high field.

retracted from, or inserted into, the bore of the superconducting solenoid. This allows access to the sample through a load-lock such that samples may be changed without the need to vent the entire UHV chamber. The sample holder port in the cryostat is keyed such that only the front of the sample faces the ion beam.

As mentioned in the previous Chapter, an important capability of the β -NMR spectrometer is the electrostatic deceleration of the ${}^8\text{Li}^+$ beam, thereby allowing for variable implantation depth and thus depth-resolved measurements. Deceleration is accomplished by placing the entire spectrometer and associated electronics on a high-voltage platform that is electrically isolated from ground. The bias voltage is thus an adjustable electrostatic barrier (up to 30 kV) that the Li ions must overcome, reducing their momentum before they reach the sample. For safety purposes, the platform and components on it, are housed in an interlocked “cage,” portions of which are visible in Fig. 2.2(b).

2.3.1 Some comments on beam spot tuning

As discussed above, after exiting the He re-ionization cell of the polarizer the beam is transported and focussed onto the sample by means of the electrostatic beamline optics. Directly upstream of the spectrometer is a series of three variable-width collimators through which the beam passes before travelling through the B detector hole and the final Einzel lens. This Einzel lens and the strong fields of the solenoid are used to focus the beam onto the sample. Ideally, a tightly-focussed and centred beam spot is desired. Typically, the beam spot is circular and ranges between 2–3 mm in diameter.

For a given ion energy, the size and location of the beam spot are quite sensitive to the applied Einzel lens voltage (≤ 20 kV) and the external field. When the external field is high (> 0.3 T), the Einzel voltage is restricted due to electric discharge problems; since experiments with the β -NMR spectrometer frequently utilize large H_0 , it is the solenoid that provides most of the final focussing.

Time is invested at the outset of all experiments to ensure the optics

of the entire beam line are tuned to provide the best beam spot under a variety of conditions, e.g., various fields and/or platform biases. To verify the position and size of the beam spot relative to the sample, images of the spot striking a crystalline sapphire disk (which is found to scintillate) are taken using a CCD (charge-coupled device) camera. The sapphire disk is mounted at the end of the cryostat and can be rotated in front of the sample when the cryostat is retracted [not shown in Fig. 2.2(c)]. The camera is mounted upstream of the sample, normal to the beam axis. Images of the beam spot are recorded by reflecting the scintillation light toward the camera using a mirror also mounted inside the beam line. An example of such an image is shown in Fig. 2.2(d). By removing the scintillator disk, and using illumination provided by LED lights located inside the beam line, similar images of the sample itself may be collected. The camera software allows for quantitative comparisons of the sample and beam spot centres.

In general, when the spectrometer bias is raised to lower the incident energy, the spot tends to become more diffuse. The combination of magnetic field from the solenoid and the beam energy determine the beam envelope function which oscillates along the trajectory toward the sample. A beam transport simulation program has been developed at ISAC that can successfully predict combinations of “magic fields” and final energies for which the beam envelope is a minimum (a node) at the the plane of the sample. For this reason, spectra are collected at particular combinations of H_0 and E_{Li} .

2.4 Data collection and analysis

In this Section, a general description of the procedures for recording resonance spectra (a function of frequency), and spin-lattice relaxation spectra (a function of time) are described. However, for both types of spectra, the important observable is the asymmetry A in the detector counts. As mentioned previously, this asymmetry is a result of the nonconservation of parity in β -decay, and is thus pivotal to β -NMR.

In Fig. 2.2(a), the large, static external field H_0 defines the polarization axis \hat{z} to which the ${}^8\text{Li}^+$ nuclear polarization is collinear. As described above,

depending on the helicity of the laser light, the ions are either implanted with their polarization parallel or antiparallel to their momentum. For ${}^8\text{Li}$ the β -electrons are emitted preferentially *opposite* to the nuclear polarization. Referring to Eq. A.9 [and Fig. A.2(b)], for the longitudinal geometry of the β -NMR spectrometer (detection angles 0° and 180°), the β -electron count distribution in the two detectors follows[202, 203]

$$N_{F(B)} = \alpha_{F(B)}[1 \pm \mathcal{A}P], \quad (2.2)$$

where $N_{F(B)}$ is the number of counts at a given detector, \mathcal{A} for ${}^8\text{Li}$ is $-\frac{1}{3}$ [201], and the constant $\alpha_{F(B)}$ is an experimental factor that takes into account the detector geometry and efficiencies.

The measured asymmetry in the β -electron counts is thus directly proportional to the nuclear polarization. The resulting normalized count asymmetry is defined as

$$A^{+(-)} = \frac{N_F - N_B}{N_F + N_B}, \quad (2.3)$$

where $A^{+(-)}$ is the asymmetry of the individual helicities. To produce a single spectrum, the separate helicities are combined according to

$$A = A^+ - A^-. \quad (2.4)$$

Data is recorded in the two helicities to overcome differences in the geometries of the two detectors, allowing for a better defined asymmetry. Multiple scans are accumulated alternately in the two helicities in order to improve signal-to-noise. The scans in a given helicity are averaged prior to combination into a single spectrum. Individual scans in either helicity can be viewed separately and those that are of poor quality are discarded prior to averaging.

2.4.1 Resonance spectra

In order to record spectra as a function of frequency ν , a small, oscillating rf field H_1 is applied normal to the polarization direction, along \hat{x} ; see Fig.

2.2(a). Here, resonance data are collected with the rf applied continuously (continuous-wave, cw-rf mode). In this mode, the Li ions are implanted continuously and the frequency is stepped at regular intervals through the desired range around ν_L . The frequency is stepped slowly (~ 1 s/value) compared to the ^8Li lifetime in order to avoid distortions to the resonance due to ions persisting in the sample from previous frequency steps; when $\delta\omega/\delta t \ll \Delta\nu/\tau$, where $\Delta\nu$ is the linewidth, there will be no hysteretic distortion[204]. As such, a given frequency is applied for a time corresponding to many cycles (continuous-wave), $\mathbf{H}_1(t) = H_1 \cos(\omega t)\hat{x}$, where the angular frequency ω equivalent to $2\pi\nu$; H_1 is typically tens of μT . In contrast to modern, conventional NMR measurements which are typically performed using pulsed methods, the amplitude of H_1 available with the β -NMR spectrometer is limited, so the cw-mode gives better signal-to-noise, especially for broad resonances.

The rf (from frequency generator and amplifier) is applied via a non-resonant coil (approximately Helmholtz; impedance of 50 Ohms) that straddles the sample; see Fig. 2.2(c). The rf power P_{rf} determines the amplitude of the applied field: $H_1 \propto \sqrt{P_{\text{rf}}}$. The power is monitored at a power-meter attached via a directional coupler before the rf coil, and via a pick-up antenna coil adjacent to the sample.

The polarization of implanted ions depends on the ^8Li lifetime τ and processes that cause relaxation of the polarization, i.e., T_1 . For a continuous beam of ions that are implanted at a constant rate \mathcal{R} , the polarization in the sample averaged over all times approaches an equilibrium value,

$$\bar{P} = \frac{P_0 \mathcal{R} \int_0^\infty e^{-t/\tau} e^{-t/T_1} dt}{\mathcal{R} \int_0^\infty e^{-t/\tau} dt} \quad (2.5)$$

$$= \frac{P_0}{1 + (\tau/T_1)}, \quad (2.6)$$

where P_0 is the initial nuclear spin polarization [Eq. (2.1)]. The β -electron counts are proportional to this polarization through Eq. (2.2) and yield the observed asymmetry per frequency step $A^{+(-)}(\nu)$ from Eq. (2.3). When the rf field is on resonance with the ^8Li in the sample it induces precession

of the polarization in a plane normal to H_1 including the two detectors ($\hat{y}\hat{z}$). The rapid precession during the integration time results in a loss of polarization; the distribution of the emitted β -electrons becomes more isotropic, i.e., there is a *decrease* in the observed asymmetry. An example of this type of resonance data recorded in a single crystal of MgO is shown in Fig. 2.3.

The importance of a well-defined, off-resonance asymmetry value is that it becomes the “baseline” for any signals in the spectrum. From Fig. 2.3, the baseline asymmetry in the combined spectrum A_0 is easily seen to be the result of the combination of the baseline asymmetries in the individual helicities $A_0^{+(-)}$, i.e., Eq. (2.4). When the individual helicities are displayed together [as in panel (a)], on resonance $A^{+(-)}$ do not approach zero, but rather a constant off-set from zero; however, it is the absolute changes in asymmetry that are important. In the *combined* spectra, the asymmetry always decreases to approach zero on resonance.

Gaussian and/or Lorentzian lineshapes[205] are used as the fit functions for resonances. Unless stated otherwise, all linewidths are taken as the full-width at half-maximum (FWHM).

Under similar beam spot and polarization conditions, spectra recorded at different external variables (e.g., temperature, H_0) may be concomitant with a change in $A_0^{+(-)}$ from any dynamic processes contributing to spin relaxation in the sample. In order to compare spectra more directly they will often be presented normalized to the baseline A_0 . The resulting normalized amplitudes (fractional losses of asymmetry) are more easily quantitatively compared. In terms of the raw asymmetry values, the normalized amplitude is $1 - (A_r/A_0)$, where A_r is the asymmetry value at the peak of the resonance. If the raw A_r is zero, the resulting normalized amplitude will be 1, and the resonance is said to be saturated, corresponding to the complete depolarization of all implanted ions.

Lastly, in a static approximation, the area of a resonance may be taken to be proportional to the number of spins contributing to it (for constant H_1). Here, the resonance area Λ (for any lineshape) is simply approximated by the product of the normalized amplitude with the FWHM.

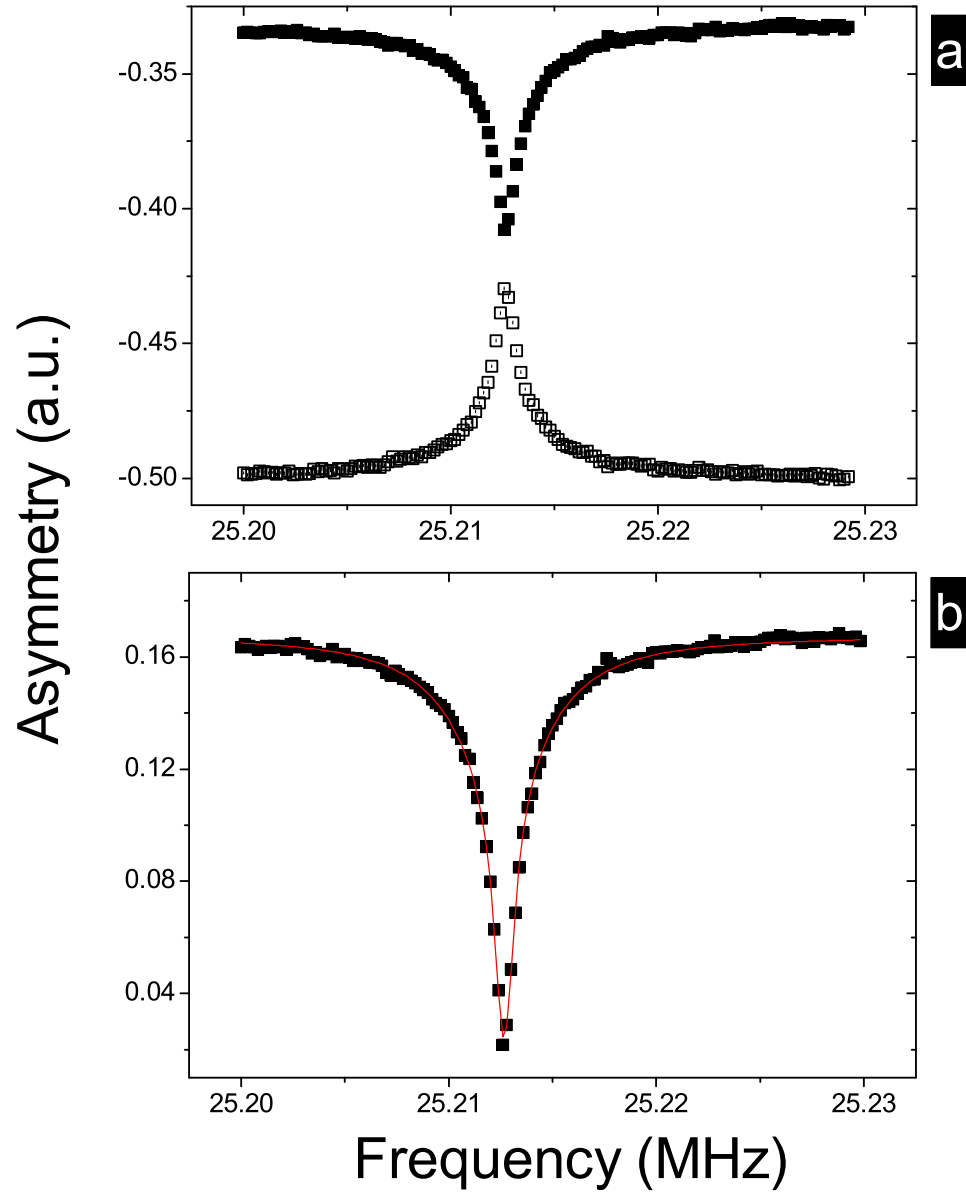


Figure 2.3: Representative resonance spectra recorded in a (100) crystal of MgO for $H_0 = 4$ T at room temperature. Top panel shows the averaged spectra in the separate helicities and the bottom panel shows the spectrum after combination.

The beam spot is quite sensitive to instabilities throughout the beam line, such as transient spikes in the voltages applied to electrostatic transport elements, or small fluctuations in temperature at the Na vapourizer. These can cause the beam spot to shift position on the sample during the collection period of a cw-rf mode spectrum, i.e., multiple frequency scans in each helicity generally requiring tens of minutes. Variations in the beam spot on the sample may give rise to fluctuations in the polarization, introducing significant noise or distortions into a spectrum, sometimes making it difficult to define a flat off-resonance A_0 , or identify resonances of small amplitude.

2.4.2 Spin-lattice relaxation spectra

The spin-lattice relaxation rate $T_1^{-1} \equiv \lambda$ is extracted from spectra that monitor the polarization of the implanted ions as a function of time in the absence of the rf field. These time-differential spectra follow the same principles of detection as those described above for resonances: The counts from the two detectors can be used to generate an asymmetry that is directly proportional to the Li nuclear polarization $P(t)$. Again, spectra are recorded in the individual helicities, then separate helicity spectra are averaged and subsequently combined [Eqs. (2.3) and (2.4)].

The beam is introduced in short pulses of length δ . Fig. 2.4 shows an example of these time spectra for $\delta = 0.5$ s and $\delta = 4.0$ s. Following the beam pulse, a counting period of 10 s is used; however, in general, few Li survive for longer than 8 s (making measurements of $T_1 \gg \tau$ difficult). This cycle is repeated every 15 s until sufficient events are accumulated, typically requiring 15–30 mins. $A^{+(-)}(t)$ is measured with a typical time resolution of 10 ms. A pulsed beam is generated by the use of an electrostatic “kicker” located near the target that deflects the beam either into the beam line or to a beam dump. A pulse length of 4 s represents a balance between one which is too short ($\delta = 0.5$ s) or one which is unnecessarily long.

To fit data for $\delta = 4.0$ s, a general spin relaxation function $f(t, t'; \lambda)$ is as-

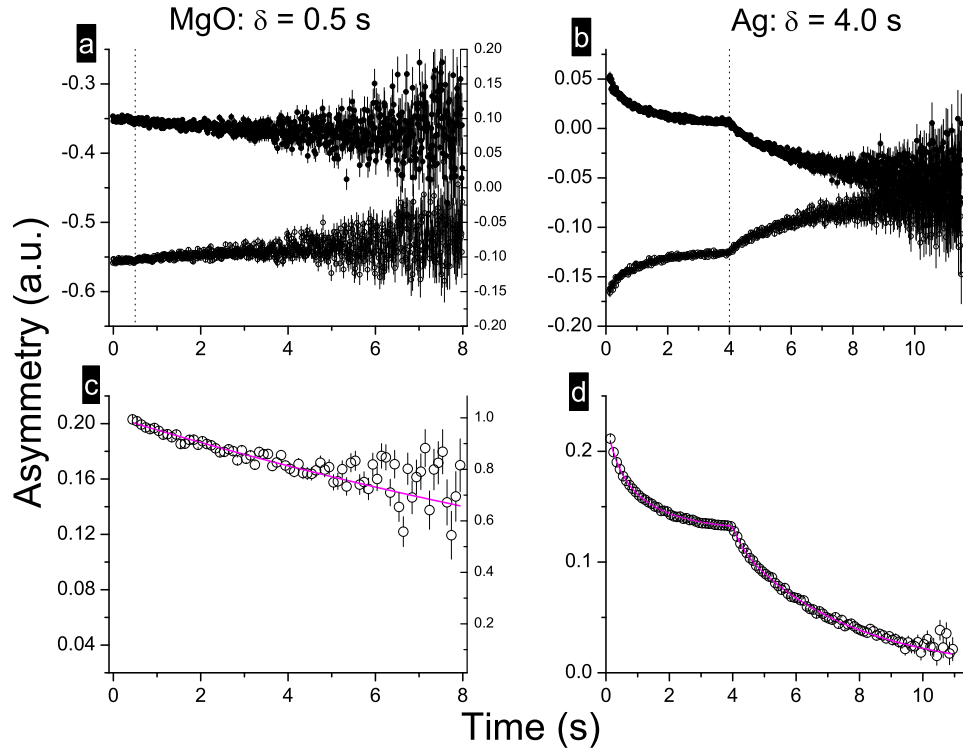


Figure 2.4: Representative spin-lattice relaxation spectra. (a) and (c), Spectrum recorded in a (100) crystal of MgO at room temperature and $H_0 = 3$ T using $\delta = 0.5$ s; (b) and (d), spectrum recorded in Ag foil at 250 K and $H_0 = 15$ mT using $\delta = 4.0$ s. The top panels show the averaged spectra in the separate helicities; while the bottom panels show the combined spectra after binning.

2.4. Data collection and analysis

summed for the ions implanted at t' , then the average polarization follows[206]

$$P(t) = \begin{cases} \frac{\int_0^t e^{-(t-t')/\tau} f(t,t';\lambda) dt'}{\int_0^t e^{-t'/\tau} dt'} & t \leq \delta \\ \frac{\int_0^\delta e^{-(\delta-t')/\tau} f(t,t';\lambda) dt'}{\int_0^\delta e^{-t'/\tau} dt'} & t > \delta. \end{cases} \quad (2.7)$$

One example of $f(t, t'; \lambda)$ is the biexponential form[206],

$$f(t, t'; \lambda) = A_1 e^{-\lambda_1(t-t')} + A_2 e^{-\lambda_2(t-t')}. \quad (2.8)$$

For instance, the Ag spectrum in Fig. 2.4(d) was fit using two components according to the above two equations. The second component is a small amplitude, faster relaxing one that is often needed to properly account for T_1^{-1} data at short times in many materials.

In contrast, the MgO spectrum in Fig. 2.4(c) was fit to a single exponentially relaxing component after the beam pulse only

$$A = A_\delta e^{-\lambda(t-\delta)}, \quad (2.9)$$

where A_δ is the asymmetry at the trailing edge of the beam pulse. The above equation can also be generalized to multiple components; however, the MgO spectrum shown could be fit satisfactorily to a single relaxing component. Notice that the relaxation in MgO is slow (practically non-relaxing) even at room temperature, as expected for a non-magnetic insulator with no conduction electrons.

The combined spectra in panels (c) and (d) of Fig. 2.4 are presented after the data in the time histograms has been further averaged. This process is termed “binning,” and it mainly serves to ease in the visual inspection of the spectra. An integer time factor is chosen over which the data is averaged. In both spectra in question, this binning factor was 10; the $A(t)$ data recorded with 10 ms bins now appears in 100 ms bins (steps). Although seldom done, binning can also be done for resonances where the averaging is done for the asymmetry values over an interval of frequency. Clearly, this improves the

statistics per bin, but the resolution in time or frequency is compromised. Care is always taken to choose a binning factor that is not too large, so as to avoid “binning over” any fine structure in a spectrum.

2.5 Additional considerations for resonance spectra

Here, some additional experimental details that are important to the interpretation of resonance spectra are summarized.

2.5.1 Lineshapes and rf power-broadening

As mentioned above, Gaussian or Lorentzian lineshapes have been used to fit the resonances obtained in the present β -NMR experiments. They are both phenomenological, simple choices of lineshapes that can be used to describe an absorption resonance.

In the absence of other broadening mechanisms, the line broadening in a solid is dominated by the local magnetic field produced by the surrounding nuclear magnetic dipoles. An expression for this broadening due to unlike spins was given in Sec. 1.4 in Eq. (1.43) and is termed the van Vleck dipolar linewidth. It is technically derived from consideration of the second moment of an absorption line due to magnetic broadening from unlike nuclear spins, and is proportional to the width of a Gaussian lineshape. The second moment of a Lorentzian lineshape is undefined. The Gaussian lineshape is thus expected to describe a β -NMR resonance when the only source of broadening is the local magnetic fields due to the host nuclear dipoles[161].

However, in the cw-mode employed here, larger amplitudes of H_1 (i.e., P_{rf}) leads to power-broadening of the resonances. This broadening is temperature-independent (in contrast to the broadening due to dilute magnetic impurities). The broadening due to H_1 gives rise to resonances that are better described by Lorentzian lineshapes. This can be seen by transformation into the rotating reference frame[20, 207], a frame rotating about \hat{z} at the rf frequency $2\pi\nu$. Application of the H_1 causes the spins to precess about

an effective field that is comprised of the now static H_1 and a contribution from H_0 . The applied rf is such that H_1 is of azimuthal orientation in the rotating frame; the spins are considered to be tipped through an angle ϕ by the rf excitation. The effective field about which the spins precess can be obtained from geometric considerations ($\cot \phi$) which yields the form of a Lorentzian. The higher the rf power, the greater the width of the Lorentzian γH_1 .

In the limit of low P_{rf} , an *approximation* for including the contribution from the power-broadening to a Gaussian lineshape is

$$\sigma^2 \approx \sigma_0^2 + (\gamma H_1)^2 + \tilde{\lambda}^2, \quad (2.10)$$

where σ_0 is used to denote the intrinsic width from the host nuclear dipoles, and $\tilde{\lambda} = \tau^{-1} + T_1^{-1}$. For the metals studied here (i.e., Au and Pd) $\tilde{\lambda}$ is at least two orders of magnitude smaller than σ_0 . This point highlights an important difference between present β -NMR measurements and the conventional NMR of molecules in solution. In the latter case, the rapid motion of the molecules leads to an averaging of local fields. In such cases, the Fourier transform of the decay in pulsed NMR measurements will yield the absorption resonance. The β -NMR resonances considered here cannot be obtained through a Fourier transform of the spin-lattice relaxation signal. The above equation is a means of approximating a small Lorentzian broadening to a Gaussian lineshape. It is not rigorously valid when the width of the Lorentzian component becomes comparable to the width of the Gaussian component. In such cases, the lineshape becomes one which is a convolution of a Gaussian with a Lorentzian, which is described by the Voigt function.

2.5.2 Demagnetization correction

In the previous Chapter, the relative frequency shift of the implanted Li probes in metals was discussed as arising predominately from the coupling to the conduction electrons, and as such is interpreted as the Knight shift. Another contribution to this shift arises from the macroscopic demagnetizing field that adds to the local field inside a magnetized material. This is a

classical field that originates from the surface of the sample, and hence is geometry-dependent[21, 162]. For spherical samples, the demagnetization contribution is exactly zero. Thus, in conventional NMR, shifts measured in non-spherical samples can show an orientation dependence of the shift with respect to H_0 [21], e.g., Ref. [208]. In terms of β -NMR in metal films, this contribution to the Li shift is significant when the host metal has a large χ (as in the case of Pd), or is ferromagnetic.

The demagnetization contribution is also approximately zero for thin films when H_0 is parallel to the plane of the film. However, for H_0 normal to the film plane, as in β -NMR, the demagnetization contribution is maximal. Correcting for the demagnetization can be done by noting the analogy between this field and the depolarizing field effect on the local electric field in a polarizable medium[3, 191]. The correction for thin film samples in β -NMR is discussed in detail in Ref. [191].

The total local magnetic field H_t can be divided into four parts:

$$H_{\text{tot}} = H_0 + H_D + H_L + H_{\text{loc}}, \quad (2.11)$$

where H_0 is the applied field, H_D the demagnetizing field, and H_L the field due to the Lorentz cavity. The field H_{loc} is the local field, taken as that dominated by the immediate atomic neighbours of the site under consideration, and is the quantity of interest. The Lorentz cavity is an imaginary sphere (boundary) placed around an atom; the magnetization outside the cavity can be treated in classical continuum theory, while that inside must be treated atomically. Isolating the last three terms on the right-hand side of the above equation and dividing by H_0 gives,

$$(H_{\text{tot}} - H_0)/H_0 = [(H_D + H_L)/H_0] + H_{\text{loc}}/H_0. \quad (2.12)$$

In this equation, the left-hand side gives the observed relative shift, and the second term on the right-hand side corresponds to the corrected shift due only to the local contribution(s). By taking account of the quantity $(H_D + H_L)/H_0$, the measured shift can be corrected.

In the following cgs units are used. For a spherical Lorentz cavity, $H_L = 4\pi M/3$, while $H_D = -\mathcal{N}M$. Here M is the bulk magnetization, and \mathcal{N} is the dimensionless, geometry-dependent demagnetization factor that ranges from 0 to 4π .¹⁰ By treating a thin film as an infinite slab with H_0 normal to the plane, $\mathcal{N} = 4\pi$. Corrections to this value of \mathcal{N} because of the finite size of the sample are proportional to the thickness to lateral dimension aspect ratio ξ_{film} . Samples for β -NMR are $\sim 1 \text{ cm}^2$ and at most hundreds of nanometers thick, thus $\xi_{\text{film}} \sim 10^{-5}$, and the corrections can be neglected. Combining the above expressions yields

$$(H_D + H_L)/H_0 = [-4\pi + (4\pi/3)]M/H_0. \quad (2.13)$$

Noting that $M/H_0 = \chi$, where specifically, it is χ^v the volume susceptibility of the host expressed in emu/cm^3 that must be used. Substituting this result into Eq. (2.12), the demagnetization-corrected Knight shift is given by:

$$K^c = K + \frac{8\pi}{3}\chi^v. \quad (2.14)$$

It is K^c that must be used when applying Eqs. (1.26) or (1.42) to extract values of the hyperfine coupling constant or the Korringa ratio.

2.5.3 Quadrupole splitting

In the previous Chapter, the possible cubic stopping sites in the fcc lattice were discussed and it was stated that at these sites, the EFG at the implanted probe is zero. In general, for stopping sites of non-cubic symmetry, the EFG will be non-vanishing resulting in a quadrupole splitting of the spectrum. The data of this thesis were all collected using large H_0 where the quadrupole interaction can be expected to be a perturbation on the Zeeman interaction (as measured by $\nu_Q/\nu_L \ll 1$). In this case, the quadrupole interaction lifts the degeneracy of the nuclear transitions— in particular for β -NMR— the $|\pm 2\rangle \rightarrow |\pm 1\rangle$ transition.

As a consequence, facile identification of such quadrupolar resonances

¹⁰0 to 1 in SI units.

2.5. Additional considerations for resonance spectra

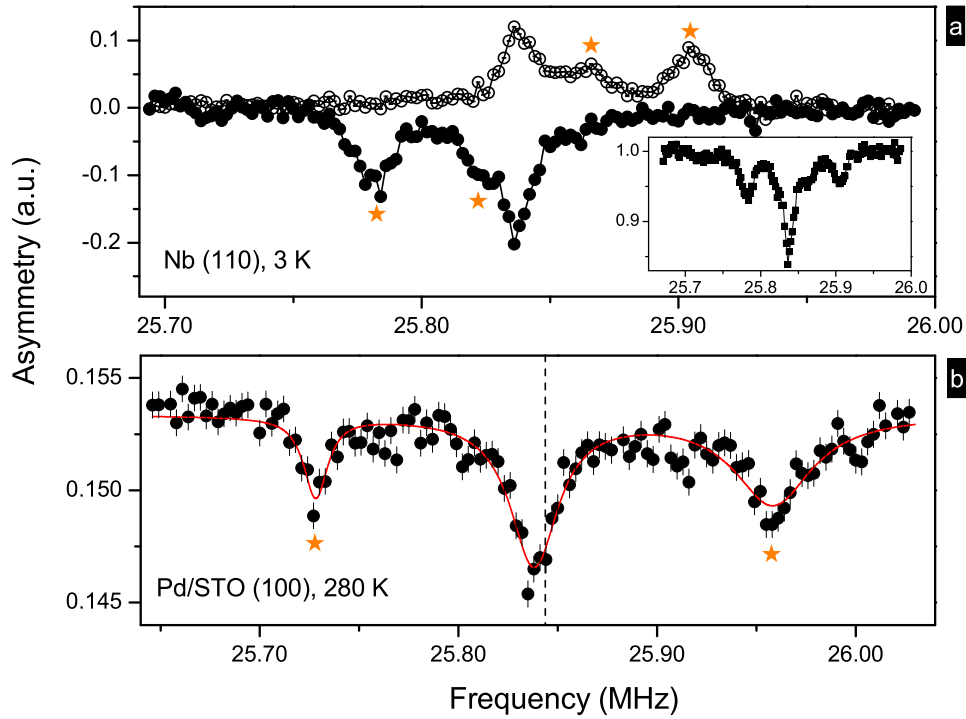


Figure 2.5: In contrast to the resonances recorded in Au and Pd, here are two examples of high field (4.1 T) spectra in which there is a quadrupole splitting. The resonances originating from a quadrupole splitting are labelled with (\star). They are easily identified as they appear at different frequencies in the separate helicities, as illustrated by the spectrum in (a) for $^8\text{Li}^+$ implanted into a film of (bcc) Nb at low temperature. For a discussion of the sites see Ref. [209]. The inset shows the combined spectrum [plotted as A/A_0 vs. Frequency (MHz)]. In (b) the combined spectrum recorded for $E_{\text{Li}} = 28$ keV in a nominally 50 nm Pd film on a STO (100) substrate is shown. The larger resonance is due to ions in the Pd. A quadrupole splitting occurs for the ions stopping in the STO substrate[204]. The centre of the inner satellites shown here provides a way of estimating ν_0 (dashed line). Panel (a) reproduced in part from Ref. [209]. Copyright (2009) by the American Physical Society.

can be made through inspection of the spectra in the separate helicities. This is illustrated by the spectrum recorded in a highly oriented Nb (110) film at 3 K shown in Fig. 2.5(a). The satellites that appear at different frequencies in the opposite helicities can be assigned to ions stopping at a site with a non-vanishing EFG and are marked by (\star). In this example, the larger amplitude resonance that appears at the same frequency in both helicities is from ions stopping in an (essentially) cubic site. Upon combination of the helicities [inset, Fig. 2.5(a)], the quadrupolar resonances contribute to a five line spectrum from $^8\text{Li}^+$ in two distinct sites[209].

Often crystalline SrTiO_3 (STO) is employed as the substrate for thin metal films in β -NMR. In particular, STO is well lattice-matched to Pd[210]. Quadrupole satellites are also seen in high H_0 spectra for ^8Li in STO, regardless of temperature[204]. As an example, a (combined) spectrum recorded at full implantation energy in a nominally 50 nm Pd film deposited onto a (100) single crystal of STO at 4.1 T is shown in Fig. 2.5(b). The inner quadrupole satellites from ions in the STO are marked by (\star), while the larger resonance is from ions stopping in the metal layer. This spectrum serves to illustrate that the centre of the satellites in STO can be used to determine ν_0 . This highlights the use of substrates like STO or MgO as *in situ* reference materials for the determination of the Knight shift. However, comparison of Figs. 2.3(b) and 2.5(b) illustrates that MgO is the preferable substrate for this purpose, as the centre of the quadrupole satellites from STO is less precisely determined.

Inspection of Fig. 2.5 shows, for a given helicity, the size of the quadrupole splitting determined by ν_Q is tens of kHz in Nb, and hundreds of kHz in STO, but in both cases $\nu_Q/\nu_L \ll 1$, so the quadrupole interaction can indeed be treated as a first-order perturbation on the Zeeman interaction, i.e., the “high-field limit.”

With this summary of the technical details completed, the results of ^8Li β -NMR of gold and palladium will now be discussed in turn.

Chapter 3

β -NMR of ^8Li in Gold

3.1 Introduction

The application of low energy ^8Li β -NMR to study the electronic and magnetic properties of multilayers and heterostructures requires an understanding of the behaviour of the probe in simple materials. Such investigations also assist in the overall development of the technique. The Pauli spin susceptibility of the group 11 metals (Cu, Ag, Au) is not temperature-dependent. Thus, the behaviour of ^8Li in these simpler metals can be contrasted with the results presented later for ^8Li in Pd.

In the Introduction the use of thin metal overlayers for proximal magnetometry experiments was discussed. The inertness and high density of Au make it an attractive candidate for such experiments, and as a thin protective capping layer, it may also serve as an *in situ* reference for Knight shift measurements (for samples where no magnetic coupling is to be expected). An important prerequisite is to establish the behaviour of ^8Li in bulk Au. An initial β -NMR study of ^8Li in Au found two resonances with temperature-dependent amplitudes[211], very similar to results from Ag[184]. In this Chapter, significantly more details of the behaviour of ^8Li in Au are presented. A comparison of the hyperfine coupling constants for ^8Li in Au is made with previously reported results for this probe in the other two group 11 metals, Ag[184] and Cu[185], and in Al[186].

3.2 Results

Data is presented from measurements on two distinct samples of Au to verify that the results are intrinsic. The first is a 100 nm film deposited on a

(100) single crystal MgO substrate, equivalent to the one used to record the spectrum shown in Fig. 2.3. This film was grown by thermal evaporation from a 99.99% pure source at a rate of $\sim 4 \text{ \AA/s}$ under a background pressure of 10^{-6} torr. X-ray diffraction shows it is polycrystalline with a preferred orientation along (111). The thickness was estimated using a calibrated thickness rate monitor during deposition. The second is a 25 \mu m 99.99% pure Au foil.

As discussed in Sec. 2.5.1, Eq. (2.10) approximates the three contributions to the linewidth for a Gaussian lineshape. For Au, the dynamic contribution λ is, for all T studied here and $H_0 > 2 \text{ mT}$, at least two orders of magnitude smaller than σ_0 and can be neglected. Thus, it is the γH_1 (Lorentzian) term that dominates the linewidth as P_{rf} is increased. To illustrate this Fig. 3.1 shows the resonances recorded in Au foil at 290 K as a function of H_1 along with the corresponding linewidths σ obtained from a fit to a single Gaussian lineshape. The solid line in Fig. 3.1(b) is a fit to the first two terms of Eq. (2.10) and yields a value of $\sigma_0 = 0.186(5) \text{ kHz}$ at this T . Below about 25 mW ($H_1 \approx 2 \text{ \mu T}$), the width is mostly the H_1 -independent intrinsic σ_0 , principally from the host nuclear dipoles.

Near room temperature, the spectrum of $^8\text{Li}^+$ in Au exhibits a single narrow resonance near ν_0 . This is illustrated in Fig. 3.2 for the 100 nm film on MgO. At this implantation energy only a small fraction of the ^8Li penetrate the Au film and stop in the MgO. Resonances from $^8\text{Li}^+$ in an insulating substrate like MgO provide a convenient *in situ* measure of ν_0 for the determination of the Knight shift [Eq. (1.16)] in β -NMR. Thus, for the resonance in Au at 290 K, the relative shift K is found to be $+63(4) \text{ ppm}$.

The earlier study of ^8Li implanted into a 50 nm Au film on STO at $H_0 = 3 \text{ T}$ found that as T is lowered a second resonance appears at higher frequency and grows in intensity at the expense of the original[211]. This is also observed for the spectra collected as a function of T in Au foil shown in Fig. 3.3. This T -dependence is therefore observed in two distinct samples of Au, indicating that it is intrinsic to isolated $^8\text{Li}^+$ in Au. The second resonance observed upon cooling has a shift of $+131(4) \text{ ppm}$. The shifts are magnetic in origin; there is no evidence of quadrupole splitting in the

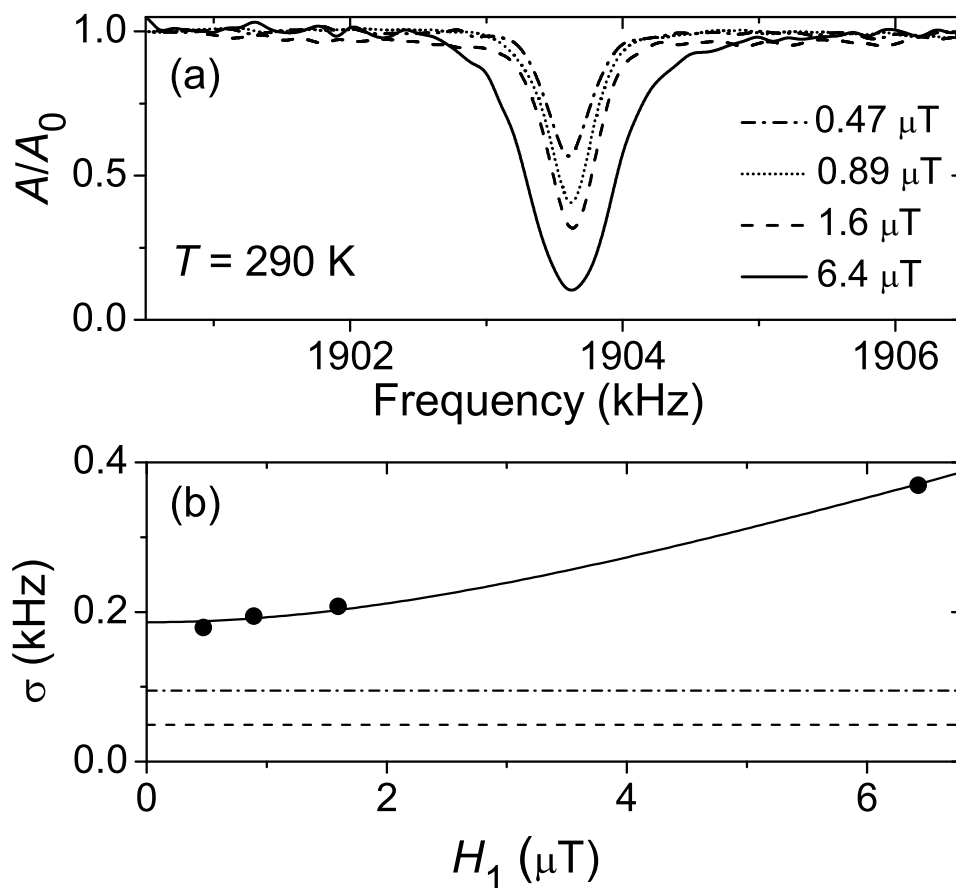


Figure 3.1: (a) Spectra recorded in Au foil ($H_0 = 0.3$ T, $E_{\text{Li}} = 30.5$ keV) as a function of the P_{rf} , the amplitude of H_1 . (b) Gaussian linewidths σ of the spectra in (a). The intrinsic linewidth $\sigma_0 = 186(5)$ Hz from the low power limit. The horizontal lines indicate calculated van Vleck linewidths for the undistorted O (dot-dash line) and S (dashed line) sites. Reproduced from Ref. [212]. Copyright (2008) by the American Physical Society.

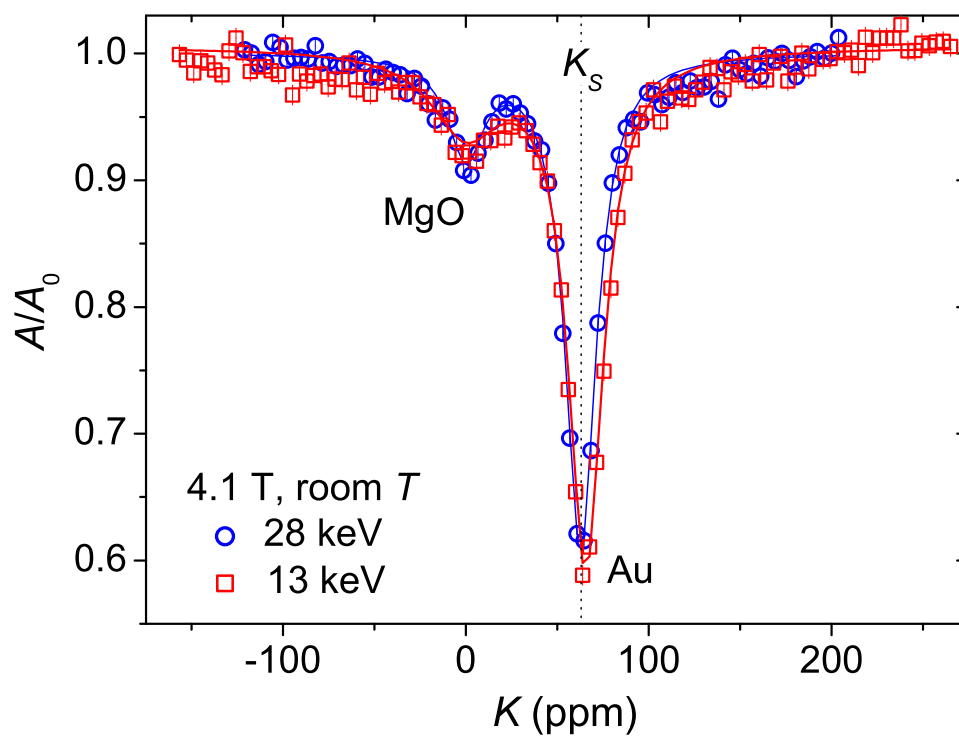


Figure 3.2: Typical high field spectra of $^8\text{Li}^+$ implanted into 100 nm Au/MgO ($H_1 \sim 3 \mu\text{T}$) showing the large resonance in Au and its Knight shift relative to the resonance in MgO. Each spectrum is fit to two Lorentzians. Reproduced in part from Ref. [212]. Copyright (2008) by the American Physical Society.

3.2. Results

separate helicities. By analogy with the behaviour of (i) the T -dependence of the resonances and (ii) the relative magnitudes of K in the other group 11 fcc metals[184, 185], the resonances in Au are provisionally assigned to ions in the octahedral interstitial O site (high frequency line), and the substitutional S site (lower frequency line). These spectra were recorded with $H_1 \sim 5 \mu\text{T}$ and are found to fit well to Lorentzian lineshapes due to the rf power-broadening; cf. Fig. 3.1(b). From these fits, the T -dependence of K , the linewidths (FWHM), and the normalized amplitudes are given in Fig. 3.4. The shifts are T -independent, consistent with Knight shifts. The linewidths are relatively constant with T , with the O line slightly broader than the S line. It is noted that the S widths agree fairly well with the full width (2σ) obtained from the fit in Fig. 3.1(b) for $H_1 = 5 \mu\text{T}$.

The amplitudes of the two resonances show a cross-over centred at $T \approx 200$ K, a somewhat higher temperature than the similar cross-over observed in Ag[184] (≈ 150 K), and much higher than the one observed in Cu[185] (≈ 50 K). As the temperature is further decreased below about 50 K, the narrow O resonance is observed to decrease in amplitude; a similar reduction of the O resonance is seen in Cu[185], but not in Ag[184].

To investigate the possible depth-dependence of the resonances from e.g., a near-surface effect, spectra were collected for several incident energies corresponding to mean implantation depths of 10 to 95 nm, according to the TRIM.SP simulations (see Appendix B). No significant depth dependence of either signal (e.g., width, position) is observed. Spectra recorded in the film at 4.1 T and room temperature for $E_{\text{Li}} = 13$ keV and $E_{\text{Li}} = 28$ keV are compared in Fig. 3.2. At 13 keV essentially no ions should be implanted into the substrate (cf. Fig. B.1), yet a signal from Li in the MgO is still observed, although of reduced amplitude. This is expected as a small area of two diagonal corners of the substrate were masked during the film deposition and remain uncovered by the Au. This indicates the beam spot was not entirely focussed on the Au. At this T , the spectrum is dominated by the signal from ions in the S sites. From Lorentzian fits to the spectra, the linewidths and K for this site are not appreciably different despite E_{Li} , and thus R , differing by a factor of 2.

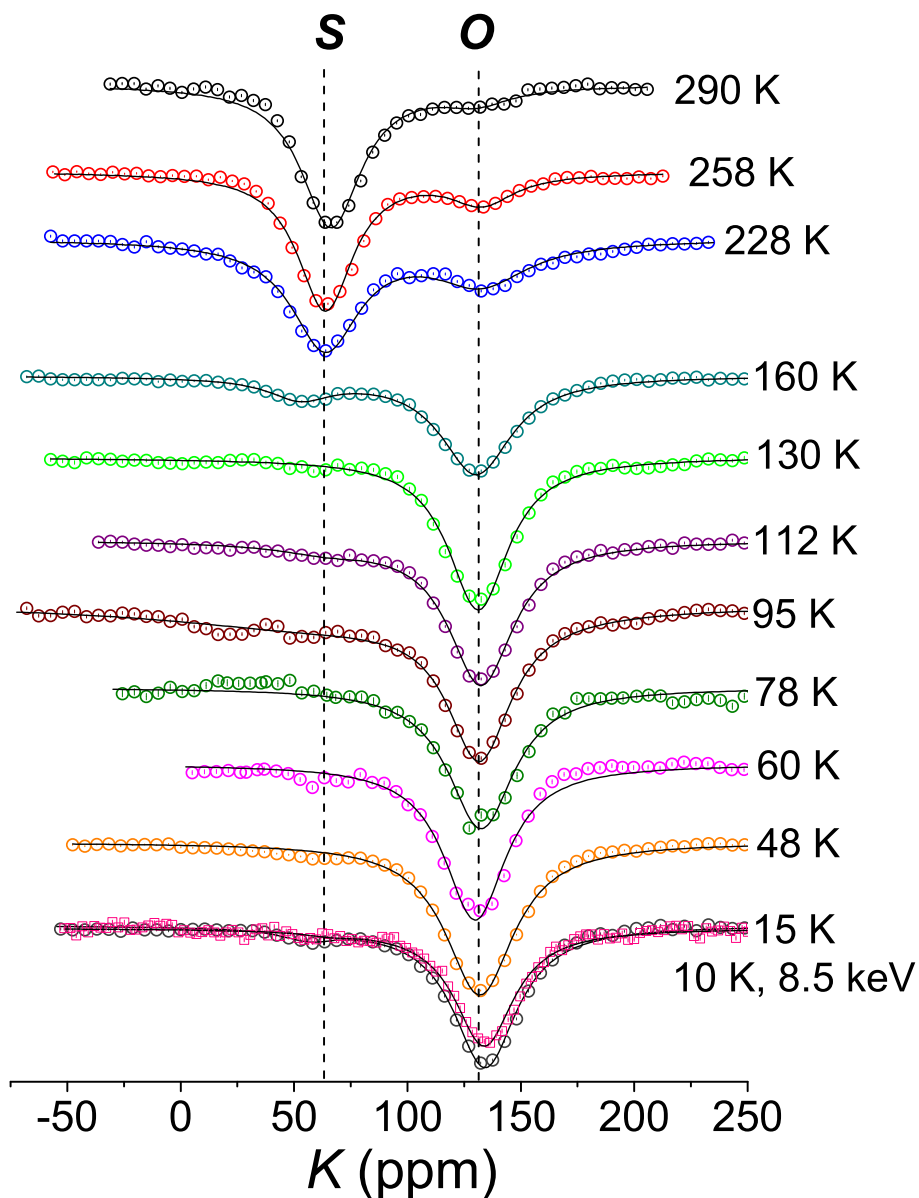


Figure 3.3: Resonance spectra recorded in Au foil for $H_0 = 3$ T, $H_1 \sim 5$ μ T, $E_{Li} = 30.5$ keV (circles); and for $E_{Li} = 8.5$ keV at 10 K (squares). The solid lines are fits using one ($T < 150$ K) or two Lorentzians ($T > 150$ K). The abscissa was set using K_S measured in Fig. 3.2. Reproduced from Ref. [212]. Copyright (2008) by the American Physical Society.

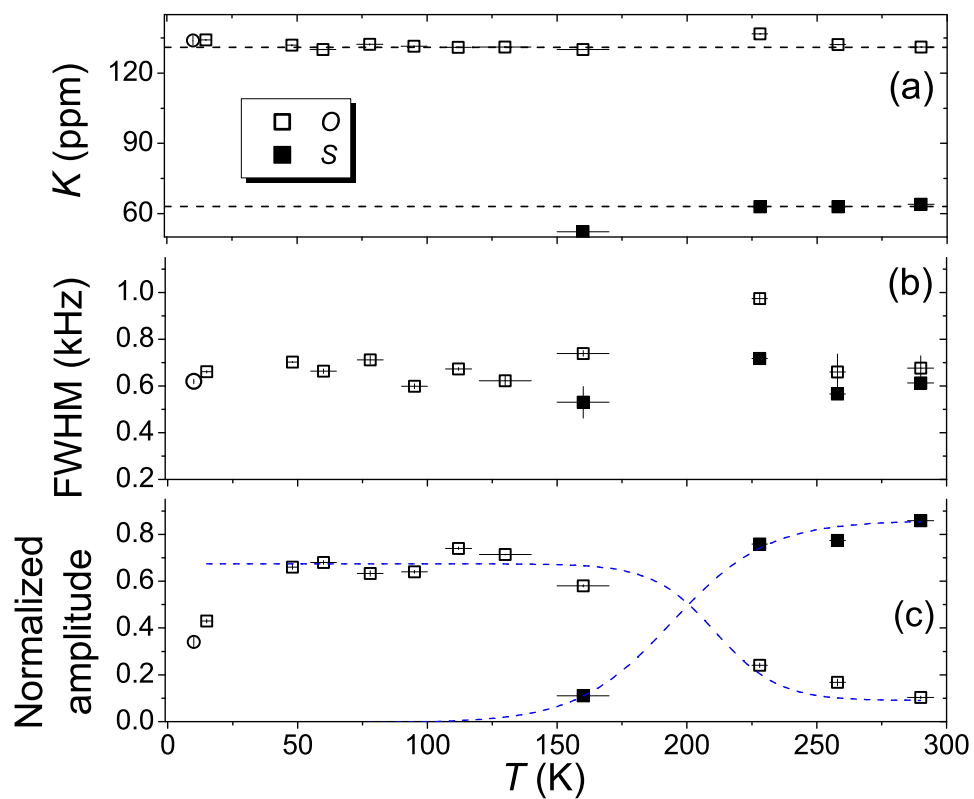


Figure 3.4: Temperature dependence of Knight shifts (a), linewidths (b) and the amplitudes (c), of the 3 T resonances in Au foil from the Lorentzian fits to the data in Fig. 3.3. Circles denote data collected for $E_{\text{Li}} = 8.5$ keV. Reproduced in part from Ref. [212]. Copyright (2008) by the American Physical Society.

3.2. Results

The absence of depth dependence also holds for low temperatures where only the O resonance is observed. Fig. 3.5 shows the results from resonances collected in Au foil below 100 K at $H_0 = 0.3$ T for reduced E_{Li} and low P_{rf} . Again, there is no appreciable difference in the peak position or linewidth when E_{Li} is reduced by a factor of 6. This is also observed at the lowest T in the high field spectra of Fig. 3.3, where the 10 K spectrum collected for $E_{\text{Li}} = 8.5$ keV is the same as that at 15 K collected for full implantation energy. The overall reduction in O signal amplitude for $T < 50$ K at full implantation energy in the 3 T spectra [Fig. 3.4(c)] is also observed at 0.3 T for both full and reduced E_{Li} . This is shown in Fig. 3.5(b) by the filled circles and dashed line for $E_{\text{Li}} = 5.5$ keV, and by the filled triangles for $E_{\text{Li}} = 30.5$ keV.

The O resonances of Fig. 3.5 were recorded for $H_1 \sim 0.5 \mu\text{T}$, and so the rf power-broadening contribution is negligible. Thus, Gaussian lineshapes are found to adequately fit the resonances, and the corresponding linewidths (2σ) are given in Fig. 3.5(b) as open symbols. As previously stated, they do not show a significant dependence on E_{Li} , and overall, they are relatively T -independent. These widths may be regarded as a good approximation to the H_1 -independent intrinsic linewidth for the ions assigned to O sites, giving $\sigma_0^O \sim 0.128(8)$ kHz. In Fig. 3.1(b) an intrinsic linewidth of $0.186(5)$ kHz was determined for resonances at 290 K, i.e., for ions assigned to the S sites. Taken together, the data indicate $\sigma_0^O < \sigma_0^S$ (for $H_0 = 0.3$ T); however, for larger H_1 (and H_0), the O signal is slightly broader than the S signal, e.g., the widths in Fig. 3.4(b) for $H_1 \sim 5 \mu\text{T}$. Finally, it is noted that $\sigma_0^O \simeq 0.13$ kHz is about 1.5 times broader than the powder average van Vleck linewidth [Eq. (1.43)] for the undistorted octahedral interstitial site in Au [dot-dashed line in Fig. 3.1(b)]. In contrast, σ_0^S is nearly 4 times broader than the powder average van Vleck linewidth for the undistorted substitutional site [dashed line in Fig. 3.1(b)]; see the Discussion.

The longitudinal spin-lattice relaxation rate T_1^{-1} was measured in both the foil and the 100 nm/MgO film at room temperature as shown in Fig. 3.6. In both, $A(t)$ following the 0.5 s beam pulse is seen to be well described by a single exponential decay [Eq. (2.9)]. The data shows no indication of mul-

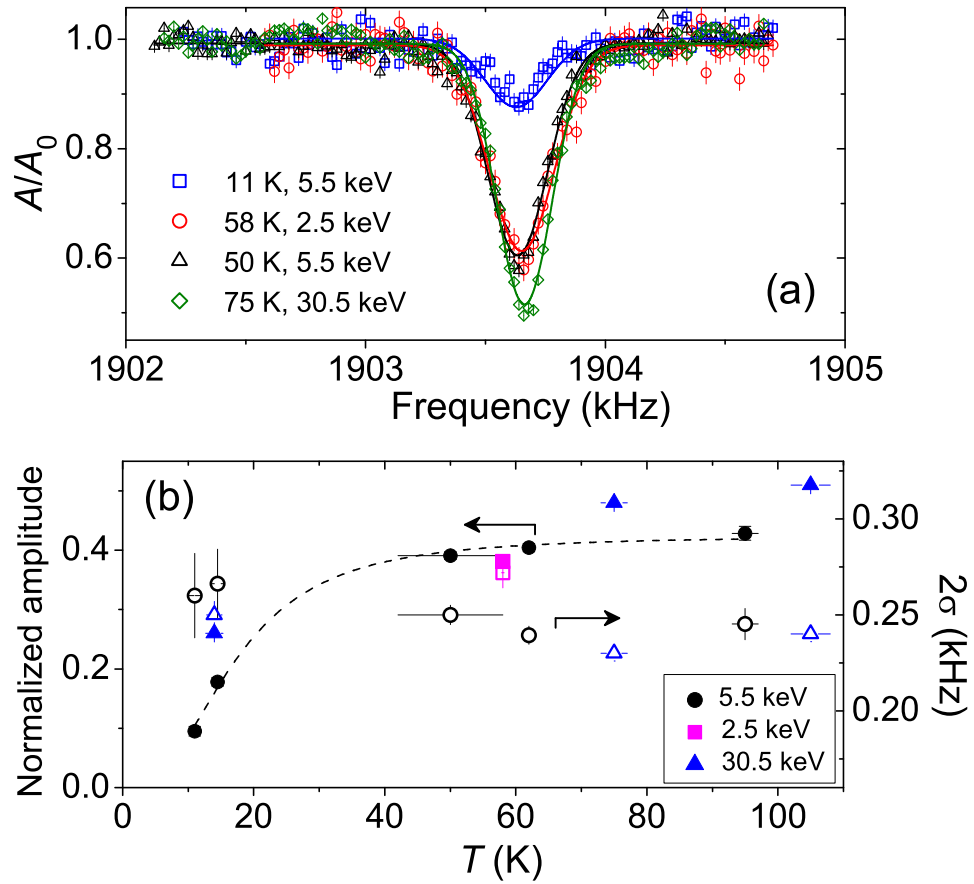


Figure 3.5: Low P_{rf} O site resonances in Au foil ($H_0 = 0.3$ T, $H_1 \sim 0.5$ μT). (a) Representative spectra and single Gaussian fits. (b) Temperature dependence of the amplitudes (filled symbols; left ordinate) and linewidths 2σ (open symbols; right ordinate). Below 50 K there is a reduction in the amplitudes as indicated by the dashed line (a guide to the eye) for the low energy data.

multiple relaxing components[213], consistent with the absence of quadrupole splitting in the spectra and the assignment of the ions to the cubic S sites. For the 100 nm film spectrum, $E_{\text{Li}} = 13$ keV, and as discussed above, the fraction of ions penetrating into the MgO substrate is negligible. However, as illustrated in Fig. 2.4(c), the relaxation rate in MgO is 2.6 times slower, so the small fraction of Li that may stop in exposed corners of the substrate are neglected (i.e., a small, non-relaxing background). The agreement between the two samples is quite good, indicating there is no sample dependence. The average of the two rates, $T_1^{-1} = 0.127(7) \text{ s}^{-1}$, is taken as the field-independent (Korringa) rate at this temperature.

3.3 Discussion

To begin, the similarities in the temperature dependence of the resonances of $^8\text{Li}^+$ in Au and Ag are noted. In both metals, at high field, two narrow resonances, positively shifted from ν_L with nearly T -independent positions, but strongly T -dependent amplitudes are observed [cf. Fig. 1.3(b)]. This is also found for ^8Li in polycrystalline Cu, but in this case the resonances are broad and not well resolved[185]. This is due to the order-of-magnitude larger γ of the two Cu isotopes giving rise to much larger dipolar linewidths; similar unresolved lines are observed for ^8Li in Al[186]. The two resonances have been provisionally assigned to ions stopping in two inequivalent cubic sites of the host lattice. Specifically, for all three metals the high temperature (smaller K) line is attributed to ions in the substitutional S site, and the low temperature (larger K) line to those in the octahedral interstitial O site. This is reasonable, simply based on the relative sizes of the three cubic sites in the fcc lattice ($S > O > T$). These assignments are motivated by analogy to results from ^{12}B cross-relaxation in Cu[179, 182]. Further, the site assignments in the group 11 metal hosts are corroborated by the recent measurements[172] and calculations[171] for ^8Li in isostructural Ni. In this picture, the T -dependent resonance amplitudes result from the thermally-activated $O \rightarrow S$ site transition, since the smaller O site is metastable and the larger S site is a lower energy configuration for the ions. In Au, the

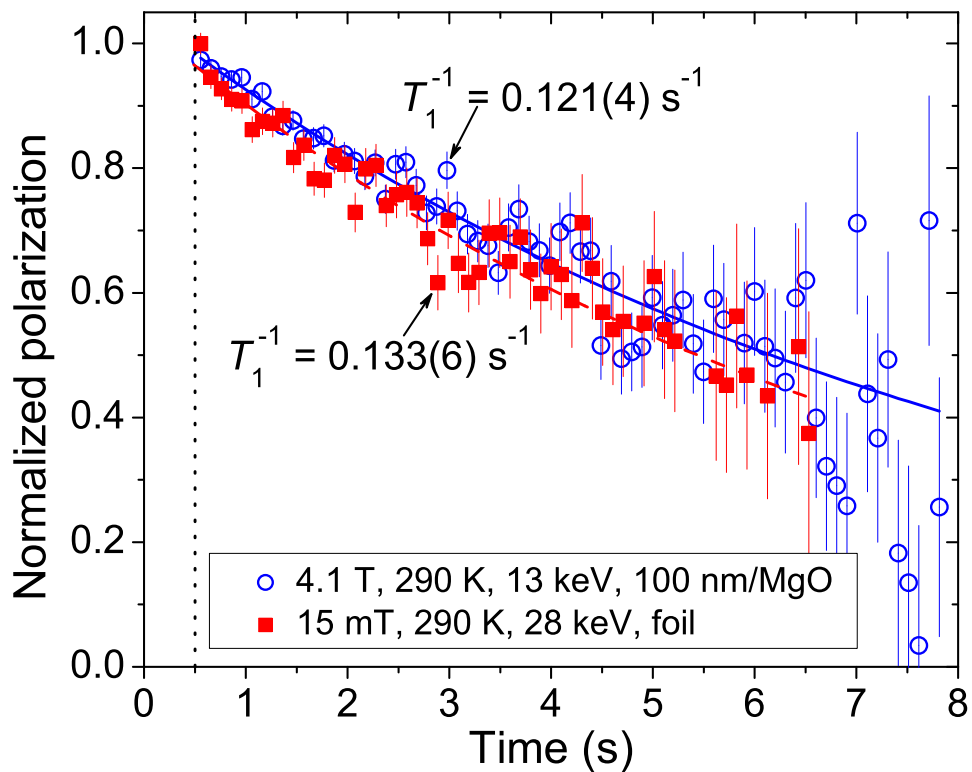


Figure 3.6: Spin-lattice relaxation spectra of ^8Li in the two Au samples at 290 K: 100 nm/MgO at 4.1 T (circles; solid line), and Au foil at 15 mT (squares; dashed line). The data are fit to a single exponential after a 0.5 s beam pulse, indicated by the dotted line. Although the magnetic field is very different, the relaxation rates are essentially the same. Reproduced from Ref. [212]. Copyright (2008) by the American Physical Society.

3.3. Discussion

ions evidently have sufficient thermal energy for this migration (within the lifetime of the Li) for T above ≈ 150 K. Recall, from the discussion in Chapter 1 that this site transition may be related to the onset of mobility of the vacancies created during the athermal implantation of the probes. Although these defects are known to become mobile typically at higher temperatures (known as stage III annealing[188]), the ion implantation process may lower the energy barrier to their mobility. Note from Fig. 3.4(b) that, for the temperatures bracketing the region of this site change, the linewidths show no indication of motional narrowing.

The dipolar linewidth is site-dependent, but uncertainty in the extent of local lattice distortion (relaxation) around the implanted ^8Li makes it difficult to use for definitive site assignments. However, such calculations are in reasonable agreement[180, 214] with the assignments for light, beta-active ions implanted in Cu. Because of the small ^{197}Au nuclear moment, small dipolar widths are expected. Indeed, it is only because they are small that such closely spaced resonances can be resolved, in contrast to the cases of Cu and Al mentioned above. The widths of the narrow ^8Li resonances in Au are larger than the dipolar (van Vleck) widths calculated for an undistorted lattice [Fig. 3.1(b)].

The origin of the additional linewidth is not clear. For example, the widths in Fig. 3.4(b) show no temperature dependence and are similar for both S and O resonances, thus they are not due to residual (ppm level) magnetic impurities in the Au, which would yield temperature- (and field-) dependent widths. The broadening likely arises from a local distortion of the Au lattice about the ^8Li as the dipolar width is dominated by the contribution from the nearest neighbours. A decrease of the distance to the nearest neighbour Au dipoles would increase the dipolar width. This possibility has been reported for other implanted probes, e.g., ^{12}B in ZnSe[177]. Alternatively, the linewidth may reflect a contribution from a narrow, unresolved quadrupolar powder pattern if the ^8Li site is not perfectly cubic. Slightly noncubic sites (with associated EFGs) could result from a small, symmetry-breaking, local lattice distortion caused by the ^8Li or, as has been suggested for ^{12}B in fcc metals[180], the EFG from close-by point defects created dur-

3.3. Discussion

ing the implantation of the probe (see Appendix B).

The finding that $\sigma_0^O < \sigma_0^S$ (at 0.3 T) is opposite to what is expected on the basis of the calculated dipolar widths in Fig. 3.1(b) of 0.095 kHz for the undistorted O sites, and 0.049 kHz for the undistorted S sites. This situation perhaps arises from opposite local host lattice relaxations surrounding the Li ions at each site, as reported for ^{12}B in Cu[179]: a local contraction about ions in S sites causing increased linewidths, and a local expansion of the lattice about ions in O sites, as σ_0^O is just slightly broader than the calculated van Vleck width, yet narrower in comparison to σ_0^S . This scenario is based on measurements at a single H_0 . At 3 T and for larger H_1 , the O resonances are slightly broader than the S resonances [Fig. 3.4(b)]. The H_1 -independent intrinsic linewidths may be H_0 -dependent and this dependence may be different for each site[176, 177]. As mentioned in the Introduction this arises because the implanted ions act as charged impurities that create EFGs sensed by the host nuclei potentially influencing their dipolar fields[176]. Thus, a detailed knowledge of σ_0 of either site awaits measurements at various external fields. For the remainder of this discussion, it will be assumed that these site assignments are correct, noting that most of the comparisons will not be drastically altered if another subset of the three cubic sites is chosen (the major difference being the coordination of the site z).

For $T < 50$ K there is a reduction in the O resonance amplitude. Preliminary data strongly suggests that this reduction is due to a small fraction of ions associated with implantation-created defects that cause a quadrupolar broadening which cannot be resolved for the amplitudes of H_1 employed for the present measurements.

The raw Knight shifts are corrected for the contribution due to demagnetization using Eq. (2.14) for $\chi_P = 1.21 \times 10^{-6}$ emu/cm³[21], yielding the corrected shifts $K_O^c = +141(4)$ ppm and $K_S^c = +73(5)$ ppm— overall small corrections. The ratio of the shifts for the two sites is then $K_O^c/K_S^c \sim 2$, corresponding to a splitting of 68(6) ppm. As χ_P for Au is T -independent, the shifts are likewise in the range of 10–290 K [Fig. 3.4(a)]. The splitting between the S and O lines observed in the polycrystalline Au foil is the same

3.3. Discussion

as that measured previously in a more highly oriented 50 nm film[211], indicating that K , and thus A_{hf} , is predominantly isotropic, as expected for a cubic host. The site-dependence of the shift is attributed to different hyperfine coupling constants as a result of hybridization of the ${}^8\text{Li}^+$ $2s$ orbital with the host s band, i.e., $2s - 6s$ hybridization. Using Eq. (1.42), $A_{\text{hf}}^S = 2.8(2)$ kG/ μ_B ($z = 12$), and $A_{\text{hf}}^O = 10.7(3)$ kG/ μ_B ($z = 6$).

These values are compared to those for ${}^8\text{Li}$ in the other simple metals in Table 3.1. For a given site, A_{hf} varies by no more than a factor of 2. The origin of the difference in A_{hf} between different hosts depends on details of the local electronic structure. As discussed in Chap. 1, A_{hf} is sensitive to several factors like the band structure of the host, the local electronic screening, and the extent of lattice relaxation around the probe. The strength of the hybridization is, in the simplest picture, a function of z and the distance between the probe and the neighbouring host atoms. Comparing the O site, z is half as big, but the distance to the nearest neighbours is less. If this were the only consideration, similar A_{hf} s for Au and Ag would be expected, on the basis that the lattice constants are essentially the same, instead the coupling constants for Au are about half the values for Ag (and χ_P for these two metals only differs by about 20%). Table 3.1 also lists the ratio $A_{\text{hf}}^O/A_{\text{hf}}^S$, which is found to be similar for all three metals, although it is slightly larger for Au than Ag and Cu, in accordance with the trend in the lattice constants ($\text{Cu} < \text{Ag} \approx \text{Au}$). First-principles calculations for a nonmagnetic defect in a nonmagnetic host, like ${}^8\text{Li}$ in these three metals, would be very useful to compare with the results of β -NMR.

At high fields, the T_1^{-1} is dominated by the Korringa mechanism. At room T , T_1^{-1} of ${}^8\text{Li}$ in Ag[184] and Cu[185] is nearly 3 times faster than in Au. The present, average room T relaxation time in Au (Fig. 3.6), $T_1 = 7.9(4)$ s, is half the 17(3) s reported by Koenig *et al.*[189], but double the 4(1) s measured by Haskell and Madansky[166]. It is within the range of the reported times, but the origin of the discrepancy is not certain, especially since previous results differ from each other by a factor of 4. In light of the sample-independence seen in Fig. 3.6, it is concluded that the present value of 7.9(4) s is the most reliable to date for ${}^8\text{Li}$ in Au. The authors of

Table 3.1: Summary of ${}^8\text{Li}^+$ K , A_{hf} , and \mathcal{K} in the group 11 metals (Cu[185], Ag[184], Au) and Al[186]. The Korringa ratios from conventional NMR[21] are given for comparison, as are the equilibrium lattice constants a_0 of the hosts[2]. Reproduced in part from Ref. [212]. Copyright (2008) by the American Physical Society.

Host	a_0 (\AA)	K^c (ppm)		A_{hf} (kG/μ_B)		$A_{\text{hf}}^O/A_{\text{hf}}^S$	S site	\mathcal{K} host NMR
		S	O	S	O			
Cu	3.61	+136(3)	+197(3)	4.8(1)	13.8(2)	2.9(1)	1.46(4)	1.9
Ag	4.09	+128(13)	+220(16)	6.2(6)	21(2)	3.4(5)	1.1(3) ^a	2.0
Au	4.08	+73(5)	+141(4)	2.8(2)	10.7(3)	3.8(3)	1.01(6)	1.4
Al	4.05	+107(3)	+141(4)	1.66(5)	4.4(1)	2.7(1)	1.19(5)	1.2

^aRef. [187].

3.3. Discussion

Ref. [189] note that in both of the previous studies (using MeV recoil ions) the temperature of the Au samples was not controlled during irradiation; however, they conclude that contamination of the sample surface was the most likely reason for the faster 4(1) s relaxation time reported in the earliest study. A relaxation time of 3.3(3) s is also reported in Ref. [189] for ^8Li in Ag foil at room T , which agrees very well with measurements using the TRIUMF β -NMR spectrometer for ^8Li in a Ag film.[184]. Determination of relaxation times that are significantly longer than the probe lifetime τ is difficult. The present measurement using $^8\text{Li}^+$ polarized in two helicities accurately determines the baseline corresponding to the thermal equilibrium polarization, even though the relaxation is too slow to reach this value during the experiment.

The average T_1^{-1} value can be combined with K_S^c in Eq. (1.26) to yield $\mathcal{K} = 1.01(6)$ for ^8Li in Au at 290 K. This result is remarkably close to the ideal value of 1, and as will be shown in the following chapters, very different from that measured in a strongly enhanced metal like Pd. The \mathcal{K} values for the simple metal hosts are given in Table 3.1. They all reveal reductions in enhancement for ^8Li in comparison to the host nuclei (conducted at cryogenic temperatures to improve signal-to-noise). The “disenhancement” is largest for Ag. The \mathcal{K}_{Au} is slightly larger (or similar to¹¹) that for the ^8Li probe. Ions in S sites should have approximately the same spatial Fourier transform $A_{\text{hf}}(\mathbf{q})$ as the host nuclei. It can be concluded that the presence of the $^8\text{Li}^+$ does not strongly influence \mathcal{K} , e.g., via electron scattering. A study comparing \mathcal{K} measured for ^{12}B in the group 11 metals (assigned to O sites) with that of the host nuclei found near equal values for Cu and Ag, but a larger enhancement for Au[173]. The possibility was suggested that this “Au anomaly” was specific to that probe[173]. The lack of enhancement for ^8Li in Au supports that proposal.

¹¹Preliminary results from T_1^{-1} measurements in Au foil as a function of temperature at 15 mT suggest $\mathcal{K}_S \sim 1.2$, and $\mathcal{K}_O \sim 1.4$.

3.4 Conclusions

To summarize the β -NMR has been used to study the behaviour of low energy ${}^8\text{Li}^+$ implanted in bulk Au. Two narrow resonances corresponding to two cubic stopping sites are found. These are assigned to ${}^8\text{Li}$ ions in the octahedral interstitial O , and substitutional S sites. As expected for a simple metal, the Knight shifts for ions in these sites are independent of temperature, as are the resonance linewidths. A transition from the metastable O site to the S site is observed centred at about 190 K. Values for the intrinsic linewidths of the two resonances are also reported, with both being broader than the van Vleck width for the undistorted sites, with the additional width being greater for the S site. No evidence for a depth dependence to these narrow resonances is found for implantation depths in the range of 10–95 nm. The spectra in Au are very similar to those in Ag, but with smaller shifts, and a considerably slower spin-lattice relaxation rate for the S site. The Korringa ratio for S site ions in Au is not significantly enhanced above the free electron gas value of one, and is also not very different from the value obtained from Au NMR. \mathcal{K} for substitutional ${}^8\text{Li}$ in the other simple metals also shows no significant enhancement over the respective host values; instead, there is a disenancement in Cu and in Ag that is greater than in Au.

The T_1^{-1} is found to be highly field-independent for external fields greater than at least 15 mT at 290 K.

Overall, the data show that ${}^8\text{Li}$ probes the intrinsic electronic structure of Au, and the behaviour of the probe in this host is quite similar to that in the other simple metals. The results of ${}^8\text{Li}$ β -NMR of Au are straightforwardly interpreted making this metal an excellent candidate for future β -NMR studies of, e.g., magnetic multilayer heterostructures.

Chapter 4

^8Li β -NMR of Palladium Foil

4.1 Introduction

In the previous Chapter, the results from ^8Li β -NMR of bulk Au were presented. The behavior of the $^8\text{Li}^+$ in Au (i.e., K^c , A_{hf} , \mathcal{K}) is found to be very similar to that of $^8\text{Li}^+$ in Ag, Cu, and Al (Table 3.1). The results obtained from these three metals serve as excellent systems with which to contrast the behavior of $^8\text{Li}^+$ in Pd. As discussed in Chapter 1, the magnetic properties of Pd are unique and quite distinct from those of the group 11 metals. In this brief chapter, this is indeed illustrated by the results of ^8Li β -NMR in Pd foil.

4.2 Results and discussion

A piece of 12.5 μm -thick, 99.95% Pd foil was mounted around a single crystal of (100) oriented MgO. The foil is highly polycrystalline as confirmed by X-ray diffraction. As the foil is far too thick for the ion beam to penetrate, a small pin was used to pierce the foil creating a hole that exposed the MgO backing. Using the electrostatic steering elements, the beam was focussed onto this hole allowing for the simultaneous collection of a signal from both materials for $H_0 = 4.1$ T at an implantation energy ~ 30 keV (Fig. 4.1). Steering the beam away from the hole resulted in a single resonance from the just the foil, as the mean implantation range is ~ 100 nm. This permitted the assignment of the resonance from ^8Li stopping in the Pd in the composite spectra; Fig. 4.1.

The assignments are consistent with the expectation that the resonance from ions stopping in the MgO backing should be near the Larmor frequency

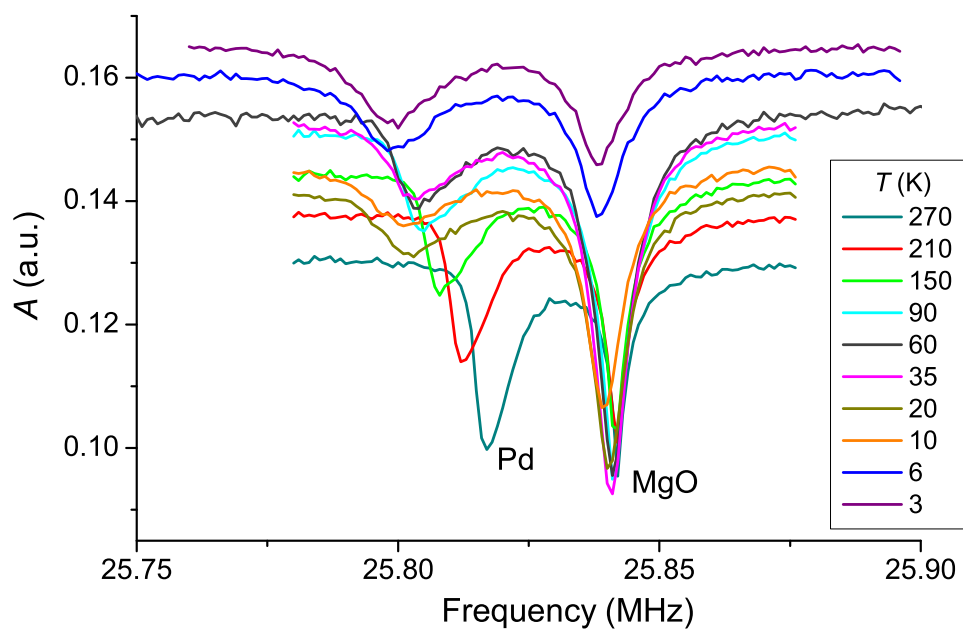


Figure 4.1: Temperature dependence of the ^8Li β -NMR spectrum at 4.1 T ($H_1 \sim 40 \mu\text{T}$) in Pd foil wrapped around crystalline MgO. The spectra have not been offset; the change in baseline asymmetries is due to the increase in spin-lattice relaxation with increasing temperature. Reproduced in part from Ref. [215]. Copyright (2005) by Elsevier B.V.

($\nu_L = 25.836$ MHz at 4.1 T). It is immediately apparent that the shift of the Pd signal is quite large (compared to the simple metals), negative, and T -dependent. The spectra are also quite broad and thus required a relatively large H_1 in order to obtain a signal of reasonable amplitude. The spectra shown in Fig. 4.1 are not offset; the decreasing off-resonance, baseline asymmetry A_0 as T is increased is consistent with the linear increase of T_1^{-1} with increasing T in metals (Chapter 1). Scanning a larger frequency range at 270 K revealed no additional resonances, indicating that the spectrum is not quadrupolar and that the stopping site(s) is(are) cubic.

The Pd spectra broaden considerably as the sample is cooled. As T is lowered the line becomes more asymmetric, appearing as a main resonance with a small amplitude, high frequency shoulder. This change in lineshape may be due to multiple low- T stopping sites with similar resonance frequencies. The Pd signal is described by two overlapping Gaussians (it will be seen in the following Chapter that the use of two lines for the Pd signal is indeed appropriate). The choice of Gaussian instead of Lorentzian lineshapes is empirical; however, regardless of the lineshape used, an additional Lorentzian needed to be included to account for the small amplitude, broad component centred between the Pd and MgO signals. A single Lorentzian is used to describe the MgO signal. Examples of these fits are shown in Fig. 4.2(a).

Using Eq. (1.16) with the MgO resonance frequency as ν_0 , the raw $K(T)$ obtained for the two Pd lines are shown in Fig. 4.2(b). As a convention in this thesis, the more negatively shifted line is denoted as 1 . The K values for both lines show a similar trend with T , spanning a range of ≈ 800 ppm. The resonance frequencies scale with H_0 , as expected for Knight shifts, further ruling out a quadrupolar origin of the splitting. For instance, at 270 K and $H_0 = 2.2$ T, fitting the Pd signal to a single lineshape yields $K \approx -994(14)$ ppm, consistent with the values observed at 4.1 T. Although these two lines are reminiscent of the tentatively assigned O and S resonances in the group 11 metals, there are differences in the case of Pd; this is discussed further in the next Chapter.

It is possible that the proximal field from the foil is influencing the res-

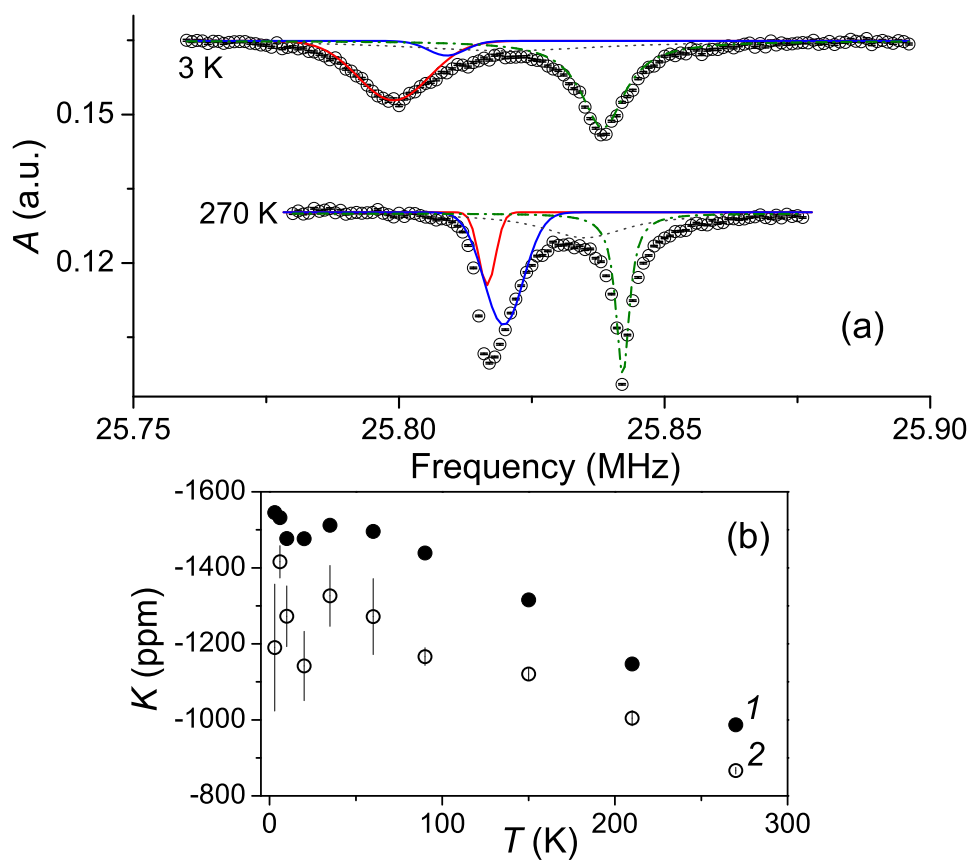


Figure 4.2: (a) Representative fits; the Pd signal is fit using using two overlapping Gaussian lineshapes (solid lines), a single Lorentzian lineshape is used to fit the MgO signal (dash-dot line), and an additional Lorentzian lineshape is added to account for the broad background (dotted line). (b) The resulting K as a function of T for the two Pd lines.

onance frequency in the MgO, increasing ν_0 , thereby artificially increasing the values of K . This can be ruled out by a simple estimation of the magnitude of the proximal field just outside the foil. By treating the foil as a thin, uniformly magnetized slab of aspect ratio $\xi_{\text{film}} = 10^{-3}$ (see Sec. 2.5.2), the proximal field is found[191] to be $\sim 0.1 \mu\text{T}$ throughout the T range studied— a value too small to affect the resonance in the MgO.

The K values obtained are corrected for the demagnetization using Eq. (2.14), treating the foil as a thin slab. In this case, there are two choices for the values of $\chi_{\text{Pd}}^v(T)$: (i) the literature susceptibility of Pd χ_{lit} (see Fig. 1.2), and (ii) the susceptibility obtained from SQUID measurements of the foil itself χ_{squid} ; shown in the inset of Fig. 4.3. The corrections are applied to the shift of line 1 as its position is better determined from the fits. In the main panel of Fig. 4.3, K_1^c is plotted versus the corresponding $\chi(T)$. Fig. 1.2 shows that from the conventional NMR of ^{105}Pd , the Knight shift tracks the bulk susceptibility. In contrast, the relation between the ^8Li $K^c(T)$ and the corresponding $\chi(T)$ is only linear in the region corresponding to high T ; K^c fails to track χ_{lit} for $T < 90$ K, and χ_{squid} for $T < 60$ K. Best-fit lines to the linear portions are shown in Fig. 4.3 along with the corresponding equations relating K^c [unitless] to the respective χ [emu/mol].

Above about 50 K, χ_{squid} is within 10% of χ_{lit} ; however, as can be seen from the inset of Fig. 4.3, below this T the magnetization M of this foil increases, whereas the literature magnetization of pure Pd decreases. This increase is attributed to dilute, magnetic impurities. It is well known that such impurities give rise to a Curie-like $1/T$ upturn of the magnetization at low T (they may have been introduced during the processing of this foil). In comparing the magnitude of the upturn in M with similar observations in Pd (e.g., Refs. [84, 153]), the concentration of impurities is estimated to be ~ 100 ppm. This explains why the low- T deviations of K^c in Fig. 4.3 are in opposite directions. Regardless, the nonlinearity is obtained regardless of the choice of χ , indicating that the *local* susceptibility probed by the implanted Li ions is distinct from that of either pure Pd, or that of this particular foil.

A_{hf} can be calculated using Eq. (1.42), equating the term K^c/χ with

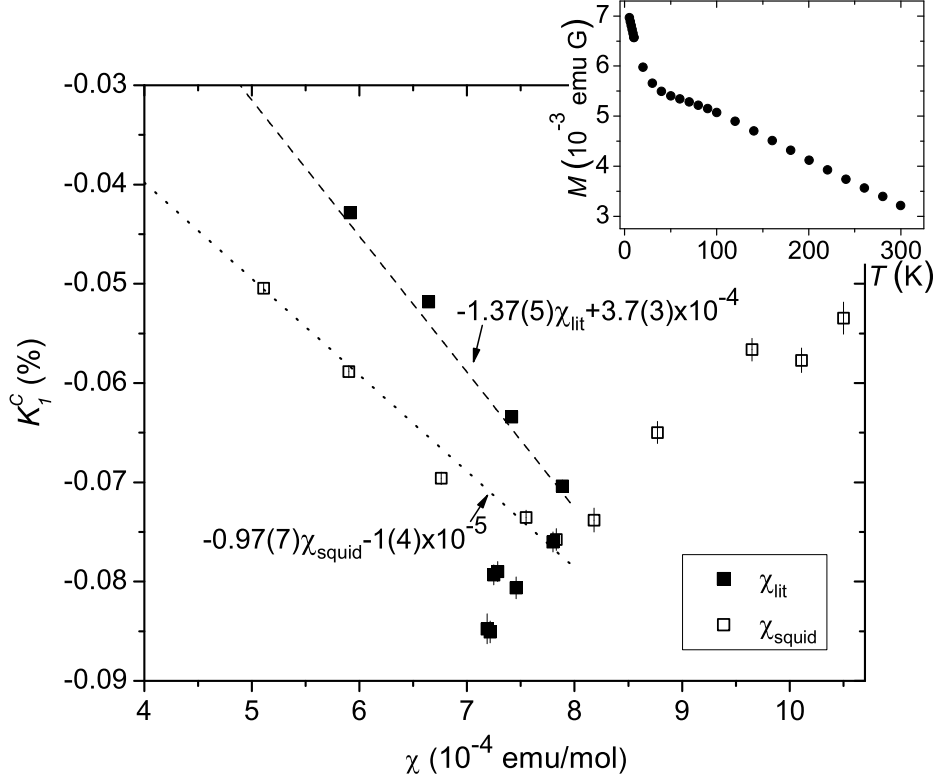


Figure 4.3: Demagnetization-corrected shifts K^c of line 1 versus χ_{Pd} . Temperature is implicit, and *decreases* from left to right. The shifts were corrected for using, and subsequently plotted against, either the literature bulk susceptibility χ_{lit} , or the susceptibility of the same β -NMR foil sample χ_{squid} . The latter was obtained from the magnetization measured in a SQUID at 4.1 T (inset). In the high T region, $K^c(T)$ is linear with the respective $\chi(T)$ as shown by the best-fit lines.

4.2. Results and discussion

the slopes from the linear fits in Fig. 4.3, and assuming only octahedral interstitial stopping sites ($z = 6$). The result is $-1.28(5)$ kG/ μ_B using χ_{lit} , and $-0.90(7)$ kG/ μ_B using χ_{squid} .

The linewidths and amplitudes of the Gaussians used to fit the Pd signals are shown in Fig. 4.4. Focussing first on the widths [panel (a)], both lines are relatively broad, and broaden further upon cooling. The sharp increase in width occurs for both lines when T is less than about 50 K. This is the T range where χ_{squid} begins to deviate from χ_{lit} , likely due to dilute magnetic impurities. These impurity moments are probably randomly distributed throughout the foil, as are the final stopping sites of the Li ions. As a consequence, when averaged over all distances, the impurity magnetization gives rise to an inhomogeneous broadening, but does not affect the resonance frequency, as mentioned in Sec. 1.2.1. Indeed, the increase in linewidth as $T \rightarrow 0$ is of the same order of magnitude as that calculated for dipolar broadening following Ref. [37] by assuming 100 ppm of Fe impurities with effective moments of $14\mu_B$ [153]. Such an impurity concentration is consistent with the quoted purity of this foil.

The corresponding amplitudes [panel (b)] decrease nearly linearly with T . However, below 50 K where the Curie-like increase in the widths occurs, there is scatter and the behaviour of the amplitudes is less obvious. This is particularly the case for line 2, which shows a larger reduction in amplitude than that expected compared to its equality with line 1 above 50 K. For a constant H_1 , a broader line will have a smaller amplitude. The significant broadening of such small signals increases the uncertainty in the amplitudes, but inspection of Fig. 4.2(a) shows that at low T , the broad component overlaps line 2. As temperature decreases, the widths increase and amplitudes decrease, and it becomes less appropriate to treat the broad component and line 2 separately. This likely leads to the peculiar behaviour of the amplitude of line 2 and increasing the uncertainties in its K at low T [Fig. 4.2(b)]. The inclusion of the broad component partly accounts for the Pd lines not being described by pure Gaussians, and is attributed to the magnetic impurities producing a pseudo-Lorentzian lineshape, i.e., increasing the spectral weight in the “tails” of the Gaussians[37]. Nonetheless, the

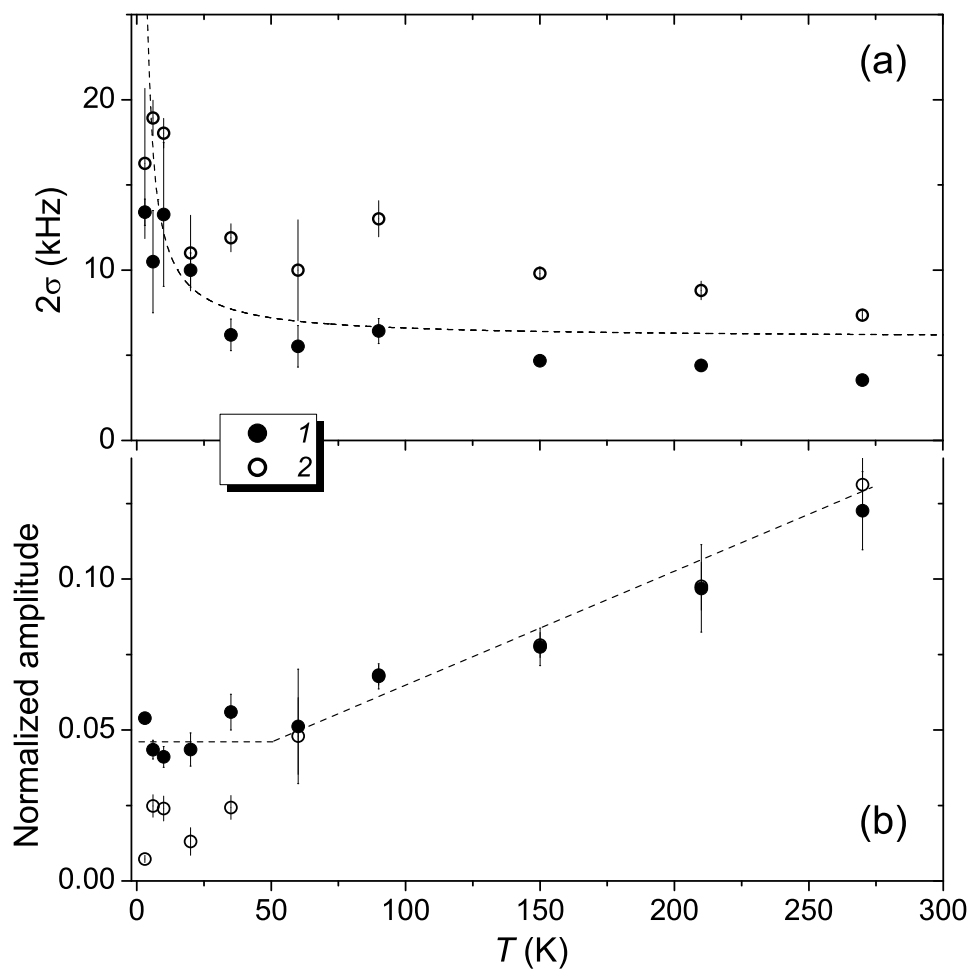


Figure 4.4: (a) Widths of the two Gaussians used in fitting the Pd signal as a function of temperature. The dashed line is an inverse- T function given by $(60/T) + 6$, and is shown for comparison. (b) Normalized amplitudes of the two Pd lines with temperature; the dashed line is a guide to the eye.

present analysis is retained, particularly since the discussion of K is confined to line 1, which has little overlap with the broad component. Moreover, in light of the presence of dilute magnetic impurities, the present analysis is quite satisfactory for an initial overview of the behaviour of ^8Li in Pd.

Finally, the Korringa relation [Eq. (1.26)] can be applied to the above results. Using the ambient temperature relaxation rate measured previously[189] (0.33 s^{-1}), and taking $\mathcal{K} = 1$ at 270 K, $|K^c|$ is predicted to be ~ 120 ppm, only about a quarter of what is observed. Similarly, for $K^c = -428.5$ ppm predicts a $T_1 \sim 0.2$ s, an order of magnitude faster than actually observed. Combining this K^c with the relaxation rate gives $\mathcal{K} \sim 13$, about 1.5 times that measured for the host nuclei by conventional NMR[21] at 4 K ($\mathcal{K}_{\text{Pd}} = 9.4$). Thus, even the smallest shift for ^8Li in Pd is much larger than expected from the Korringa relation; not surprising given that Pd is far from being a simple metal.

4.3 Conclusions

In this short Chapter the general features of ^8Li β -NMR in (bulk) Pd foil were presented. In contrast to the shifts observed in noble metals or Al, strongly T -dependent Knight shifts are observed in Pd, that are much larger than the T_1^{-1} predicts. The resonance is relatively broad, and exhibits a strong T -dependent width. At high temperature the shifts scale with susceptibility of pure Pd, but at low temperature this scaling no longer holds, and is most likely a manifestation of the unique magnetic properties of this host in response to the presence of the probe itself.

In order to verify that these intriguing results are truly intrinsic to $^8\text{Li}^+$ in bulk Pd, the β -NMR of $^8\text{Li}^+$ in a 100 nm film grown from a higher purity Pd source was subsequently studied, and this is the topic of the following Chapter.

Chapter 5

β -NMR of ^8Li in a Bulk Palladium Film

5.1 Introduction

In the previous Chapter, a brief study of the ^8Li in a microns-thick Pd foil sample revealed an unexpected low-temperature behaviour of the Knight shift that is likely linked to the unique magnetic properties of Pd. In order to verify that these results are indeed intrinsic to $^8\text{Li}^+$ in bulk Pd, a 100 nm film of Pd was studied. By comparison to the findings in Au (Chapter 3), it is expected that a film of such thickness should give β -NMR results similar to that of the 12.5 μm foil. Additionally, at low temperatures, the magnetization of the foil indicated the presence of magnetic impurities that broadened the linewidths of the resonances in that sample. This was avoided for this film as it was grown from a higher purity source, and subsequently protected by a Au capping layer.

Resonances are presented from this film, and the spin-lattice relaxation rate is measured as a function of temperature in the foil. A combined analysis of the two data sets is presented in order to gain a more detailed understanding of the β -NMR of $^8\text{Li}^+$ in bulk Pd. This is an important prerequisite to follow-up experiments to examine the possibility of studying size-dependent magnetic properties of thin Pd films by β -NMR.

5.2 Results

The sample consists of a nominally 100 nm thick Pd film grown via e-beam evaporation from a 99.99% source onto an epitaxially polished (100) STO

substrate at 60–80 °C. The growth rate was $\sim 0.5 \text{ \AA/s}$ under a background pressure of $\sim 10^{-8}$ Torr. It was subsequently capped *in situ* with nominally 10 nm of Au. The thicknesses being established by a quartz crystal growth-rate monitor. The Pd is found to be polycrystalline, but with a (111) texture along the film normal as determined from X-ray diffraction (thus less polycrystalline than the foil).

Resonances were recorded at an external field of 4.1 T for an implantation energy of 11 keV and $H_1 \sim 30 \mu\text{T}$. For this E_{Li} the TRIM.SP simulation of the stopping profile indicates that no ions should stop in the STO substrate [cf. Figs. B.2(b) and B.3]. Spectra were collected in the temperature range of 8.5 K–270 K and are displayed in Fig. 5.1(a). The signals from Li in the two layers could be assigned based on their relative amplitudes, and the expected K in the respective metals (Chapters 3 and 4). The assignments were confirmed by recording a spectrum for $E_{\text{Li}} = 0.9 \text{ keV}$ for which the signal assigned to ions in the Au is of larger amplitude compared to that assigned to ions stopping in the Pd.

As expected from the measurements in the 12.5 μm foil presented in the previous Chapter, the Pd signal is strongly T -dependent with a large, negative K . The amplitude of the Pd signal also decreases with decreasing T , as observed in the foil. As seen in the data of Chapter 3, the position of the resonance from ions in the Au does not change with T , nor does its amplitude. This is best seen in the normalized spectra in the inset of Fig. 5.1(b). It is noted that the Au signal is quite broad; however, this is not discussed here, keeping the focus on exclusively the Pd resonances.

The Pd resonances from this film clearly appear as two partly resolved lines throughout the entire T range studied. This *a posteriori* justifies the use of two signals in fitting the resonances in the Pd foil in Chapter 4. As discussed further below, in contrast to the foil spectra, there is no Curie-like broadening of the resonances at low T , consistent with the higher purity of this sample. The spectra were thus fit using two Lorentzian lineshapes to account for the Pd signal, and a single Lorentzian lineshape for the Au signal. This is illustrated for three representative spectra in Fig. 5.2. Close inspection of these spectra shows that the choice of Lorentzians is motivated

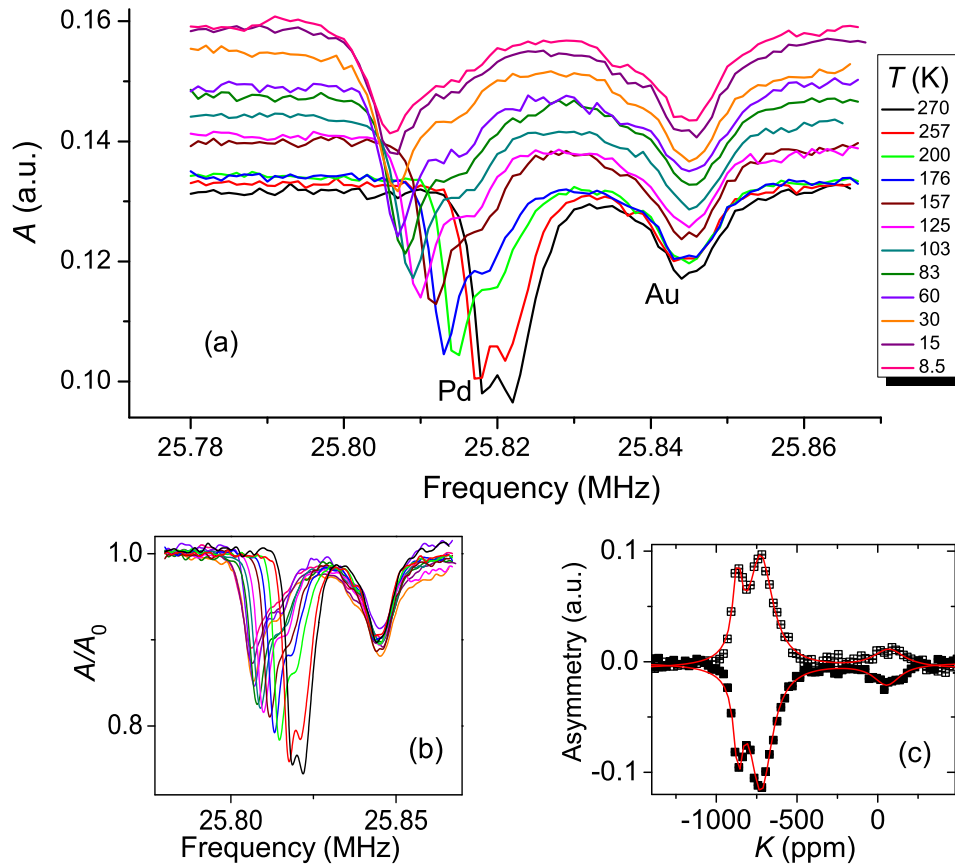


Figure 5.1: (a) Temperature dependence of the ^8Li β -NMR spectra recorded in the Au(10 nm)/Pd(100 nm)/STO film at 4.1 T for $H_1 \sim 30 \mu\text{T}$ and $E_{\text{Li}} = 11 \text{ keV}$. The amplitude of the Pd signal decreases with decreasing T while the amplitude of the Au signal remains constant, as seen in (b) for the normalized spectra. (c) Spectrum from this film ($H_0 = 6.55 \text{ T}$, $H_1 \sim 40 \mu\text{T}$, 270 K) in the separate helicity channels.

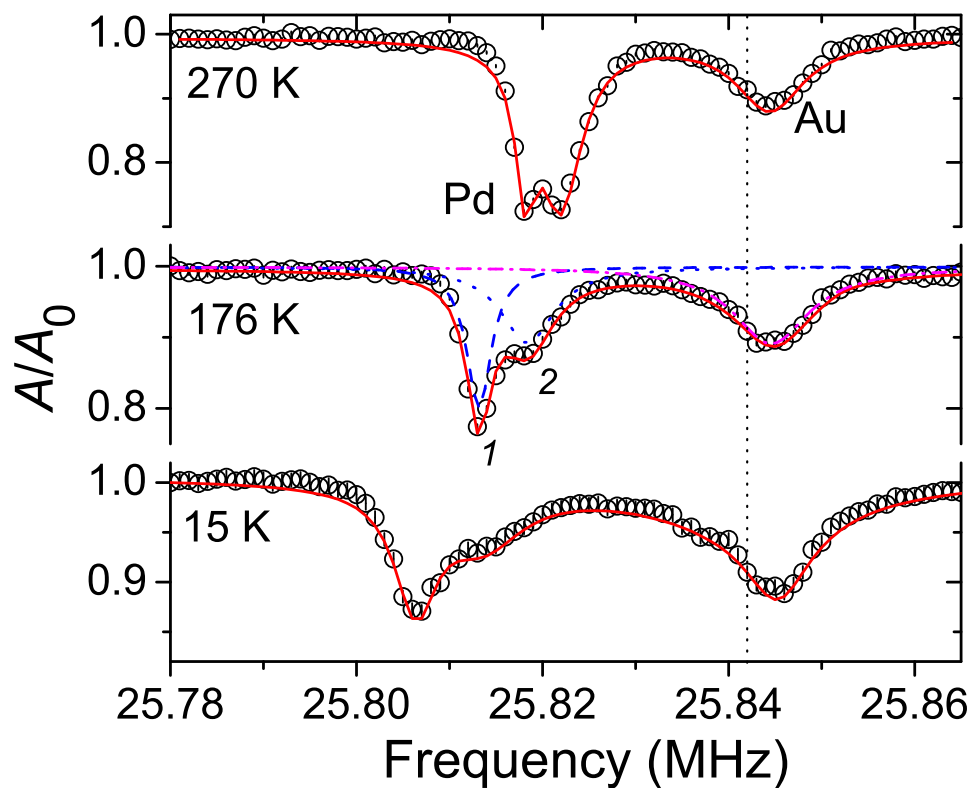


Figure 5.2: Representative spectra from Fig. 5.1 showing the fits to three Lorentzians. The Pd signal is fit to two overlapping lines, denoted 1 and 2, and the Au signal is fit to a single line. The vertical line denotes ν_0 as determined from the known K_S in Au (Chapter 3). Reproduced from Ref. [216]. Copyright (2007) by the American Physical Society.

by the high rf power, but also to account for the small, high frequency tail of the Pd signal. This is analogous to the high frequency broad component observed in the foil spectra, but in the present resonances it is of reduced amplitude and no additional lineshape was needed in the fits. It is noted that in comparison, the low frequency end of the signal exhibits a sharper cut-off. Random, dilute magnetic impurities are expected to produce symmetrically broadened resonances[37]. The asymmetric shape of these signals instead suggests the shifts are distributed towards smaller values. As the temperature is decreased, the frequency difference (i.e., splitting) between the two lines comprising the resonances remains essentially constant.

Based on the results in Chap. 3, for $T > 150$ K, the Au signal would be expected to appear as two resolved resonances attributed to ions stopping in the S and O sites. However, as stated above, the resonance from the Au is broad, and the two lines are not resolved. Additionally, near room temperature the resonance from the Au is predominantly from ions assigned to the S site. Using the established value of K for this site (+63 ppm) and the frequency of the Au signal in this film at 270 K, a value of the reference frequency ν_0 was determined (vertical line in Fig. 5.2).

With the value of ν_0 fixed, raw K values for the two Pd lines were calculated using Eq. (1.16) and are shown in Fig. 5.3(a). The spectra show no indication of a quadrupolar interaction in the individual helicities, e.g., Fig. 5.1(c). The K values of both Pd lines for $H_0 = 6.55$ T at 270 K [e.g., Fig. 5.1(c)] and 70 K are essentially equal to the shift values at 4.1 T, consistent with magnetic Knight shifts, as was concluded from the foil resonances. The values of K for the two lines in the foil are also plotted in panel (a) of Fig. 5.3. The similarity between the shifts from the two samples is immediately evident; the magnitude of the shifts and their variation with T are consistent between the two samples.

As the splitting between lines 1 and 2 in the film is small in comparison to the shifts (~ 200 ppm) and does not show any appreciable dependence on T ; taking the average shift K_{av} simplifies the analysis, and this is plotted Fig. 5.3(b). For the sake of comparison, K_{av} of the two lines from the foil is also shown in Fig. 5.3(b). The magnitude and temperature dependence

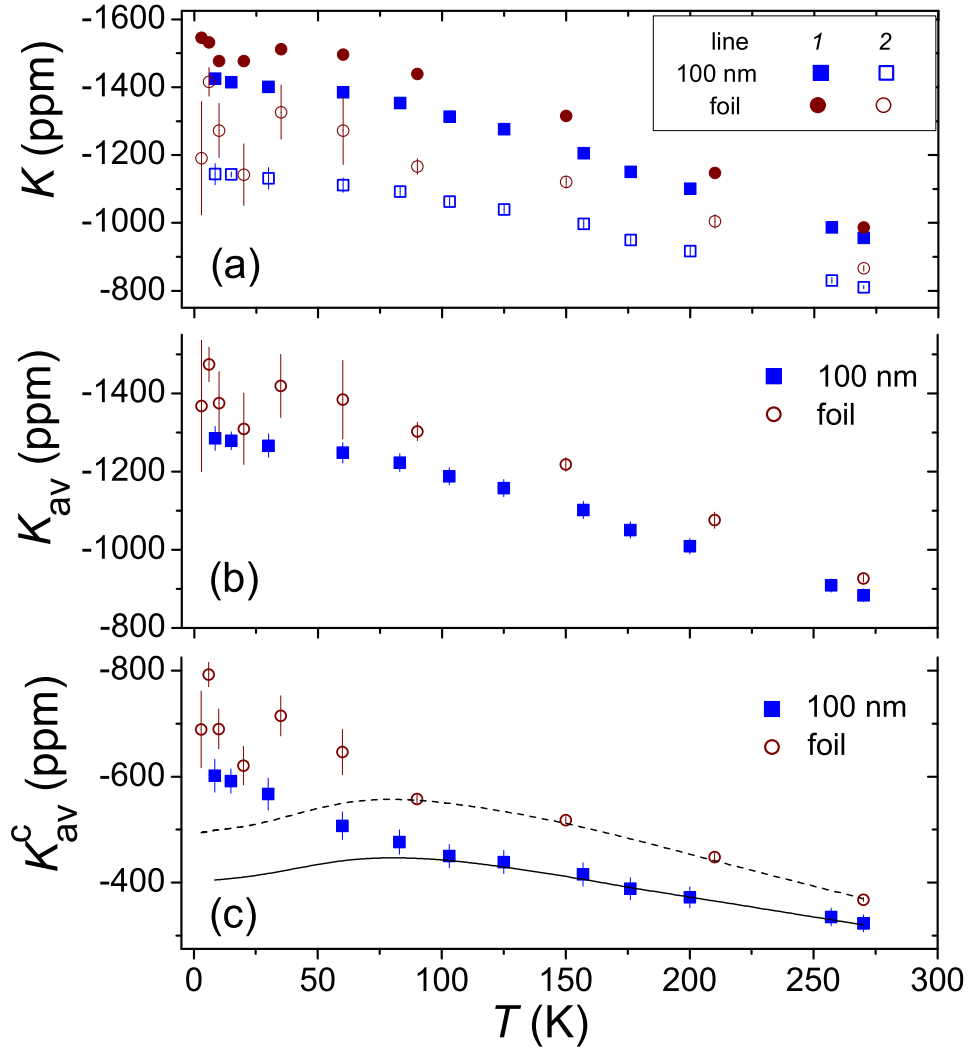


Figure 5.3: ^8Li Knight shifts measured in the 100 nm film and Pd foil (Chapter 4) and as a function of temperature. (a) Raw shifts of the two lines used to fit the Pd signals from both samples, and (b) the average of the shift of the two lines in (a). (c) Average shifts from (b) corrected for the demagnetization using the literature χ_{Pd} . The lines indicate the shift values if K_{av}^c scaled with the susceptibility of Pd for all T (cf. Fig. 5.4).

5.2. Results

of the two $K_{\text{av}}(T)$ are very similar as the values for the 100 nm are at most about 10% smaller than those for the foil. This is most significant below 60 K where, due to the broadening attributed to dilute magnetic impurities, the uncertainties and scatter in the shifts in the foil, especially of line 2, are the largest. Overall, the agreement in the shifts from the two samples can be considered quantitative. The small discrepancy is largely attributed to systematics, particularly the broadening in the foil producing unresolved lines, and the indirect determination of ν_0 for the film data.

The K_{av} values are subsequently corrected for the effect of demagnetization using Eq. (2.14). The choice of χ is clearly important here. In contrast to a sample of foil, it is not feasible to measure the magnetization of this thin film using SQUID magnetometry as the magnetization would be dominated by the signal from the massive STO substrate. The susceptibility obtained from the magnetization of the lower purity foil (inset of Fig. 4.3) is obviously not appropriate. As the raw shifts are very similar in this film to those in the bulk foil, the literature susceptibility of pure Pd χ_{Pd} (Fig. 1.2) is used in Eq. (2.14). The resulting corrected values are plotted in panel (c) of Fig. 5.3, where K_{av}^c from the foil is also shown for comparison.

The corrected shifts from the film exhibit a monotonic increase toward larger negative values upon cooling. At the lowest T K_{av}^c has increased by a factor ~ 2 over the value near room T . The low temperature susceptibility probed by the Li ions is not proportional to χ_{Pd} , while at higher temperatures it scales linearly with χ_{Pd} . This behaviour is seen in both the foil and the film, and thus, is intrinsic to $^8\text{Li}^+$ in Pd. Focussing on the film, below about 110 K, K_{av}^c increases roughly linearly with decreasing T . At the lowest T , K_{av}^c is about -200 ppm larger than if the scaling with χ_{Pd} were maintained, which is well outside the statistical errors. This low- T deviation is not entirely surprising as χ_{Pd} is very sensitive to the presence of structural perturbations (like the ^8Li probes), particularly for T in the region of the susceptibility maximum and below. Thus, it seems reasonable that for $T < T^* \simeq 110$ K a low temperature “defect” state is formed for $^8\text{Li}^+$ in Pd. In this T range, the local susceptibility sensed by the Li χ_{loc} differs from that of χ_{Pd} — it is notably *enhanced* over that of the pure host.

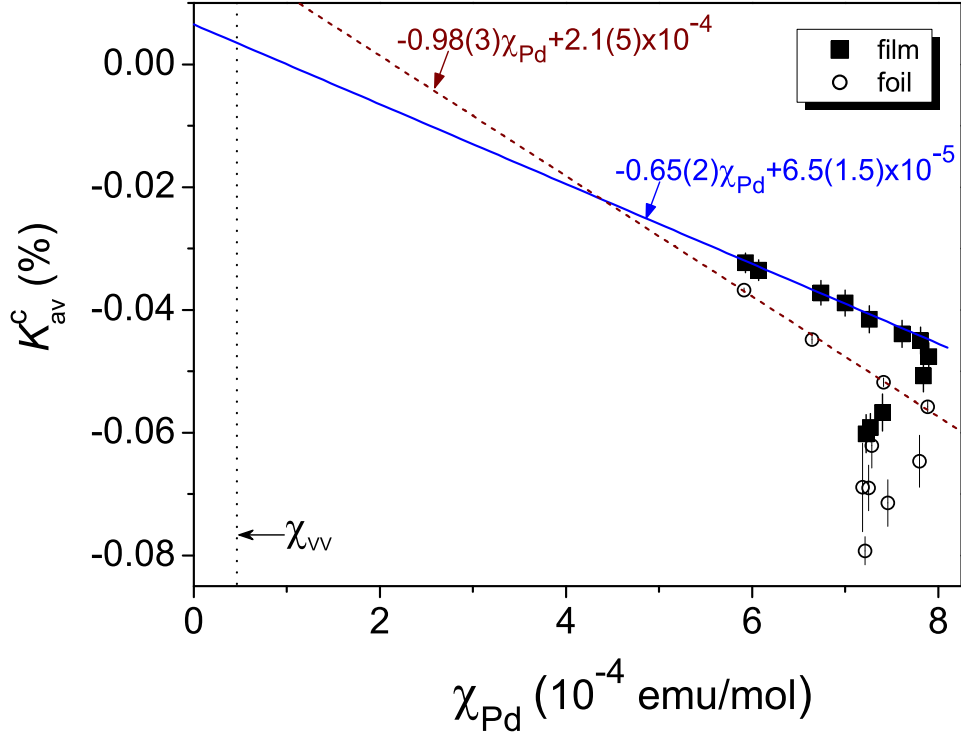


Figure 5.4: Demagnetization-corrected average shifts for ${}^8\text{Li}^+$ in the film and foil versus the susceptibility of Pd. At high temperature (small χ_{Pd}), K_{av}^c is linear with the susceptibility as illustrated by the best-fit lines. The vertical line denotes the van Vleck (orbital) susceptibility of Pd[11].

Above T^* the scaling of K_{av}^c (and thus χ_{loc}) with χ_{Pd} is shown by the K - χ plot of Fig. 5.4. Best-fit lines for the shifts in the high T region are shown along with the associated expressions for K_{av}^c [unitless] as a function of χ_{Pd} [emu/mol]. Having established that the magnitudes and thermal evolution of the shifts in the film are consistent with those from the foil, for the remainder of this Chapter, the analysis will be restricted to the Knight shift data from the film.

Extrapolation of the fit line in Fig. 5.4 toward $\chi = 0$, i.e., for vanishing d spin polarization, can be used to estimate the T -independent contributions to the shift of the implanted ${}^8\text{Li}$. These would be the orbital (or chemical) shift and the shift due to the paramagnetism of the s electrons. The

latter would be obtained by extrapolation to χ_s , but may not be strictly T -independent due to the $s - d$ hybridization in the host[93]. For Pd, estimates of χ_s are either smaller, or similar to χ_{VV} , which amounts to just a few percent of the total susceptibility[5, 14]. From Fig. 5.4, the intercept of the fit line can thus be used as an adequate approximation for these contributions, yielding $\sim +65$ ppm. This value is derived from a limited number of data points. The large extrapolation required for this data increases the uncertainty considerably to $\sim \pm 100$ ppm (as determined manually). In Sec. 1.4 it was mentioned that the chemical shifts of Li from $^{6,7}\text{Li}$ NMR generally span a very small range ($\sim \pm 10$ ppm). Thus, a small K^{orb} is expected for ^8Li . The μ^+ shift in Pd for zero susceptibility is $+45(10)$ ppm[198]. To obtain Knight shifts arising only from the coupling to the d electrons, a T -independent contribution should be subtracted from K_{av}^c . However, as this appears consistent with a small value, and the uncertainty in such a value is substantial, no attempt is made here to correct the ^8Li Knight shifts for this contribution.

From the slope of the fit line in Fig. 5.4 a value of the hyperfine coupling constant A_{hf} for ^8Li in the film can be calculated from Eq. (1.42). Although not strictly necessary, a value needs to be assigned to z . This requires a consideration of the possible stopping sites for Li in Pd. It is assumed that the ions occupy exclusively the octahedral interstitial site ($z = 6$); discussed further below. This yields $A_{\text{hf}} = -0.65(2)$ kG/ μ_B . By contrast, the coupling constants of ^8Li in the group 11 metals (Table 3.1) are at least an order of magnitude larger. This is not unreasonable, as the Li is hybridized with the d band in Pd and these orbitals are more contracted and closer to the host atoms, the overlap is smaller in this host. Due to the enhanced susceptibility of Pd, a small coupling is still sufficient to produce the sizeable shifts observed.

The amplitudes of the Lorentzians used to fit the Pd signal in the film are shown in Fig. 5.5(a). Both lines exhibit a monotonic decrease in amplitude with decreasing T . This is the same trend observed for the amplitudes in the foil [cf. Fig. 4.4(b)] Indeed, the decrease as the film is cooled is quantitatively similar in both samples. At the lowest temperature, the amplitude of line 1

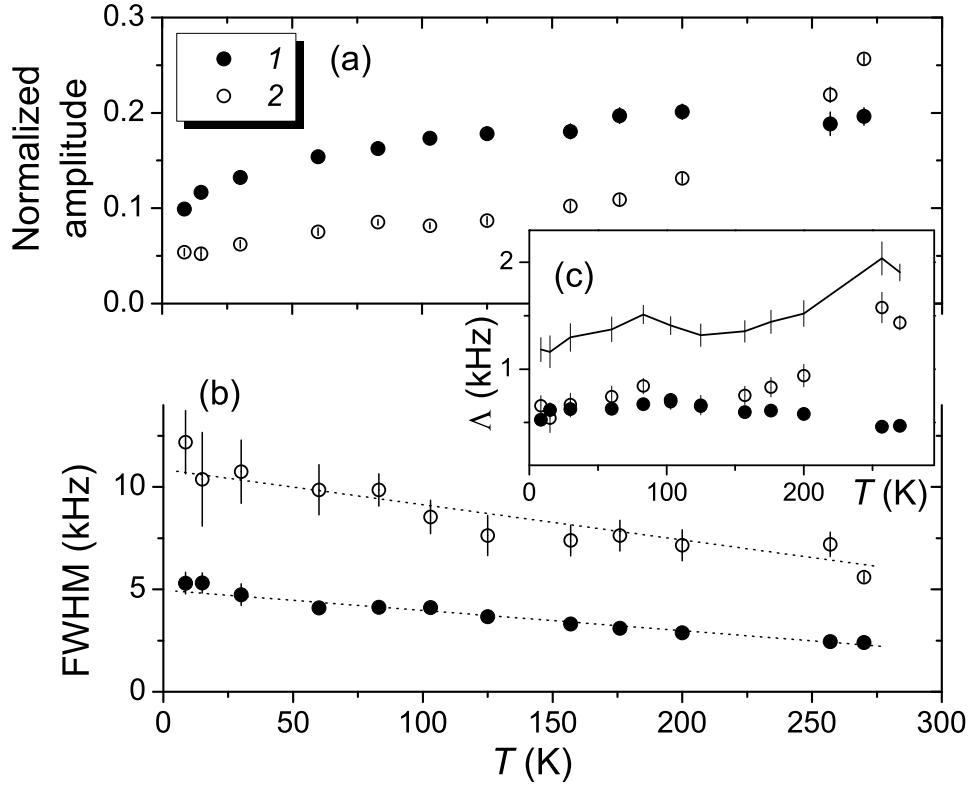


Figure 5.5: Temperature dependence of (a) the normalized amplitudes and (b) the linewidths of the two Lorentzians used in fitting the Pd resonances in the spectra of Fig. 5.1; the dotted lines are guides to the eye. (c) The area Λ of each resonance (FWHM \times Normalized amplitude); the continuous line gives their sum.

decreased by a factor of about 2, and that of line 2 by a factor of 5. In the foil, the amplitudes of these two lines are reduced by factors of about 3 and 5, respectively, at $T \simeq 10$ K.

The temperature dependence of the amplitudes of the two lines in Pd is rather distinct from those observed for ^8Li in the isostructural group 11 metals. In those hosts the linewidths are independent of temperature, and the amplitudes vary with T in accord with a thermally-induced site change, as illustrated by the data from Au in Fig. 3.4. By analogy it is tempting to attribute line 2 to Li in S sites and line 1 to Li in O sites. This implies that

the temperature range for which the Li site change occurs in Pd is higher than room T . Thus, if the measurements could be extended to higher T it would be expected that the amplitude of line 2 would continue to increase, eventually saturating at some T , while the amplitude of line 1 would decrease and eventually disappear completely. A difficulty with this scenario is the small difference in K for lines 1 and 2. In the group 11 metals, K for the S and O signals differs by a factor ~ 2 (Table 3.1), while K for the two lines of Pd differs by only a factor of ~ 1.2 . Moreover, for a site change which occurs above room T , it is unlikely that the S sites would have appreciable occupancy at the lowest temperatures and this line would not be expected to be observed for all T . The S and O sites are sufficiently distinct that Li occupying these sites should have clearly different shifts, as seen for Li in the group 11 metals; however, the unique magnetic properties of Pd may modify the shift of one or both sites such that the splitting between them is reduced. Nonetheless, the Li is taken to be stopping in only the O sites throughout the entire T range (see the Discussion). It is noted that absence of the exact knowledge of the stopping site(s) does not preclude important conclusions from being made.

The linewidths of the two Lorentzians are given in Fig. 5.5(b). They are strongly temperature-dependent, exhibiting an increase upon cooling. As found for the resonances from the foil [Fig. 4.4(a)], the width of line 2 is always greater than that of line 1. However, unlike the foil, they do not show the pronounced Curie-like impurity contribution at low T . This is consistent with this film being of higher purity. The linewidths in this film are also essentially equivalent to the values in the foil (for T above 60 K): $\sim 3 - 5$ kHz and $\sim 7 - 12$ kHz for lines 1 and 2, respectively. Put differently, the widths of both lines double upon cooling from room temperature to 8 K. In panel (c) of Fig. 5.5, the area of the two lines as a function of temperature is shown. Below 250 K, they are essentially equal and approximately constant with T . Thus, the decrease in amplitude is proportional to the increase in width, and the number of spins contributing to each site is essentially constant; this is further evidence against a thermally-induced site change.

In Fig. 5.6 the linewidths are re-plotted against T on a logarithmic scale

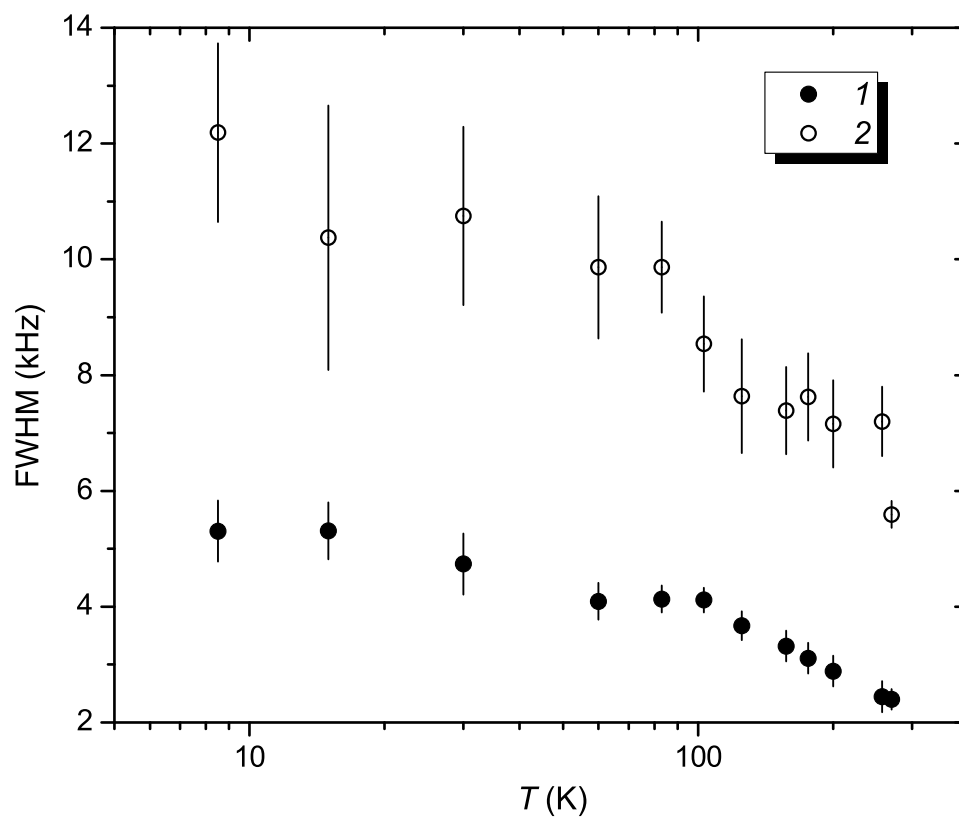


Figure 5.6: Temperature dependence of the linewidths of the two Lorentzians used in fitting the Pd resonances plotted on a semi-logarithmic scale.

providing a different perspective on their thermal variation. Such a pronounced T -dependence indicates a contribution from a mechanism other than static dipolar broadening from the host nuclei which is T -independent. The powder-average, intrinsic (van Vleck) linewidths for undistorted O and S sites in Pd are calculated to be 0.097 kHz and 0.051 kHz, respectively [Eq. (1.43)]. These are essentially equal to those in Au. The only isotope of Pd with a nuclear spin (^{105}Pd) has a gyromagnetic ratio ~ 4 times that of ^{197}Au , but has only a 22.3% natural abundance. The differences basically cancel, so in the simplest estimate, the linewidths due to the static dipolar broadening in Pd and Au are roughly the same. The linewidths observed in Pd are thus indicative of a broadening due to inhomogeneities in the T -dependent local magnetic field at the ^8Li probes. Indeed, for larger H_0 (6.55 T), the linewidths are broader, but based on the limited data, they do not broaden in proportion to the change in applied field.

Turning to the spin-lattice relaxation rates, measurements of T_1^{-1} were not performed in this film in order to avoid contamination from ions stopping in the Au capping layer. Instead, the data were collected in a piece of the same foil discussed in the previous Chapter. The data was collected for $H_0 = 4.1$ T, $E_{\text{Li}} = 28$ keV, using a beam pulse of width $\delta = 4$ s.

Representative time spectra spanning the T range studied are shown in Fig. 5.7(a) along with the corresponding fits to Eqs. (2.7) and (2.8) as these spectra were found to require two relaxing components to adequately describe the data. One component was constrained to be a small fraction (between 5 and 10%) of the total asymmetry, and have a relaxation rate an order of magnitude faster than the majority component. A possible origin for this small component is the fraction of ions that are backscattered, a second is surface contamination. Regardless, the fits demonstrate that these time spectra are well described by a single majority component. Thus, in spite of the resonance spectra being comprised of two partially resolved lines, all implanted ions can be taken to relax at the same rate for a given T . This is not unreasonable since the shifts of the two lines differ by only $\sim 20\%$, and so any small difference in the relaxation rates is not likely to be resolved in the data.

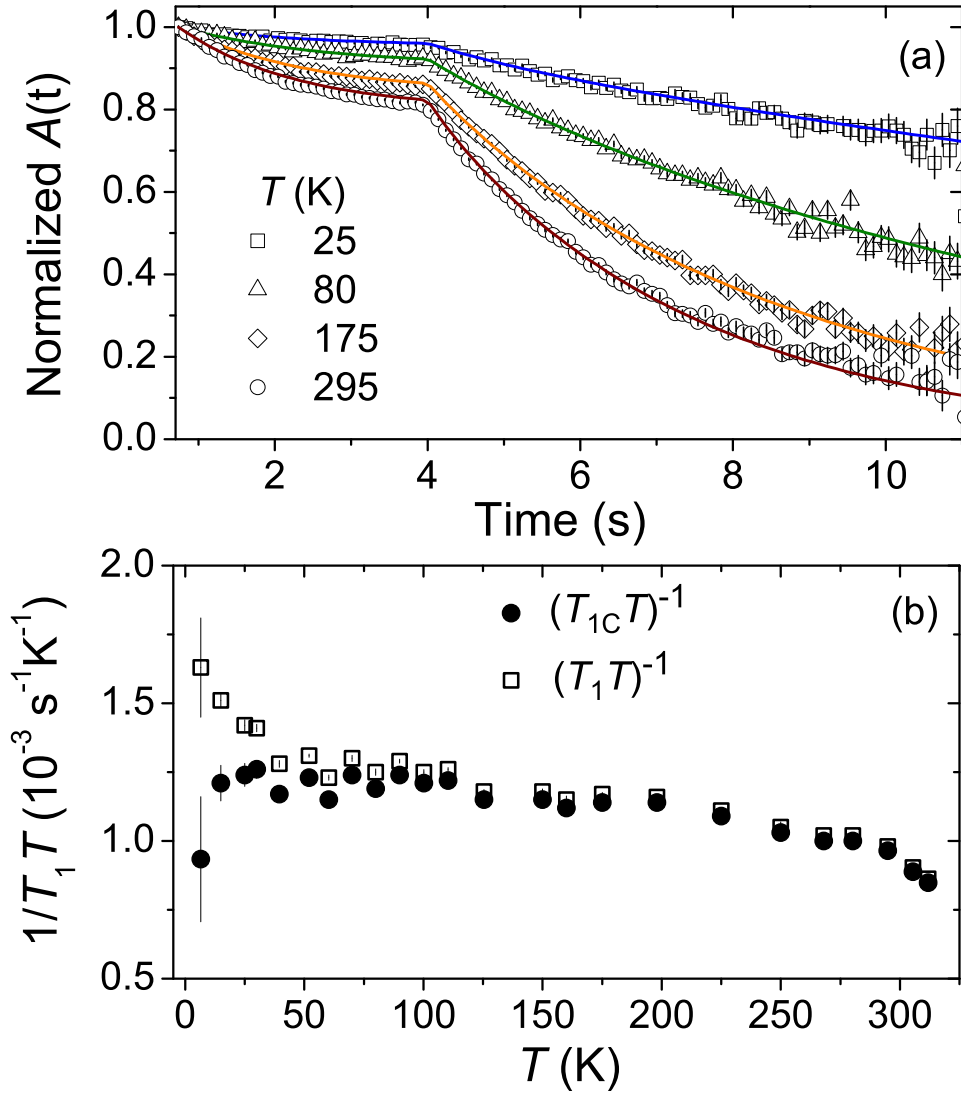


Figure 5.7: (a) Representative spin-lattice relaxation spectra recorded in the Pd foil and associated two component fits using Eqs. (2.7) and (2.8). (b) Temperature dependence of the product $(T_1 T)^{-1}$ for both T_1 and T_{1c} [the temperature dependence of T_1^{-1} is shown in Fig. 5.8(b)]. Reproduced in part from Ref. [216]. Copyright (2007) by the American Physical Society.

5.2. Results

The resulting rates for the majority fraction as a function of T are displayed in Fig. 5.8(b). The rates exhibit an overall increase with increasing T . This is also reflected by the essentially constant nature of $1/T_1T$ over most of the T range in Fig. 5.7(b). At a temperature just above T^* , T_1^{-1} becomes sub-linear. However, for $T \leq 110$ K, a linear fit to the rates yields $T_1^{-1} = 1.22(2) \times 10^{-3} \text{ s}^{-1}\text{K}^{-1}T + 4.5(9) \times 10^{-3} \text{ s}^{-1}$ [solid line in Fig. 5.8(b)]. Note the rate obtained at room T is in very good agreement with the one reported previously for ^8Li in Pd at ambient temperature by Koenig *et al.*[189]. In order to isolate only the temperature-dependent contribution to T_1^{-1} , the small T -independent term below T^* is subtracted and the resulting rates denoted by T_{1c}^{-1} . Since the T_1^{-1} data were collected over a T range spanning two orders of magnitude, the effect of this correction is most significant only at the lowest T where it removes the increase seen in $1/T_1T$. This is readily seen in the temperature dependence of $1/T_{1c}T$ that is also plotted in Fig. 5.7(b).

Measurements of ^{105}Pd T_1^{-1} show that the rate is linear below about 150 K; whereas, above this T it becomes non-linear and appears to saturate near room T [32]. This was discussed in Sec. 1.3 as being consistent with spin fluctuation theory which predicts a thermal increase in the SF amplitudes until a saturation is reached at T_{sf} whereupon they behave as effective local moments with some degree of short-range order. The ^8Li rates exhibit a saturation consistent with the accepted value of $T_{\text{sf}} \sim 250$ K for Pd[32, 95]. Very good agreement between these β -NMR rates and T_{1d}^{-1} reported from ^{105}Pd NMR[32] is evidenced in Fig. 5.9. The non-linearity of T_1^{-1} at high T is thus characteristic of the nearly ferromagnetic nature of this host; however, for T above room temperature, the limited data suggest a further decrease in T_1^{-1} . This may be an indication of the onset of a thermally-activated site change of the ^8Li . The site at higher temperature would be characterized by a smaller $|K|$, and hence a smaller slope, analogous to the decrease in the slope of T_1^{-1} seen in the simple metals[185, 186, 187]. This observation lends support to the belief that below room temperature the Li stopping site does not change.

Nuclear spin-lattice relaxation rates provide an important test of spin

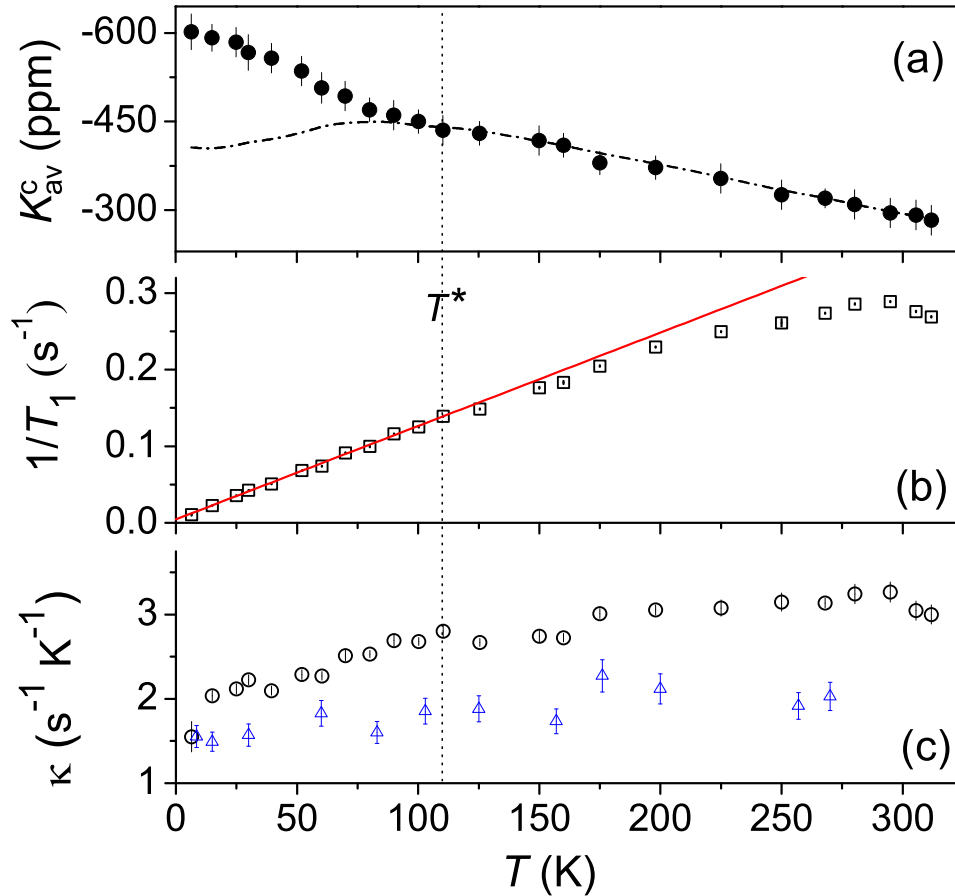


Figure 5.8: (a) Temperature dependence of K_{av}^c with some shift values interpolated/extrapolated from Fig. 5.3(c) to match those temperatures of the T_1^{-1} data in (b). In (b), the solid line is a best-fit line for the data below T^* . (c) The value $\kappa \equiv (T_1 T |K_{av}^c|)^{-1}$ as a function of T for: (circles) T_{1c}^{-1} measured in the foil and the K_{av}^c values in (a); and (triangles) T_{1b}^{-1} calculated from the baseline asymmetry values in Fig. 5.1(a). Reproduced in part from Ref. [216]. Copyright (2007) by the American Physical Society.

5.2. Results

fluctuation theory[71]. In Sec. 1.3 the observation of ferromagnetic dynamical scaling, $(T_1 T)_d^{-1} \propto \chi_d(T)$, by conventional NMR in weak ferromagnets (or strong paramagnets) was discussed. Notably, this relation was found to hold from ^{105}Pd NMR[32]. A similar analysis can be performed for the ^8Li β -NMR data following Eq. (1.41). The shifts and relaxation rates are taken to be dominated by the d electrons of the host. T_{1c}^{-1} is used such that the zero temperature intercept is zero. The slope denoted by κ is therefore equivalent to $(T_{1c} T |K_{\text{av}}^c|)^{-1}$. The resulting $\kappa(T)$ is displayed as circles in Fig. 5.8(c). The values of κ are observed to be largely constant, i.e., this scaling largely holds for $T > T^*$.

In addition, as recently demonstrated for Ag, T_1^{-1} can also be extracted from the off-resonance, baseline asymmetries A_0 [Fig. 5.1(a)] using the expression[187]

$$\frac{1}{T_{1b}} = \frac{X - A_0}{\tau A_0}, \quad (5.1)$$

where X is an adjustable scaling parameter. The value of X is chosen such that T_{1b}^{-1} coincides with T_{1c}^{-1} as $T \rightarrow 0$ where the relaxation is the slowest. The resulting rates are shown as squares in Fig. 5.9, with $1/T_{1b} T$ plotted in the inset. It is noted that these rates will contain a contribution from the ions stopping in the Au overlayer; however ion implantation simulations using TRIM.SP (Appendix B) indicate the fraction of the total implanted ions that stop in the Au is at most 5%. This tiny fraction is too small to influence the A_0 values. Furthermore, the choice of X can only shift the rates by a constant along the ordinate as their variation with temperature is dictated by the values of A_0 . Choosing X such that T_{1b}^{-1} coincides with T_{1c}^{-1} at 270 K results in a large intercept ($\simeq 0.1 \text{ s}^{-1}$), which is rather unrealistic. In fact, the value of T_{1b}^{-1} shown in Fig. 5.9 near room T is quantitatively similar to the rate measured directly at room T in an uncapped 150 nm Pd film which was grown in the same e-beam evaporator from a source of equivalent purity onto an equivalent STO substrate. This lends support to the choice of X , i.e., scaling at low T , as well as the negligible contribution from the small fraction of ions in the Au layer. It is emphasized that this method of determining the rates is indirect; in this particular case, they also include the small, fast

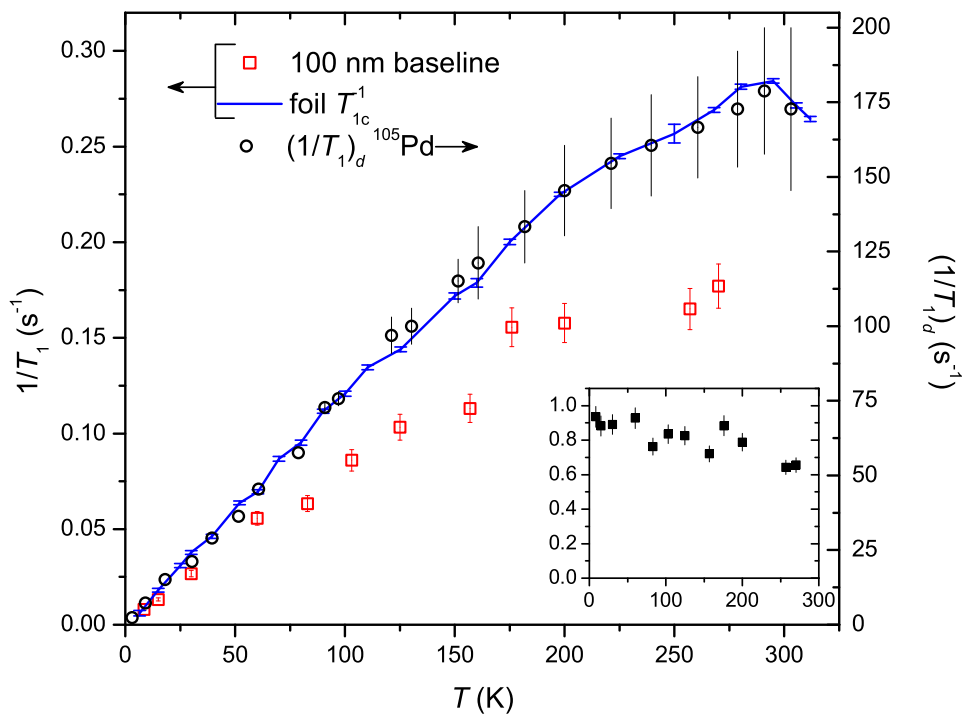


Figure 5.9: Comparison of the temperature dependence of $(T_{1c}T)^{-1}$ of ${}^8\text{Li}$ in Pd foil (line, left ordinate) with the reported d electron contribution to the relaxation rate from ${}^{105}\text{Pd}$ NMR (circles; right ordinate)[32]. The rates determined from the baseline asymmetry values T_{1b}^{-1} from the resonance spectra in the film are also shown (squares; left ordinate). Inset: $1/T_{1b}T$ ($10^{-3} \text{ s}^{-1} \text{ K}^{-1}$) plotted over the same temperature range.

component. Nonetheless, A_0 values can in principle provide an alternative way of obtaining T_1^{-1} [187], so it is interesting to compare these rates with those determined directly. The rates obtained directly from the time spectra in the foil are considered more reliable; however, the discrepancy between the two sets provides motivation for further investigation. To this end, κ calculated using T_{1b}^{-1} and the corresponding K_{av}^c are also plotted as triangles in Fig. 5.8(c). A close examination shows that for both sets of values κ begins to decrease when the temperature is lowered below about 175 K.

5.3 Discussion

The observed resonances are comprised of two partially resolved lines that exhibit similar thermal evolution of their shifts, widths and amplitudes. Inspection of the resonances in the separate helicities does not indicate a quadrupolar origin. By comparison with other fcc metals, one is lead to the conclusion that the Li ions predominantly come to rest in the O sites over the whole T range employed. This implies that there is a slight difference in the hf interaction for a fraction of the ions although they all occupy the same crystallographic lattice site.

This proposal is further substantiated by preliminary results from ^8Li β -NMR of a 100 nm (111)-oriented *single crystal* film of Pd grown epitaxially on an equivalent STO substrate[210]. The resonances from this sample (not shown) exhibit identical relative shifts as a function of temperature, but more importantly, they appear as a single, narrower line as opposed to two overlapping ones. The resonance labelled 2 in the foil and the polycrystalline film discussed here is essentially absent in the single crystal spectra. The major difference between polycrystalline and single crystal specimens is the greater degree of orientation and lack of grain boundaries in the latter. Thus, it is suggested here that the two lines observed in polycrystalline samples arise from ions are indeed in the same sites (O), but are distinct as a consequence of the orientational heterogeneity. This implies the local magnetic field probed by the ^8Li depends on the orientation of the lattice with respect to H_0 , albeit slightly. The two lines can then arise as a result of

a powder-average over the randomly distributed lattice orientations in the following manner. It is assumed that the local magnetic field at the probes varies sinusoidally as a function of the angle of H_0 with respect to the local cubic axes of the crystallites. While the film is largely textured in the (111) direction along the normal to the plane, the orientation of the crystallites is completely random in the plane, and so this angle is also assumed to be distributed randomly (i.e., the arcsine distribution with its two singularities). The probability density is thus concentrated at the boundary values, yielding two predominant local magnetic fields that produce the two lines with differing shifts. The fact that the resonances also become narrower as the degree of orientation is increased indicates that the linewidths are also reflective of this crystallographic inhomogeneity.

Turning to the susceptibility enhancement probed by the Li, the temperature dependence of the Korringa ratio \mathcal{K} [Eq. (1.26)] is shown in Fig. 5.10. \mathcal{K} exhibits a continual increase with decreasing T for both sets of T_1^{-1} . Near room temperature the enhancement is roughly equal to that obtained in ^{105}Pd NMR[21] at 4 K, denoted by (\star), while at the lowest temperatures it is ~ 3 times larger. Thus, even near room temperature, \mathcal{K} is almost 10 times larger for ^8Li in Pd than for ^8Li in the group 11 metals (Table 3.1).

At low temperatures the effects of the spin fluctuations are not as significant and Eq. (1.28) can be applied to demonstrate the large ferromagnetic enhancement of the local susceptibility in the ground state for the ^8Li probes. The parameter $K(\alpha_0)$ is used to quantify the enhancement in materials with strong electron interactions that may affect the shift and the relaxation rate differently (i.e., the \mathbf{q} dependence of χ). From Fig. 5.10, taking $\mathcal{K} \simeq 30$ as $T \rightarrow 0$ gives $K(\alpha_0) \approx 0.14$. By comparison $K(\alpha_0) = 0.19$ is determined from the ^{105}Pd NMR measurements[32], and calculations for Pd predict[32, 217] $K(\alpha_0) \sim 0.23$. Thus, the ratio $K(\alpha_0)_{\text{exp}}/K(\alpha_0)_{\text{calc}} \sim 0.6$ for ^8Li in Pd, whereas for the host it is ~ 0.8 [32, 71]. It is noted that \mathcal{K} is calculated from K_{av}^c values that have not been corrected for any K^{orb} . However, as K^{orb} is likely small, this is not expected to be a significant problem, particularly in comparison to the large values of the shifts at the lowest temperatures.

Small values of $K(\alpha_0)$ are characteristic of the enhanced paramagnetic

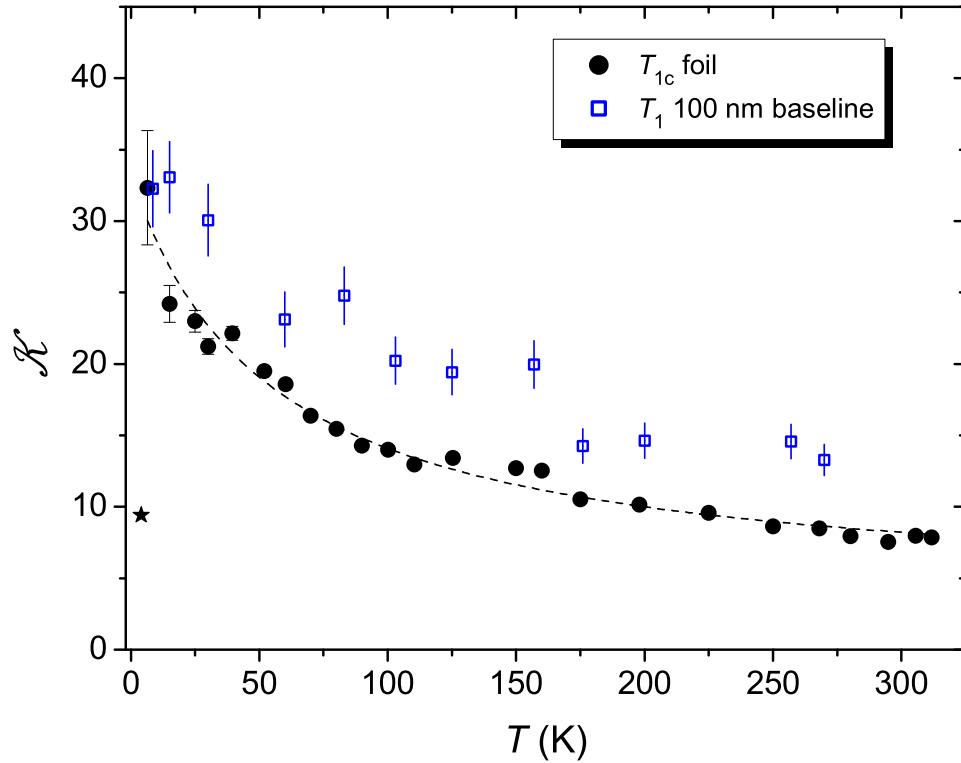


Figure 5.10: Temperature dependence of the Korringa ratio \mathcal{K} calculated for K_{av}^c and T_{1c} or T_{1b} . The dashed line is a guide to the eye. (\star) denotes the value reported from ^{105}Pd NMR at 4 K[21].

state of nearly, or weakly, ferromagnetic metals, i.e., for enhancements of the susceptibility that are confined to a small region around $\mathbf{q} \simeq 0$. Moreover, they are an indication of the absence of any localized moments. By contrast, for systems with localized impurity moments, $K(\alpha_0) \sim 1$ and the susceptibility is enhanced uniformly in q -space[71]. The ^8Li data yield a small $K(\alpha_0)$ implying the susceptibility is enhanced in a small region of q -space. The localized nature in q -space means the enhancement is extended in real space.

The variation of $K(\alpha_0)$ has been calculated for various values of α_0 [44, 45, 217]. Recall that α_0 is a phenomenological measure of electron-electron interactions, such that the Stoner enhancement factor can be approximated as $\mathcal{S} \approx (1 - \alpha_0)^{-1}$. The above $K(\alpha_0)$ values for ^8Li in Pd of $\approx 0.12 - 0.14$ correspond to $\alpha_0 \approx 0.95 - 0.96$, yielding $\mathcal{S} \sim 20 - 25$. Thus, the local susceptibility probed by ^8Li χ_{loc} is enhanced by a factor of at least 2 over that of the pure host (as $T \rightarrow 0$).

In Ref. [196], K of Li at O sites in Pd is reported from calculation to be ~ -700 ppm at 0 K. This agrees fairly well with the present low- T K_{av}^c . However, no details of the calculation were provided, so it is not known what value of χ_{Pd} was used to generate this shift and the agreement may be fortuitous. It is reasonable that the deviation of the shifts from the host susceptibility below T^* is related to the presence of the $^8\text{Li}^+$ probe. No observation of such an enhancement by any other implanted probe in this metal has been reported to date.

In addition to the electronic modification of the host arising from the hybridization of the Li $2s$ orbital with the d band, the local lattice relaxation about the probe needs to be taken into consideration as a major factor in determining χ_{loc} . Indeed, in keeping with the assumed assignment of the Li probes to the O sites, a local expansion of the host lattice is thus expected as discussed in Sec. 1.4. Importantly for Pd, a lattice expansion is predicted to lead to a ferromagnetic ground state[135, 136, 137, 138, 139, 140]. Moreover, Hjelm predicts that a lattice expansion will also significantly decrease the critical field for a metamagnetic transition, concomitant with an increasing orbital susceptibility with increasing applied field[133]. By comparison to

the reported lattice expansions of octahedral interstitial H, B, and C in Pd[218], Li can be estimated to produce an expansion $\sim 10\%$, sufficient to substantially enhance the susceptibility.

Further, due to the anisotropy of the elastic constants of Pd, the magnitude of the expansion is expected to depend on crystallographic orientation[221]. However, the expansion must maintain the cubic symmetry of the stopping site as there is no evidence for a quadrupole splitting due to an EFG at the Li site. It is possible that the site is slightly non-cubic producing a small EFG that gives rise to an unresolved, T -independent broadening of the resonances. Regardless, this anisotropy is in keeping with the suggested origin of the two resonance lines in polycrystalline specimens, although no anisotropy of the resonances has been observed for ^8Li in other cubic metals. The source of this proposed anisotropic hf field must not depend strongly on temperature as the splitting between the lines is approximately constant throughout the temperature range. One possible origin is the spin-orbit interaction which, due to the orbital motion of the electrons in the presence of a magnetic field, can impart a preferred direction to the susceptibility[219, 220]. This may further be related to the specific geometry of the crystallites. Slight differences in the temperature dependence of the local lattice relaxation may also contribute to the inhomogeneity of χ_{loc} that is evidenced through the temperature dependence of the linewidths.

Furthermore, the volume dependence of the susceptibility of enhanced magnetic metals is generally attributed to the volume dependence of the Stoner parameter (i.e., of \bar{I})[222, 223, 224, 225] which is taken to be a local atomic property, so this is consistent with the perturbation being confined to a region of the Pd lattice in the immediate vicinity of the Li. Recall, Zeller *et al.* suggest that a small temperature dependence of I_0 ($\sim 1\%$) is sufficient to account for the entire temperature dependence of χ_{Pd} [109]. Thus, it is not unreasonable to consider a small enhancement of this parameter for, at least, the Pd atoms nearest to the Li as a major contribution to χ_{loc} .

A more intriguing characteristic of χ_{loc} is found by examination of the temperature behaviour of the inverse of the shifts. In Fig. 5.11 $|K_{\text{av}}^c|^{-1}$

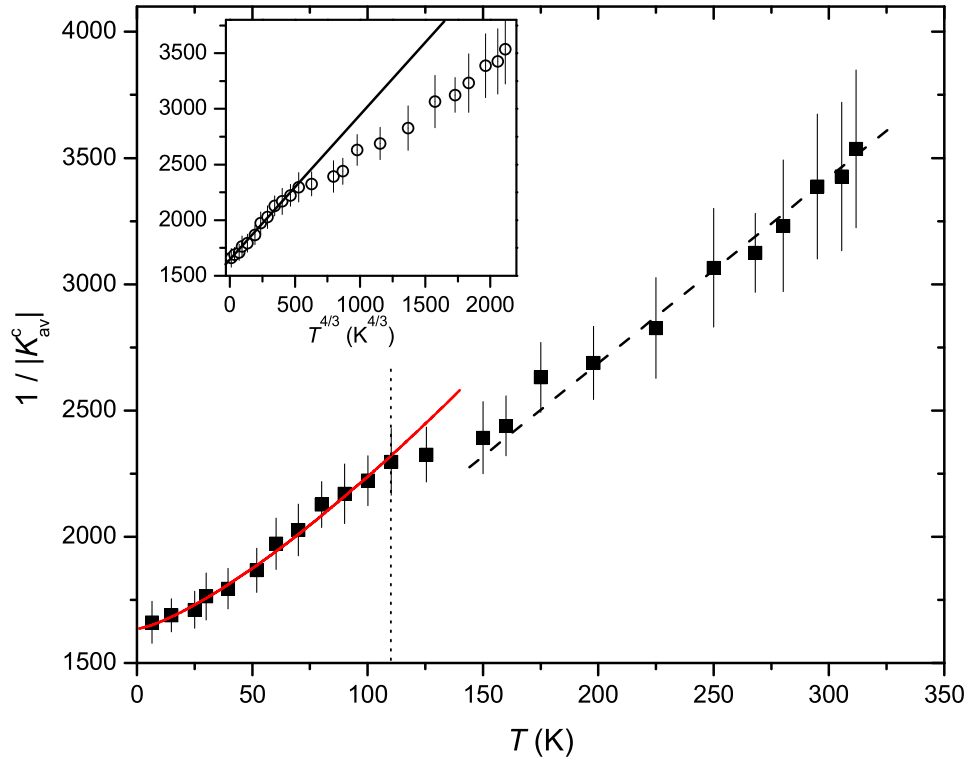


Figure 5.11: Apparent $T^{4/3}$ dependence of $1/|K_{av}^c|$ (unitless) below T^* (red line). The dotted line marks T^* . For temperatures above 150 K, K_{av}^c exhibits the same CW behaviour as the host (dashed line; guide to the eye). The inset shows $1/|K_{av}^c|$ (unitless) plotted against $T^{4/3}$.

5.3. Discussion

(taken $\propto \chi_{\text{loc}}^{-1}$) is plotted as a function of T . For temperatures above ≈ 150 K, the inverse shifts are seen to follow the CW behaviour of the host susceptibility[32]; however, for $T < T^*$, they appear to be well described by a behaviour $\propto T^{4/3}$ as illustrated by the red line and in the inset. This holds most strongly for temperatures below 50 K. Such a temperature dependence is predicted from spin fluctuation theory for χ^{-1} of an itinerant ferromagnet (in 3 dimensions) over a wide range of T just above the transition temperature[54, 79, 87, 226]. This has also been experimentally observed by magnetometry in several weak metallic ferromagnets where T_C was tuned via chemical doping[227, 228, 229]. For instance, the temperature behaviour shown in Fig. 5.11 is identical with that reported in Ref. [227] for Nb-doped ZrZn_2 for a Nb concentration slightly above the critical concentration for which T_C is suppressed to zero. The present results strongly point to enhanced spin fluctuations in the region about the Li that further enhance the propensity for ferromagnetic order, although there is no evidence for static ordering.

The Li may be characterized as “nucleating” a region in its vicinity that is even closer to ferromagnetic order than the enhanced paramagnetic host. This is similar to “droplets” of local order in an otherwise non-ordered background that are theoretically predicted to be induced by defects in metals that are proximal to magnetic groundstates[230]. The clear distinction here is that there is no evidence of any long-range ferromagnetic order induced by the Li. The notion of a droplet of locally stronger enhancement may indeed be a useful way to view the present results, in some ways analogous to the concept of a magnetic polaron[231]. While the spin-lattice relaxation rates show a linear increase with increasing T , consistent with the Korringa mechanism, they are far slower than predicted from K^c using the Korringa relation. This is surprising since a stronger local enhancement of the susceptibility would be predicted to give rise to stronger fluctuations thereby increasing T_1^{-1} , particularly at lower temperatures. However, as pointed out by Lederer[232] for the case of an isolated magnetic impurity in a nearly ferromagnetic host, a local breakdown of the Korringa relation can be expected. This is due to the differing \mathbf{q} dependence of K and T_1^{-1} . The shift

is sensitive to the static uniform susceptibility which, as discussed above, is consistent with a large ferromagnetic enhancement in the region $\mathbf{q} \simeq 0$. Referring to Eq. (1.40), it is seen that T_1^{-1} depends on a sum over all \mathbf{q} components, and is less affected by the small region around $\mathbf{q} = 0$ where the uniform susceptibility is most enhanced. Thus, a stronger local enhancement of the susceptibility need not correspond to faster relaxation rates. This is equivalently manifest by the change in κ below T^* .

5.4 Conclusions

In this Chapter a more detailed analysis of the behaviour of $^8\text{Li}^+$ in a high-purity, 100 nm Pd film was presented. The Knight shifts scale with χ_{Pd} as the temperature is lowered from room temperature down to $T^* = 110$ K. This behaviour is similar to that observed in the foil indicating the behaviour is intrinsic to ^8Li in Pd. The resonances appear as two partially resolved signals throughout the T range, but do not exhibit the thermal variation in amplitudes (areas) of the resonances observed in other fcc metals. The two lines are not assigned to ^8Li stopping in distinct lattice sites, but are instead taken to arise from ions in O sites that experience a subtly different hf fields as a consequence of the lattice orientation. A powder-average of crystallite orientations with respect to H_0 is suggested to give rise to a local hf field probability distribution that is concentrated at two values.

The linewidths are too broad to be solely from host nuclear dipoles, and must be of magnetic origin. They are strongly dependent on temperature, doubling as T is lowered from room temperature down to 8 K. However, they do not show any sign of a Curie-like increase at the lowest temperatures due to dilute magnetic impurities as in the case of the foil. The resonance amplitudes decrease monotonically with decreasing T . This is simply a consequence of the line broadening as the resonance areas remain essentially constant.

Spin-lattice relaxation rates measurements in the foil, and extracted from the resonance baseline asymmetries in the film, reveal an initial linear increase with T at low temperatures, with an eventual saturation at higher

5.4. Conclusions

temperatures. The rates in the foil have a temperature dependence that is identical to the d contribution to T_1^{-1} reported from conventional NMR of the host. The data is observed to satisfy the relation predicted for ferromagnetic SFs of $(T_1 T)^{-1} \propto K_{\text{av}}^c(T)$ for $T > T^*$.

Correspondingly, the local susceptibility probed by Li is enhanced over that of the host below T^* , and for $T \rightarrow 0$ this corresponds to a Stoner enhancement that is a factor of at least 2 greater than the pure host susceptibility. The origin of this enhancement is not definite at present. However, the importance of a local lattice expansion about the putative interstitial ions, and an increase in the electron interaction parameter on the neighbouring Pd atoms are pointed out in this regard. The inverse of the shifts for $T < T^*$ can be described by a $T^{4/3}$ variation which is expected for itinerant ferromagnetic metals in a range of temperatures just above T_C . This can be viewed as the Li inducing a region locally that is closer to ferromagnetic order— a droplet of “super-enhancement.” However, the spin-lattice relaxation rates do not exhibit a corresponding enhancement. This intriguing observation requires further study, e.g., as a function of applied field, and calls for *ab initio* calculations specifically treating the response of Pd to such isolated defects.

Chapter 6

Summary and Future Prospects

The results presented here describe the successful application of the β -NMR technique to study the magnetism of transition metals. In particular, two metals at the extremes of paramagnetism; namely, non-magnetic Au and strongly exchange-enhanced, nearly ferromagnetic Pd. These results serve as clear demonstrations of the power of this implanted probe technique for studying materials typically not accessible by conventional NMR. Both metals were studied in the form of macroscopic foils, and also as thin films. The latter samples illustrate the advantage of the TRIUMF low-energy β -NMR facility using in-flight, optical polarization of the ions. Most other implementations of the β -NMR technique rely on polarized ions produced by nuclear reactions which are subsequently implanted at MeV energies, thus precluding their application to the study of thin film samples. This is a testament to the immense potential of low-energy β -NMR for investigating the magnetism of materials in reduced geometries, with the capability of depth-resolved measurements when desired.

In a broader context, this work expands the knowledge of the hyperfine interaction of implanted probes, as previous use of ^8Li as a β -NMR probe in either Au and Pd was scarce. First-principle calculations of the hyperfine fields at impurities are stringent tests of theory. It is thus desirable to test existing theories with as many probe-host combinations as possible. Only in this way can potential deficiencies in present theories be identified and improvements attempted, which may ultimately lead to new and more accurate predictions. Calculations of the hf interaction of ^8Li in the group 11

metals and Pd would certainly be desirable, not only in light of the present results, but also in aiding the direction future studies.

Overall, the behaviour of ^8Li in Au is very similar to that observed in the other simple metals. Two distinct, narrow resonances are observed whose frequencies do not show any dependence on temperature, in keeping with the temperature-independent Pauli susceptibility. Only single resonances are observed with no indication of quadrupole splitting, indicative of well-defined, crystallographic stopping sites of cubic symmetry. Similar to the case of the other three metals, these are taken to be the octahedral interstitial and substitutional lattice sites. The resonance from ions in the latter site appears only for temperatures greater than about 150 K, and is attributed to a thermally-induced site change from the metastable interstitial site. The linewidths are quite narrow and are not dependent on temperature (they broaden slightly in the T range of the site change). Such narrow lines are also observed in Ag, but not in Al or polycrystalline Cu where the two resonances are so broad they cannot be resolved. On the basis of the present data, a comparison of the observed widths (in the limit of small H_1) with the calculated rigid-lattice dipolar widths is highly suggestive of a local expansion about the interstitial ions and a local contraction about the substitutional ions. No dependence on the mean implantation depth of the probes was found for the resonances in Au.

The spin-lattice relaxation rate is independent of applied field for fields greater than at least 15 mT. The rate at room temperature is less than half as fast as that in the other three metals, and this is a notable distinction for Au. Application of the Korringa relation for the substitutional ions yields a ratio that is little enhanced over that predicted for a free-electron gas, i.e., $\mathcal{K} \approx 1$, and this is also the case for the other three metals. Except for Al where they are equal, the ^8Li enhancement values are slightly smaller than those reported for the host nuclei by conventional NMR; the “disenhancement” being greatest for Ag. Thus, the Li is not generating any significant electronic correlations in its vicinity in these metals, signifying that it is indeed probing their intrinsic electronic structure.

Preliminary T_1^{-1} data as a function of temperature in Au (not included

herein) are indicative of a rate that increases linearly with T , in keeping with the Korringa mechanism of relaxation due to conduction electron spin-flip scattering. The slope decreases in the T range of the site change. This is analogous to what is observed in the other three simple metals. A study of the intrinsic linewidths should be carried out as a function of larger H_0 to be certain that the values are determined in the high-field limit where the quadrupolar interaction for the host spins is not a complication. In this regard, given that ^{197}Au is 100% abundant ($I = \frac{3}{2}$), it may be interesting to attempt cross-relaxation measurements with ^8Li in this host as well, which have already been undertaken for ^8Li in Cu[233].

The inertness of Au makes it prevalent as a protective capping layer for many samples. Given its tendency to form flatter films[234] and its higher density (i.e., greater stopping power), Au is an appealing candidate for proximal magnetometry by ^8Li β -NMR. Indeed, the induced magnetic polarization of Au layers in contact with $3d$ ferromagnet layers is a topic that has received little experimental attention[235]. The larger spin-orbit coupling of Au can be expected to result in a magnetic coupling at the interfaces that is distinct from that of other simple metals.

Turning to the results in Pd, the enhanced paramagnetism of this metal makes β -NMR of this host more complicated, but simultaneously richer than the simple metals. The results obtained are far from being fully understood, and more work is needed; first-principle calculations would clearly be beneficial in this regard.

The measured Knight shifts are negative for all temperatures studied, and this is consistent with calculations of the hf field at ^8Li in ferromagnetic hosts like Ni as a consequence of the strong spin polarization from the d electrons. The shifts track the temperature-dependent susceptibility of the host for $T > T^* \approx 110$ K, which is in keeping with the results of other implanted probes like μ^+ and ^{12}B , as well as conventional NMR. However, below this temperature the scaling breaks down; the local susceptibility probed by the ^8Li thus includes a contribution representing the response of the host to the isolated defect and is no longer representative of the pure host. Such a deviation from the host χ is hardly seen in the muon Knight

shifts in Pd. The previous ^{12}B (and ^{12}N) β -NMR measurements of Pd did not extend below 100 K, so this appears to be a rare observation by NMR of the temperature evolution of such a “defect” state in this metal. While not a huge effect, the local susceptibility at the probe below T^* is greater ($\sim 30\%$) than that of the pure host and is consistent with the temperature dependence expected for a weak ferromagnet in three dimensions just above T_C ; although, there is no evidence for static ordering.

The resonances appear as two partially resolved lines, but there is no indication of a quadrupolar splitting. The amplitudes of the resonances decrease with decreasing T due to line broadening. The resonances are significantly broader than predicted for host spin dipolar broadening pointing to a likely magnetic origin. The behaviour is not in keeping with the thermally-induced site changes observed in the isostructural simple metals. Assignment of the lattice location(s) for the implanted ions is correspondingly difficult; the analysis presented here assumes only the octahedral interstitial site is occupied to any appreciable extent. The observation of two resonances from the same stopping site leads to the suggestion that the hf interaction is anisotropic; the pair of resonances arise due to an average over the random distribution of crystallite orientations with respect to H_0 .

The spin-lattice relaxation rates measured in a foil sample initially increase with increasing T , but become sub-linear above T^* tending to saturate near room temperature. This is in keeping with the spin fluctuation-dominated relaxation reported from ^{105}Pd conventional NMR. Additionally, below T^* where the shifts indicate a local enhancement of the static susceptibility, T_1^{-1} remains slower than expected. Above room T , T_1^{-1} further decreases analogous to that observed in the T range of the thermally-induced site changes in the fcc simple metals. Higher temperature measurements would be useful, but this requires a high temperature oven not presently available. If the T_1^{-1} is instead calculated using the baseline asymmetries from the resonances in a 100 nm film, a similar behaviour with T is observed, but a stronger saturation occurs at a lower T ($\simeq 175$ K) to a rate that is roughly half as fast as that measured in the foil. Thus, a consistent determination of both K and T_1^{-1} in the *same film* sample is a more

desirable situation.

Nonetheless, the shifts and relaxation rates could be analyzed analogous to conventional NMR data to show that the prediction from spin fluctuation theory of ferromagnetic dynamical scaling holds for ^8Li β -NMR of Pd. This demonstrates that β -NMR can be used to study the spin fluctuation (SF) spectra of enhanced, or weakly, magnetic materials in a manner analogous to conventional NMR. μSR can be used to probe the spin dynamics in such systems[236], but the technique of β -NMR has not been applied for this purpose. In this regard, the information obtained are complementary to that from conventional NMR or inelastic neutron scattering, since light implanted probes can access the interstitial regions and the presence of the probe itself may affect the SFs locally. These additional perspectives on SFs can be valuable in testing and refining theory, and thus further the understanding of the role of these magnetic excitations of a given material and the occurrence of magnetism in general. For example, a possible initial candidate for this type of study by β -NMR is the well-known, prototypical weak ferromagnet Ni_3Al . This system crystallizes in a structure that is analogous to the fcc lattice of a pure metal, and recently susceptibility[228] and ^{27}Al NMR[124] were used to study the evolution of the SF spectrum following C intercalation into the octahedral interstices.

Clearly further β -NMR of Pd is still in order. The onset of the intriguing enhancement of the susceptibility is near 100 K, a relatively high temperature in comparison to other “low temperature” phenomena. The Li may be viewed as inducing a region of enhanced spin fluctuations that is locally closer to ferromagnetic order than the pure host, described as a “droplet” of super-enhancement. By all other reports, non-magnetic impurities cause a *reduction* in the susceptibility of Pd. Thus, the origin of this effect certainly deserves further investigation, and may also provide new insights into the origin of the maximum observed in the susceptibility of the pure host.

Immediate future measurements should be extended to lower temperatures, as well as carried out as a function of H_0 , particularly for lower values than employed here. Systematic studies of the shifts, linewidths, and T_1^{-1} as a function of applied field may be useful in elucidating the origin of the

Li's influence on the susceptibility. Also, the use of single crystal specimens of different orientation, or alternatively, rotating a single crystal with respect to H_0 , would be useful in addressing the proposed anisotropy of the hf interaction.

Finally, some future extensions of β -NMR of Pd are mentioned. The first involves the use of Pd layers in ^8Li proximal magnetometry, or in studies of induced magnetic polarization. While more complicated than simple metals like Ag or Au, magnetic polarization of Pd is far more facile. It is also likely to yield a much more fascinating spatial response for which low-energy β -NMR, with its depth resolution capability, is ideally equipped to study. Indeed, it has been long known that Pd in contact with a ferromagnetic substrate becomes polarized ferromagnetically, and that in many cases this polarization extends a considerable distance from the interface[237, 238, 239, 240, 241, 242, 243]. It is quite conceivable that β -NMR could easily address many aspects of these systems, like the temperature, applied field, and distance dependence of this magnetic coupling. Rather analogous to the magnetic proximity effect, is the proximity effect from a superconductor. There is considerable interest in understanding how the occurrence of superconductivity is influenced at the interface between a superconductor and a ferromagnet, or equally an enhanced paramagnet[244]. A recent example is such a study in Pd/Nb bilayers[245].

The second potential extension involves the study of Pd samples of reduced size. Owing to the strong dependence of the susceptibility on the lattice structure, rather dramatic effects in the β -NMR of Pd can be expected for samples of thin films or supported nanocrystals[246]. In fact, preliminary ^8Li β -NMR results of thinner Pd films reveal a remarkable reduction in the Knight shift as a function of thickness[247]; cf. Fig. 2.5(b). Further studies along this line would certainly be a valuable contribution towards the understanding of magnetism at the nanoscale. In this regard, the giant enhancement of the susceptibility observed for epitaxially strained thin Pd in Au/Pd/Au sandwiches is recalled[139]. A multilayer comprised of several repeating units of these sandwiches could easily be studied by low-energy β -NMR, and the results would be of use in clarifying the influence

of lattice strain on the susceptibility.

Bibliography

- [1] J. Kübler, *Theory of Itinerant Electron Magnetism* (Clarendon, Oxford, 2000).
- [2] N.W. Ashcroft and N.D. Mermin, *Solid State Physics* (Holt-Saunders, Philadelphia, 1976).
- [3] C. Kittel, *Introduction to Solid State Physics*, 6th ed. (Wiley, New York, 1986).
- [4] R.M. White, *Quantum Theory of Magnetism*, 2nd ed. (Springer-Verlag, Berlin, 1983).
- [5] J.J. van der Klink and H.B. Brom, Prog. Nucl. Magn. Reson. Spectrosc. **36**, 89 (2000).
- [6] P.K. Misra and L. Kleinman, Phys. Rev. B **5**, 4581 (1972).
- [7] M. Yasui, T. Takahashi, and J. Callaway, J. Phys.: Condens. Matter **3**, 2679 (1991).
- [8] The original reference for this is: R. Kubo and Y. Obata, J. Phys. Soc. Jpn. **11**, 547 (1956).
- [9] R. Huguenin, G.P. Pells, and D.N. Baldock, J. Phys. F **1**, 281 (1971).
- [10] J. Benkowitsch and H. Winter, Z. Phys. B **50**, 217 (1983).
- [11] M. Deng, H. Freyer, J. Voitländer, and H. Ebert, J. Phys.: Condens. Matter **13**, 8551 (2001).

Bibliography

- [12] V. Jaccarino, in *Proceedings of the International School of Physics, Enrico Fermi, Course XXXVII: Theory of Magnetism in Transition Metals*, edited by W. Marshall (Academic, New York, 1967), pp. 335–385.
- [13] A.J. Manuel and J.M.P. St. Quinton, Proc. R. Soc. London Ser. A **273**, 412 (1963).
- [14] J.A. Seitchik, A.C. Gossard, and V. Jaccarino, Phys. Rev. **136**, A1119 (1964).
- [15] H.C. Jamieson and F.D. Manchester, J. Phys. F **2**, 323 (1972).
- [16] F.H. Spedding and J.J. Croat, J. Chem. Phys. **58**, 5514 (1973).
- [17] R.J. Stierman, K.A. Gschneidner, Jr., T.-W.E. Tsang, F.A. Schmidt, P. Klavins, R.N. Shelton, J. Queen, and S. Legvold, J. Magn. Magn. Mater. **36**, 249 (1983).
- [18] N. Inoue and T. Sugawara, J. Phys. Soc. Jpn. **44**, 440 (1978).
- [19] J. Winter, *Magnetic Resonance in Metals* (Clarendon, Oxford, 1971).
- [20] C.P. Slichter, *Principles of Magnetic Resonance*, 3rd. ed. (Springer-Verlag, Berlin, 1990).
- [21] G.C. Carter, L.H. Bennett, and D.J. Kahan, *Metallic Shifts in NMR*, Progress in Materials Science Vol. 20, edited by B. Chalmers, J.W. Christian, and T.B. Massalski (Pergamon Press, Oxford, 1977), Pt. 1.
- [22] C.H. Townes, C. Herring, and W.D. Knight, Phys. Rev. **77**, 852 (1950).
- [23] W. Götz and H. Winter, J. Phys.: Condens. Matter **5**, 1707 (1993).
- [24] A. Abragam and B. Bleaney, *Electron Paramagnetic Resonance of Transition Metal Ions* (Clarendon, Oxford, 1970).
- [25] G.D. Gaspari, W.-M. Shyu, and T.P. Das, Phys. Rev. **134**, A852 (1964).

Bibliography

- [26] A.M. Clogston, V. Jaccarino, and Y. Yafet, *Phys. Rev.* **134**, A650 (1964).
- [27] M. Shaham, U. El-Hanany, and D. Zamir, *Phys. Rev. B* **17**, 3513 (1978).
- [28] R. Krieger and J. Voitländer, *Z. Phys. B* **40**, 39 (1980).
- [29] H. Akai and T. Kotani, *Hyperfine Interact.* **120-121**, 3 (1999).
- [30] M. Battocletti and H. Ebert, *Phys. Rev. B* **64**, 094417 (2001).
- [31] K. Terakura, N. Hamada, T. Oguchi, and T. Asada, *J. Phys. F* **12**, 1661 (1982).
- [32] M. Takigawa and H. Yasuoka, *J. Phys. Soc. Jpn.* **51**, 787 (1982).
- [33] T. Asada, K. Terakura, and T. Jarlborg, *J. Phys. F* **11**, 1847 (1981);
corrigendum: **14**, 1989 (1984).
- [34] J.B. Boyce and C.P. Slichter, *Phys. Rev. Lett.* **32**, 61 (1974).
- [35] J. Owen, M. Browne, W.D. Knight, and C. Kittel, *Phys. Rev.* **102**, 1501 (1956).
- [36] L.D. Graham and D.S. Schreiber, *Phys. Rev. Lett.* **17**, 650 (1966).
- [37] R.E. Walstedt and L.R. Walker, *Phys. Rev. B* **9**, 4857 (1974).
- [38] e.g., L.L. Lumata, K.Y. Choi, J.S. Brooks, A.P. Reyes, P.L. Kuhns, G. Wu, and X.H. Chen, *J. Phys.: Condens. Matter* **22**, 295601 (2010).
- [39] T. Moriya, *J. Phys. Soc. Jpn.* **18**, 516 (1963).
- [40] W.W. Warren, Jr., G.F. Brennert, and U. El-Hanany, *Phys. Rev. B* **39**, 4038 (1989).
- [41] The original reference to this is: J. Koringa, *Physica* **16**, 601 (1950).
- [42] Y. Yafet and V. Jaccarino, *Phys. Rev.* **133**, A1630 (1964).
- [43] Y. Obata, *J. Phys. Soc. Jpn.* **18**, 1020 (1963).

Bibliography

- [44] A. Narath and H.T. Weaver, Phys. Rev. **175**, 373 (1968).
- [45] R.W. Shaw, Jr. and W.W. Warren, Jr., Phys. Rev. B **3**, 1562 (1971).
- [46] B.S. Shastry and E. Abrahams, Phys. Rev. Lett. **72**, 1933 (1994).
- [47] H.-O. Lee and H.-Y. Choi, Phys. Rev. B **62**, 15120 (2000).
- [48] e.g., R.E. Walstedt and Y. Yafet, Solid State Commun. **15**, 1855 (1974).
- [49] F.E. Hoare and J.C. Matthews, Proc. R. Soc. London Ser. A **212**, 137 (1952).
- [50] E. Şaşıoğlu, C. Friedrich, and S. Blügel, Phys. Rev. B **83**, 121101(R) (2011).
- [51] V. Thakor, J.B. Staunton, J. Poulter, S. Ostanin, B. Ginatempo, and E. Bruno, Phys. Rev. B **68**, 134412 (2003).
- [52] e.g., I.D. Hughes, M. Däne, A. Ernst, W. Hergert, M. Lüders, J. Poulter, J.B. Staunton, A. Svane, Z. Szotek, and W.M. Temmerman, Nature **446**, 650 (2007).
- [53] E.C. Stoner, Proc. R. Soc. London Ser. A **154**, 656 (1936); **165**, 372 (1938).
- [54] G.G. Lonzarich, in *Electron: A Centenary Volume*, edited by M. Springford (Cambridge University Press, Cambridge, 1997), Chap. 6.
- [55] P.A. Wolff, Phys. Rev. **120**, 814 (1960); T. Izuyama, D.-J. Kim, and R. Kubo, J. Phys. Soc. Jpn. **18**, 1025 (1963).
- [56] S. Doniach, Proc. Phys. Soc. London **91**, 86 (1967).
- [57] J. Wahle, N. Blümer, J. Schlipf, K. Held, and D. Vollhardt, Phys. Rev. B **58**, 12749 (1998).
- [58] O.K. Andersen, Phys. Rev. B **2**, 883 (1970).

Bibliography

- [59] F.M. Mueller, A.J. Freeman, J.O. Dimmock, and A.M. Furdyna, *Phys. Rev. B* **1**, 4617 (1970).
- [60] T.J. Watson-Yang, B.N. Harmon, and A.J. Freeman, *J. Magn. Magn. Mater.* **2**, 334 (1976).
- [61] A. Shabaev and D.A. Papaconstantopoulos, *Phys. Rev. B* **79**, 064107 (2009).
- [62] S.G. Das, D.D. Koelling, and F.M. Mueller, *Solid State Commun.* **12**, 89 (1973).
- [63] J.F. Janak, *Phys. Rev. B* **16**, 255 (1977).
- [64] J.R. Schrieffer, *J. Appl. Phys.* **39**, 642 (1968).
- [65] E. Stenzel and H. Winter, *J. Phys. F* **16**, 1789 (1986).
- [66] J.B. Staunton, J. Poulter, B. Ginatempo, E. Bruno, and D.D. Johnson, *Phys. Rev. B* **62**, 1075 (2000).
- [67] T. Jeong, A. Kyker, and W.E. Pickett, *Phys. Rev. B* **73**, 115106 (2006).
- [68] D.A. Tompsett, R.J. Needs, F.M. Grosche, and G.G. Lonzarich, *Phys. Rev. B* **82**, 155137 (2010).
- [69] M. Shimizu, *Rep. Prog. Phys.* **44**, 21 (1981).
- [70] O. Gunnarsson, *J. Phys. F* **6**, 587 (1976).
- [71] T. Moriya, *Spin Fluctuations in Itinerant Electron Magnetism* (Springer-Verlag, Berlin, 1985).
- [72] S. Doniach and S. Engelsberg, *Phys. Rev. Lett.* **17**, 750 (1966).
- [73] M.T. Béal-Monod, S.-K. Ma, and D.R. Fredkin, *Phys. Rev. Lett.* **20**, 929 (1968).
- [74] K.K. Murata and S. Doniach, *Phys. Rev. Lett.* **29**, 285 (1972).

Bibliography

- [75] T.V. Ramakrishnan, Phys. Rev. B **10**, 4014 (1974).
- [76] N.F. Berk and J.R. Schrieffer, Phys. Rev. Lett. **17**, 433 (1966).
- [77] T. Takezawa, H. Nagara, and N. Suzuki, Phys. Rev. B **71**, 012515 (2005); S.K. Bose, J. Phys.: Condens. Matter **20**, 045209 (2008).
- [78] G.G. Lonzarich and L. Taillefer, J. Phys. C **18**, 4339 (1985).
- [79] R.P. Smith, J. Phys.: Condens. Matter **21**, 095601 (2009).
- [80] P. Larson, I.I. Mazin, and D.J. Singh, Phys. Rev. B **69**, 064429 (2004).
- [81] D. Belitz, T.R. Kirkpatrick, and T. Vojta, Rev. Mod. Phys. **77**, 579 (2005).
- [82] The derivation of this model is given in the Appendix of Ref. [78].
- [83] N.R. Bernhoeft, S.M. Hayden, G.G. Lonzarich, D.McK. Paul, and E.J. Lindley, Phys. Rev. Lett. **62**, 657 (1989).
- [84] R. Double, S.M. Hayden, P. Dai, H.A. Mook, J.R. Thompson, and C.D. Frost, Phys. Rev. Lett. **105**, 027207 (2010).
- [85] H. Nakamura, K. Yoshimoto, M. Shiga, M. Nishi, and K. Kakurai, J. Phys.: Condens. Matter **9**, 4701 (1997).
- [86] e.g., V. Yushankhai, P. Thalmeier, and T. Takimoto, Phys. Rev. B **77**, 125126 (2008).
- [87] A. Ishigaki and T. Moriya, J. Phys. Soc. Jpn. **67**, 3924 (1998).
- [88] e.g., A.V. Ruban, S. Khemlevskiy, P. Mohn, and B. Johansson, Phys. Rev. B **75**, 054402 (2007).
- [89] H. Yamada, Phys. Rev. B **47**, 11211 (1993).
- [90] I.F. Foulkes and B.L. Gyorffy, Phys. Rev. B **15**, 1395 (1977); D. Fay and J. Appel, *ibid.* **16**, 2325 (1977); T. Jarlborg, Physica C **385**, 513 (2003).

Bibliography

- [91] P. Monthoux, D. Pines, and G.G. Lonzarich, *Nature* **450**, 1177 (2007).
- [92] P. Mohn and K. Schwarz, *J. Magn. Magn. Mater.* **104-107**, 685 (1992).
- [93] A.A. Povzner, A.G. Volkov, and A.N. Filanovich, *Sov. Phys. Solid State* **52**, 2012 (2010) [*Fiz. Tverd. Tela* **52**, 1879 (2010)].
- [94] A. Khellaf and J.J. Vuillemin, *J. Phys.: Condens. Matter* **4**, 1757 (1992); J.T. Schriempf, A.I. Schindler, and D.L. Mills, *Phys. Rev.* **187**, 959 (1969); A.B. Kaiser and S. Doniach, *Int. J. Magn.* **1**, 11 (1970); R. Jullien, M.T. Béal-Monod, and B. Coqblin, *Phys. Rev. B* **9**, 1441 (1974); A.P. Murani, *Phys. Rev. Lett.* **33**, 91 (1974).
- [95] K. Ikeda, S.K. Dhar, M. Yoshizawa, and K.A. Gschneidner, Jr., *J. Magn. Magn. Mater.* **100**, 292 (1991).
- [96] S. Misawa, *Phys. Lett. A* **32**, 153 (1970); **32**, 541 (1970).
- [97] G. Barnea, *J. Phys. F* **7**, 315 (1977).
- [98] G.M. Carneiro and C.J. Pethick, *Phys. Rev. B* **16**, 1933 (1977).
- [99] D.R. Grempel, *Phys. Rev. B* **27**, 4281 (1983).
- [100] E. Pamyatnykh, A. Poltavets, and M. Shabalin, *J. Phys.: Condens. Matter* **9**, 715 (1997).
- [101] D.L. Maslov and A.V. Chubukov, *Phys. Rev. B* **79**, 075112 (2009).
- [102] H. Yamada and K. Terao, *J. Phys.: Condens. Matter* **6**, 10805 (1994).
- [103] S. Rowley, R. Smith, M. Dean, L. Spalek, M. Sutherland, M. Saxena, P. Alireza, C. Ko, C. Liu, E. Pugh, S. Sebastian, and G. Lonzarich, *Phys. Status Solidi B* **247**, 469 (2010).
- [104] A. Aguayo, I.I. Mazin, and D.J. Singh, *Phys. Rev. Lett.* **92**, 147201 (2004).
- [105] J. Kübler, *Phys. Rev. B* **70**, 064427 (2004).

Bibliography

- [106] e.g., A. Fujita, K. Fukamichi, J.-T. Wang, and Y. Kawazoe, *Phys. Rev. B* **68**, 104431 (2003).
- [107] S. Sakai, R. Arita, and H. Aoki, *Phys. Rev. Lett.* **99**, 216402 (2007).
- [108] J.E. van Dam and O.K. Andersen, *Solid State Commun.* **14**, 645 (1974).
- [109] B. Zeller, A. Paintner, and J. Voithländer, *J. Phys.: Condens. Matter* **16**, 919 (2004).
- [110] C.J. Schinkel, F.R. de Boer, and B. de Hon, *J. Phys. F* **3**, 1463 (1973).
- [111] K.L. Liu, A.H. MacDonald, J.M. Daams, S.H. Vosko, and D.D. Koelling, *J. Magn. Magn. Mater.* **12**, 43 (1979).
- [112] S.N. Kaul, *J. Phys.: Condens. Matter* **11**, 7597 (1999).
- [113] Y. Takahashi, *J. Phys.: Condens. Matter* **13**, 6323 (2001).
- [114] A.Z. Solontsov and D. Wagner, *Phys. Rev. B* **51**, 12410 (1995).
- [115] A. Solontsov, *Int. J. Mod. Phys. B* **19**, 3631 (2005).
- [116] V.P. Antropov and A. Solontsov, *J. Appl. Phys.* **109**, 07E116 (2011).
- [117] S. Hirooka, *J. Phys.: Condens. Matter* **12**, 5669 (2000).
- [118] E. Miyai and F.J. Ohkawa, *Phys. Rev. B* **61**, 1357 (2000).
- [119] A. Ishigaki and T. Moriya, *J. Phys. Soc. Jpn.* **65**, 3402 (1996).
- [120] H. Alloul and L. Mihaly, *Phys. Rev. Lett.* **48**, 1420 (1982).
- [121] K. Yoshimura, M. Mekata, M. Takigawa, Y. Takahashi, and H. Yasuoka, *Phys. Rev. B* **37**, 3593 (1988).
- [122] K. Yoshimura, T. Imai, T. Kiyama, K.R. Thurber, A.W. Hunt, and K. Kosuge, *Phys. Rev. Lett.* **83**, 4397 (1999).

Bibliography

- [123] M. Corti, F. Carbone, M. Filibian, Th. Jarlborg, A.A. Nugroho, and P. Carretta, *Phys. Rev. B* **75**, 115111 (2007).
- [124] B. Chen, H. Ohta, C. Michioka, Y. Itoh, and K. Yoshimura, *Phys. Rev. B* **81**, 134416 (2010).
- [125] M. Majumder, K. Ghoshray, A. Goshray, B. Bandyopadhyay, and M. Ghosh, *Phys. Rev. B* **82**, 054422 (2010)
- [126] e.g., B. Nowak, O. Żogał, A. Pietraszko, R.E. Baumbach, M.B. Maple, and Z. Henkie, *Phys. Rev. B* **79**, 214411 (2009); C. Bourbonnais, P. Wzietek, F. Creuzet, D. Jérôme, P. Batail, and K. Bechgaard, *Phys. Rev. Lett.* **62**, 1532 (1989).
- [127] e.g., C.-S. Lue and J.H. Ross, Jr., *Phys. Rev. B* **60**, 8533 (1999).
- [128] F.M. Muller, R. Gersdorf, and L.W. Roeland, *Phys. Lett. A* **31**, 424 (1970).
- [129] G.R. Stewart and B.L. Brandt, *Phys. Rev. B* **28**, 2266 (1983).
- [130] W. Joss, L.N. Hall, G.W. Crabtree, and J.J. Vuillemin, *Phys. Rev. B* **30**, 5637 (1984).
- [131] L.W. Roeland, J.C. Wolfrat, D.K. Mak, and M. Springford, *J. Phys. F* **12**, L267 (1982).
- [132] T. Jarlborg and A.J. Freeman, *Phys. Rev. B* **23**, 3577 (1981).
- [133] A. Hjelm, *Int. J. Mod. Phys. B* **7**, 275 (1993).
- [134] E. Hüger and K. Osuch, *Eur. Phys. J. B* **44**, 145 (2005).
- [135] H. Chen, N.E. Brener, and J. Callaway, *Phys. Rev. B* **40**, 1443 (1989).
- [136] V.L. Moruzzi and P.M. Marcus, *Phys. Rev. B* **39**, 471 (1989).
- [137] L. Fritsche, J. Noffke, and H. Eckardt, *J. Phys. F* **17**, 943 (1987).
- [138] S.C. Hong and J.I. Lee, *J. Korean Phys. Soc.* **52**, 1099 (2008).

Bibliography

- [139] M.B. Brodsky and A.J. Freeman, *Phys. Rev. Lett.* **45**, 133 (1980).
- [140] T. Jarlborg and A.J. Freeman, *J. Appl. Phys.* **53**, 8041 (1982).
- [141] Y. Kuk, L.C. Feldman, and P.J. Silverman, *Phys. Rev. Lett.* **50**, 511 (1983).
- [142] S.C. Hong, C.L. Fu, and A.J. Freeman, *J. Appl. Phys.* **63**, 3655 (1988).
- [143] cf. W. Gerhardt, F. Razavi, J.S. Schilling, D. Hüser, and J.A. Mydosh, *Phys. Rev. B* **24**, 6744 (1981).
- [144] D.J. Lam and K.M. Myles, *J. Phys. Soc. Jpn.* **21**, 1503 (1966).
- [145] T. Asada and K. Terakura, *J. Phys. Soc. Jpn.* **47**, 1495 (1979).
- [146] O. Loebich, Jr. and Ch.J. Raub, *J. Less-Common. Met.* **55**, 67 (1977).
- [147] T. Auerswald, H. Claus, and O. Meyer, *Phys. Rev. B* **43**, 14232 (1991).
- [148] R. Doclo, S. Foner, and A. Narath, *J. Appl. Phys.* **40**, 1206 (1969).
- [149] W. Sängler and J. Voitländer, *Z. Phys. B* **44**, 283 (1981).
- [150] R.J. Miller, T.O. Brun, and C.B. Satterthwaite, *Phys. Rev. B* **18**, 5054 (1978).
- [151] M.Mahnig and L.E. Toth, *Phys. Lett. A* **32**, 319 (1970); H. Husemann and H. Brodowsky, *Z. Naturforsch. A* **23**, 1693 (1968).
- [152] J. Crangle and W.R. Scott, *J. Appl. Phys.* **36**, 921 (1965); G.J. Nieuwenhuys, *Adv. Phys.* **24**, 515 (1975).
- [153] T. Herrmannsdörfer, S. Rehmann, W. Wendler, and F. Pobell, *J. Low Temp. Phys.* **104**, 49 (1996).
- [154] G.G. Low and T.M. Holden, *Proc. Phys. Soc. London* **89**, 119 (1966); B.H. Verbeek, G.J. Nieuwenhuys, J.A. Mydosh, C. van Dijk, and B.D. Rainford, *Phys. Rev. B* **22**, 5426 (1980).

Bibliography

- [155] S. Polesya, S. Mankovsky, O. Sipr, W. Meindl, C. Strunk, and H. Ebert, *Phys. Rev. B* **82**, 214409 (2010).
- [156] e.g., N. Kioussis and J.W. Garland, *Phys. Rev. Lett.* **67**, 366 (1991).
- [157] J.D. Jackson, *Classical Electrodynamics*, 3rd ed. (Wiley, New York, 1999).
- [158] e.g., A. Zangwill, *Physics at Surfaces* (Cambridge University Press, Cambridge, 1988).
- [159] e.g., J. Lu, P.L. Kuhns, M.J.R. Hoch, W.G. Moulton, and A.P. Reyes, *Phys. Rev. B* **72**, 054401 (2005); R.I. Salikhov, I.A. Garifullin, N.N. Garif'yanov, L.R. Tagirov, K. Theis-Bröhl, K. Westerholt, and H. Zabel, *Phys. Rev. Lett.* **102**, 087003 (2009).
- [160] H.J. Jänsch, P. Gerhard, and M. Koch, *Proc. Nat. Acad. Sci. USA* **101**, 13715 (2004); A. Bifone, T. Pietrass, J. Kritzenberger, A. Pines, and B.F. Chmelka, *Phys. Rev. Lett.* **74**, 3277 (1995).
- [161] E.B. Karlsson, *Solid State Phenomena As Seen by Muons, Protons, and Excited Nuclei* (Clarendon, Oxford, 1995).
- [162] A. Schenck, *Muon Spin Rotation Spectroscopy: Principles and Applications in Solid State Physics* (Adam Hilger, Bristol, 1985).
- [163] R.F. Kiefl, G.D. Morris, P. Amaudruz, R. Baartman, J. Behr, J.H. Brewer, J. Chakhalian, S. Daviel, J. Doornbos, S. Dunsiger, S.R. Kreitzman, T. Kuo, C.D.P. Levy, R. Miller, M. Olivo, R. Poutissou, G.W. Wight, and A. Zelenski, *Physica B* **289-290**, 640 (2000).
- [164] e.g., E. Morenzoni, T. Prokscha, A. Suter, H. Luetkens, and R. Khasanov, *J. Phys.: Condens. Matter* **16**, S4583 (2004).
- [165] Z. Salman, E.P. Reynard, W.A. MacFarlane, K.H. Chow, J. Chakhalian, S. Kreitzman, S. Daviel, C.D.P. Levy, R. Poutissou, and R.F. Kiefl, *Phys. Rev. B* **70**, 104404 (2004).

- [166] R.C. Haskell and L. Madansky, *Phys. Rev. C* **7**, 1277 (1973).
- [167] D. Borremans, D.L. Balabanski, K. Blaum,, W. Geithner, S. Gheysen, P. Himpe, M. Kowalska, J. Lassen, P. Lievens, S. Mallion, R. Neugart, G. Neyens, N. Vermeulen, and D. Yordanov, *Phys. Rev. C* **72**, 044309 (2005).
- [168] C.D. Gelatt, Jr., A.R. Williams, and V.L. Moruzzi, *Phys. Rev. B* **27**, 2005 (1983).
- [169] e.g., R. Böhmer, K.R. Jeffrey, and M. Vogel, *Prog. Nucl. Magn. Reson. Spectrosc.* **50**, 87 (2007).
- [170] H. Akai, M. Akai, S. Blügel, B. Drittler, H. Ebert, K. Terakura, R. Zeller, and P.H. Dederichs, *Prog. Theor. Phys. Suppl.* **101**, 11 (1990).
- [171] H. Fukuda and H. Akai, *J. Phys. Soc. Jpn.* **70**, 2019 (2001).
- [172] Y. Nojiri, K. Ishiga, T. Onishi, M. Sasaki, F. Ohsumi, T. Kawa, M. Mihara, M. Fukuda, K. Matsuta, and T. Minamisono, *Hyperfine Interact.* **120-121**, 415 (1999).
- [173] R. Pirlot, M. Cyamukungu, L. Grenancs, J. Lehmann, R. Coussement, G. S'heeren, and K. Tompa, *Hyperfine Interact.* **80**, 989 (1993).
- [174] S.J. Blundell and S.F.J. Cox, *J. Phys.: Condens. Matter* **13**, 2163 (2001).
- [175] The original reference is: J.H. van Vleck, *Phys. Rev.* **74**, 1168 (1948).
- [176] O. Hartmann, *Phys. Rev. Lett.* **39**, 832 (1977).
- [177] B. Ittermann, G. Welker, F. Kroll, F. Mai, K. Marbach, and D. Peters, *Phys. Rev. B* **59**, 2700 (1999).
- [178] H.-J. Stöckmann, E. Jäger, G. Sulzer, B. Ittermann, H. Ackermann, E. Diehl, R. Dippel, B. Fischer, H.-P. Frank, and W. Seelinger, *Hyperfine Interact.* **49**, 235 (1989).

- [179] M. Füllgrabe, B. Ittermann, H.-J. Stöckmann, F. Kroll, D. Peters, and H. Ackermann, *Phys. Rev. B* **64**, 224302 (2001).
- [180] T.K. McNab and R.E. McDonald, *Phys. Rev. B* **13**, 34 (1976).
- [181] T. Minamisono, Y. Nojiri, and K. Matsuta, *Phys. Lett. A* **94**, 312 (1983).
- [182] E. Jäger, B. Ittermann, H.-J. Stöckmann, K. Bürkmann, B. Fischer, H.-P. Frank, G. Sulzer, H. Ackermann, and P. Heitjans, *Phys. Lett. A* **123**, 39 (1987).
- [183] E. Jäger, K. Bürkmann, B. Fischer, H.-P. Frank, B. Ittermann, G. Sulzer, H.-J. Stöckmann, and H. Ackermann, *Z. Phys. B* **86**, 389 (1992).
- [184] G.D. Morris, W.A. MacFarlane, K.H. Chow, Z. Salman, D.J. Arseneau, S. Daviel, A. Hatakeyama, S.R. Kreitzman, C.D.P. Levy, R. Poutissou, R.H. Heffner, J.E. Elenewski, L.H. Greene, and R.F. Kiefl, *Phys. Rev. Lett.* **93**, 157601 (2004).
- [185] Z. Salman, A.I. Mansour, K.H. Chow, M. Beaudoin, I. Fan, J. Jung, T.A. Keeler, R.F. Kiefl, C.D.P. Levy, R.C. Ma, G.D. Morris, T.J. Parolin, D. Wang, and W.A. MacFarlane, *Phys. Rev. B* **75**, 073405 (2007).
- [186] D. Wang, Z. Salman, K.H. Chow, I. Fan, M.D. Hossain, T.A. Keeler, R.F. Kiefl, C.D.P. Levy, A.I. Mansour, G.D. Morris, M.R. Pearson, T.J. Parolin, H. Saadaoui, M. Smadella, Q. Song, and W.A. MacFarlane, *Physica B* **404**, 920 (2009).
- [187] M.D. Hossain, H. Saadaoui, T.J. Parolin, Q. Song, D. Wang, M. Smadella, K.H. Chow, M. Egilmez, I. Fan, R.F. Kiefl, S.R. Kreitzman, C.D.P. Levy, G.D. Morris, M.R. Pearson, Z. Salman, and W.A. MacFarlane, *Physica B* **404**, 914 (2009).
- [188] P. Ehrhart and H. Schultz, in *Atomic Defects in Metals*, edited by H. Ullmaier, Landolt-Börstein, New Series, Group III, Vol. 25 (Springer-Verlag, Heidelberg, 1991), Chap. 2.

Bibliography

- [189] I. Koenig, D. Fick, S. Kossionides, P. Egelhof, K.-H. Möbius, and E. Steffens, *Z. Phys. A* **318**, 135 (1984).
- [190] T.A. Keeler, Z. Salman, K.H. Chow, B. Heinrich, M.D. Hossain, B. Kardasz, R.F. Kiefl, S.R. Kreitzman, C.D.P. Levy, W.A. MacFarlane, O. Mosendz, T.J. Parolin, M.R. Pearson, and D. Wang, *Phys. Rev. B* **77**, 144429 (2008).
- [191] M. Xu, M.D. Hossain, H. Saadaoui, T.J. Parolin, K.H. Chow, T.A. Keeler, R.F. Kiefl, G.D. Morris, Z. Salman, D. Wang, Q. Song, and W.A. MacFarlane, *J. Magn. Reson.* **191**, 47 (2008).
- [192] H. Saadaoui, W.A. MacFarlane, Z. Salman, G.D. Morris, Q. Song, K.H. Chow, M.D. Hossain, C.D.P. Levy, A.I. Mansour, T.J. Parolin, M.R. Pearson, M. Smadella, D. Wang, and R.F. Kiefl, *Phys. Rev. B* **80**, 224503 (2009).
- [193] e.g., S.C. Hong, J.I. Lee, and R. Wu, *Phys. Rev. B* **75**, 172402 (2007).
- [194] e.g., Y. Oba, T. Sato, and T. Shinohara, *Phys. Rev. B* **78**, 224417 (2008).
- [195] K. Tompa, R. Pirlot, L. Grenacs, and J. Lehmann, *Phys. Status Solidi B* **153**, 721 (1989).
- [196] M. Mihara, K. Matsuta, S. Kumashiro, M. Fukuda, S. Kosakai, Y. Umemoto, M. Yoshikawa, R. Matsumiya, D. Nishimura, J. Komurasaki, D. Ishikawa, M. Ogura, H. Akai, and T. Minamisono, *Hyperfine Interact.* **178**, 73 (2007); M. Mihara, S. Kumashiro, K. Matsuta, Y. Nakashima, H. Fujiwara, Y.N. Zheng, M. Ogura, H. Akai, M. Fukuda, and T. Minamisono, *ibid.* **158**, 361 (2004).
- [197] J. Imazato, Y.J. Uemura, N. Nishida, R.S. Hayano, K. Nagamine, and T. Yamazaki, *J. Phys. Soc. Jpn.* **48**, 1153 (1980).
- [198] F.N. Gygax, A. Hintermann, W. Rüegg, A. Schenck, and W. Studer, *Solid State Commun.* **38**, 1245 (1981).

Bibliography

- [199] J. Brossel, A. Kastler, and J. Winter, *J. Phys. Radium* **13**, 668 (1952).
- [200] W.B. Hawkins and R.H. Dicke, *Phys. Rev.* **91**, 1008 (1953).
- [201] C.D.P. Levy, A. Hatakeyama, Y. Hirayama, R.F. Kiefl, R. Baartman, J.A. Behr, H. Izumi, D. Melconian, G.D. Morris, R. Nussbaumer, M. Olivo, M. Pearson, R. Poutissou, and G.W. Wight, *Nucl. Instrum. Methods B* **204**, 689 (2003).
- [202] W. Widdra, M. Detje, H.-D. Ebinger, H.J. Jänsch, W. Preyss, H. Reich, R. Veith, D. Fick, M. Röckelein, and H.-G. Völk, *Rev. Sci. Instrum.* **66**, 2465 (1995).
- [203] Yu.G. Abov, A.D. Gulko, and F.S. Dzheparov, *Sov. Phys. At. Nucl.* **69**, 1701 (2006) [*Yad. Fiz.* **69**, 1737 (2006)].
- [204] W.A. MacFarlane, G.D. Morris, K.H. Chow, R.A. Baartman, S. Daviel, S.R. Dunsiger, A. Hatakeyama, S.R. Krietzman, C.D.P. Levy, R.I. Miller, K.M. Nichol, R. Poutissou, E. Dumont, L.H. Greene, and R.F. Kiefl, *Physica B* **326**, 209 (2003).
- [205] C.P. Poole, Jr. and H.A. Farach, *Theory of Magnetic Resonance*, 2nd ed. (Wiley, New York, 1987).
- [206] Z. Salman, R.F. Kiefl, K.H. Chow, M.D. Hossain, T.A. Keeler, S.R. Krietzman, C.D.P. Levy, R.I. Miller, T.J. Parolin, M.R. Pearson, H. Saadaoui, J.D. Schultz, M. Smadella, D. Wang, and W.A. MacFarlane, *Phys. Rev. Lett.* **96**, 147601 (2006).
- [207] S.R. Krietzman, *Hyperfine Interact.* **65**, 1055 (1990).
- [208] S. Kazama and Y. Fukai, *J. Less-Common Met.* **53**, 25 (1977).
- [209] T.J. Parolin, J. Shi, Z. Salman, K.H. Chow, P. Dosanjh, H. Saadaoui, Q. Song, M.D. Hossain, R.F. Kiefl, C.D.P. Levy, M.R. Pearson, and W.A. MacFarlane, *Phys. Rev. B* **80**, 174109 (2009).
- [210] T. Wagner, G. Richter, and M. Rühle, *J. Appl. Phys.* **89**, 2606 (2001).

- [211] W.A. MacFarlane, G.D. Morris, T.R. Beals, K.H. Chow, R.A. Baartman, S. Daviel, S.R. Dunsiger, A. Hatakeyama, S.R. Kreitzman, C.D.P. Levy, R.I. Miller, K.M. Nichol, R. Poutissou, and R.F. Kiefl, *Physica B* **326**, 213 (2003).
- [212] T.J. Parolin, Z. Salman, K.H. Chow, Q. Song, J. Valiani, H. Saadaoui, A. O'Halloran, M.D. Hossain, T.A. Keeler, R.F. Kiefl, S.R. Kreitzman, C.D.P. Levy, R.I. Miller, G.D. Morris, M.R. Pearson, M. Smadella, D. Wang, M. Xu, and W.A. MacFarlane, *Phys. Rev. B* **77**, 214107 (2008).
- [213] e.g., A.F. McDowell, *J. Magn. Reson. Ser. A* **113**, 242 (1995), and references therein.
- [214] F. Ohsumi, K. Matsuta, M. Mihara, T. Onishi, T. Miyake, M. Sasaki, K. Sato, C. Ha, A. Morishita, T. Fujio, Y. Kobayashi, M. Fukuda, and T. Minamisono, *Hyperfine Interact.* **120-121**, 419 (1999).
- [215] T.J. Parolin, Z. Salman, J. Chakhalian, D. Wang, T.A. Keeler, M.D. Hossain, R.F. Kiefl, K.H. Chow, G.D. Morris, R.I. Miller, and W.A. MacFarlane, *Physica B* **374-375**, 419 (2006).
- [216] T.J. Parolin, Z. Salman, J. Chakhalian, Q. Song, K.H. Chow, M.D. Hossain, T.A. Keeler, R.F. Kiefl, S.R. Kreitzman, C.D.P. Levy, R.I. Miller, G.D. Morris, M.R. Pearson, H. Saadaoui, D. Wang, and W.A. MacFarlane, *Phys. Rev. Lett.* **98**, 047601 (2007).
- [217] A. Narath and H.T. Weaver, *Phys. Rev. B* **3**, 616 (1971).
- [218] H.L.M. Bakker, M.J.C. de Jong, P.M. Oppeneer, R. Griessen, A. Lodder, R. Vis, and H. Brodowsky, *J. Phys. F* **16**, 707 (1986).
- [219] P.G. Averbuch and P.J. Ségransan, *Phys. Rev. B* **4**, 2067 (1971).
- [220] E. Fawcett and V. Pluzhnikov, *Physica* **119B**, 161 (1983).
- [221] e.g., M. Doerr, S. Schönecker, A. Haase, E. Kampert, J.A.A.J. Parenboom, M. Richter, M. Rotter, M.S. Kim, and M. Loewenhaupt, *J. Low Temp. Phys.* **159**, 20 (2010).

Bibliography

- [222] e.g., E. Fawcett, J.P. Maita, E. Bucher, and J.H. Wernick, *Phys. Rev. B* **2**, 3639 (1970).
- [223] A.B. Kaiser and P. Fulde, *Phys. Rev. B* **37**, 5357 (1988).
- [224] A.B. Kaiser, A.M. Oleś, and G. Stollhoff, *Phys. Scr.* **37**, 935 (1988).
- [225] A.S. Panfilov and I.V. Svechkarev, *Int. J. Mod. Phys. B* **7**, 699 (1993).
- [226] A.J. Millis, *Phys. Rev. B* **48**, 7183 (1993).
- [227] D.A. Sokolov, M.C. Aronson, W. Gannon, and Z. Fisk, *Phys. Rev. Lett.* **96**, 116404 (2006).
- [228] B. Chen, C. Michioka, Y. Itoh, and K. Yoshimura, *J. Phys. Soc. Jpn.* **77**, 103708 (2008).
- [229] J. Yang, B. Chen, H. Ohta, C. Michioka, K. Yoshimura, H. Wang, and M. Fang, *Phys. Rev. B* **83**, 134433 (2011).
- [230] A.J. Millis, D.K. Morr, and J. Schmalian, *Phys. Rev. Lett.* **87**, 167202 (2001).
- [231] e.g., P.-G. de Gennes, *Phys. Rev.* **118**, 141 (1960); V.G. Storchak, J.H. Brewer, R.L. Lichti, T.A. Lograsso, and D.L. Schlagel, *Phys. Rev. B* **83**, 140404(R) (2011).
- [232] P. Lederer, *Solid State Commun.* **7**, 209 (1969).
- [233] A.I. Mansour, G.D. Morris, Z. Salman, K.H. Chow, T. Dunlop, J. Jung, I. Fan, W.A. MacFarlane, R.F. Kiefl, T.J. Parolin, H. Saadaoui, D. Wang, M.D. Hossain, Q. Song, M. Smadella, O. Mosendz, B. Kardasz, and B. Heinrich, *Physica B* **401-402**, 662 (2007).
- [234] e.g., A.J. Francis and P.A. Salvador, *J. Mater. Res.* **22**, 89 (2007).
- [235] F. Wilhelm, M. Angelakeris, N. Jaouen, P. Pouloupoulos, E.Th. Papaioannou, Ch. Mueller, P. Fumagalli, A. Rogalev, and N.K. Flevaris, *Phys. Rev. B* **69**, 220404(R) (2004); T. Emoto, N. Hosoi, and T. Shinjo, *J. Magn. Magn. Mater.* **189**, 136 (1998).

- [236] e.g., A. Yaouanc, P. Dalmas de Réotier, P.C.M. Gubbens, S. Sakarya, G. Lapertot, A.D. Hillier, and P.J.C. King, *J. Phys.: Condens. Matter* **17**, L129 (2005).
- [237] U. Gradmann and R. Bergholz, *Phys. Rev. Lett.* **52**, 771 (1984).
- [238] J. Dorantes-Dávila, H. Dreyssé, and G.M. Pastor, *Phys. Rev. Lett.* **91**, 197206 (2003); P.F. Carcia, A.D. Meinhaldt, and A. Suna, *Appl. Phys. Lett.* **47**, 178 (1985).
- [239] E.E. Fullerton, D. Stoeffler, K. Ounadjela, B. Heinrich, Z. Celinski, and J.A.C. Bland, *Phys. Rev. B* **51**, 6364 (1995); Z. Celinski, B. Heinrich, J.F. Cochran, W.B. Muir, A.S. Arrott, and J. Kirschner, *Phys. Rev. Lett.* **65**, 1156 (1990).
- [240] L. Cheng, Z. Altounian, D.H. Ryan, J.O. Ström-Olsen, M. Sutton, and Z. Tun, *Phys. Rev. B* **69**, 144403 (2004).
- [241] H.H. Bertschat, H.-H. Blaschek, H. Granzer, K. Potzger, S. Seeger, W.-D. Zeitz, H. Niehus, A. Burchard, D. Forkel-Wirth, and ISOLDE Collaboration, *Phys. Rev. Lett.* **80**, 2721 (1998).
- [242] T. Manago, T. Ono, H. Miyajima, K. Kawaguchi, and M. Sohma, *J. Phys. Soc. Jpn.* **68**, 3677 (1999).
- [243] Y.N. Kim, E.K. Lee, Y.B. Lee, H. Shim, N.H. Hur, and W.S. Kim, *J. Am. Chem. Soc.* **126**, 8672 (2004).
- [244] e.g., D. Katayama, A. Sumiyama, and Y. Oda, *Phys. Rev. B* **68**, 132502 (2003).
- [245] A. Potenza, M.S. Gabureac, and C.H. Marrows, *Phys. Rev. B* **76**, 014534 (2007); *J. Appl. Phys.* **103**, 07C703 (2008).
- [246] e.g., F. Silly and M.R. Castell, *Phys. Rev. Lett.* **94**, 046103 (2005); F. Silly, A.C. Powell, M.G. Martin, and M.R. Castell, *Phys. Rev. B* **72**, 165403 (2005).

Bibliography

- [247] T.J. Parolin, Z. Salman, J. Chakhalian, Q. Song, K.H. Chow, G.D. Morris, M. Egilmez, I. Fan, M.D. Hossain, T.A. Keeler, R.F. Kiefl, S.R. Kreitzman, C.D.P. levy, A.I. Mansour, R.I. Miller, M.R. Pearson, H. Saadaoui, M. Smadella, D. Wang, M. Xu, and W.A. MacFarlane, *Physica B* **404**, 917 (2009).
- [248] G. Friedlander, J.W. Kennedy, E.S. Macias, and J.M. Miller, *Nuclear and Radiochemistry*, 3rd ed. (Wiley, New York, 1981).
- [249] K. Heyde, *Basic Ideas and Concepts in Nuclear Physics*, 3rd ed. (Institute of Physics, Bristol, 2004), Chap. 5.
- [250] E. Segrè, *Nuclei and Particles*, 2nd ed. (Benjamin/Cummings, Reading, MA, 1977).
- [251] H.J. Lipkin, *Beta Decay for Pedestrians* (Dover, Mineola, NY, 2004), Chap. 2.
- [252] S.G. Crane, S.J. Brice, A. Goldschmidt, R. Gukert, A. Hime, J.J. Kitten, D.J. Vieira, and X. Zhao, *Phys. Rev. Lett.* **86**, 2967 (2001).
- [253] L.M. Chirovsky, W.P. Lee, A.M. Sabbas, J.L. Groves, and C.S. Wu, *Phys. Lett. B* **94**, 127 (1980).
- [254] J. Sromicki, M. Allet, K. Bodek, W. Hajdas, J. Lang, R. Müller, S. Navert, O. Naviliat-Cuncic, J. Zejma, and W. Haeberli, *Phys. Rev. C* **53**, 932 (1996).
- [255] N.E. Holden, in *CRC Handbook of Chemistry and Physics*, 78th ed., edited by D.R. Lide (CRC Press, Boca Raton, 1997), Sec. 11.
- [256] P.D. Townsend, J.C. Kelly, and N.E.W. Hartley, *Ion Implantation, Sputtering and their Applications* (Academic, London, 1976).
- [257] E. Rauhala, in *Handbook of Modern Ion Beam Materials Analysis*, edited by J.R. Tesmer and M. Nastasi (Materials Research Society, Pittsburgh, 1995), Chap. 2.

Bibliography

- [258] e.g., M. Ohring, *The Materials Science of Thin Films* (Academic, San Diego, 1992), pp. 609–23.
- [259] e.g., A. Meldrum, R.F. Haglund, Jr., L.A. Boatner, and C.W. White, *Adv. Mater.* **13**, 1431 (2001).
- [260] e.g., J. Fassbender and J. McCord, *J. Magn. Magn. Mater.* **320**, 579 (2008).
- [261] J.A. Leavitt, L.C. McIntyre, Jr., and M.R. Weller, in *Handbook of Modern Ion Beam Materials Analysis*, edited by J.R. Tesmer and M. Nastasi (Materials Research Society, Pittsburgh, 1995), Chap. 4.
- [262] e.g., M. Hohenstein, A. Seeger, and W. Sigle, *J. Nucl. Mater.* **169**, 33 (1989).
- [263] J. Gittus, *Irradiation Effects in Crystalline Solids* (Applied Science Publishers, Essex, 1978).
- [264] J.F. Ziegler, J.P. Biersack, and U. Littmark, *The Stopping and Range of Ions in Solids* (Pergamon, New York, 1985).
- [265] W. Eckstein, *Computer Simulation of Ion-Solid Interactions* (Springer-Verlag, Berlin, 1991).

Appendix A

Basics of Beta Decay

A.1 General concepts

The use of beta-radioactive nuclei underlies the technique of β -NMR. Thus, a review of the fundamentals of the beta decay process[248] is given here.

In β -decay the parent nucleus A_ZX is transformed into a daughter nucleus of ${}^A_{Z+1}X$ or ${}^A_{Z-1}X$; thus, the total mass number A remains constant, but the atomic number Z changes. Beta decay is subdivided into three types of processes. In two of these a β -particle, or electron, is emitted from the *nucleus* during the decay; in the third type, an *extranuclear* or orbital electron is captured by the nucleus. (i) In β^- -decay e^- emission accompanies the transformation of a neutron to a proton, and ($Z \rightarrow Z + 1$); (ii) in β^+ -decay, positrons e^+ are emitted when the opposite occurs, a proton transforms to a neutron and ($Z \rightarrow Z - 1$); (iii) in electron capture[249] EC, an electron from a bound atomic state (K,L,M,...) is captured by a proton, a neutron is formed, and again ($Z \rightarrow Z - 1$). EC leaves the final atom in an excited state and secondary emission of X-rays or Auger electrons is observed, the latter are *not* considered β -particles. It is a decay of type (i) that is relevant for β -NMR studies of this thesis.

Historically, β -decay was quite puzzling for several reasons. First, in contrast to alpha decay where the α -particles are emitted in discrete energy groups, the β -particles exhibit a continuous distribution of energy, extending from zero to an upper maximum E_0 ; see Fig. A.1. If E_0 corresponds to the energy difference between the initial (parent) nucleus and final (daughter) nucleus states, then the continuous nature of the β -particle kinetic energy spectrum seemed to violate the law of conservation of energy. Additionally, β -decay seemed to violate the principle of conservation of angular momen-

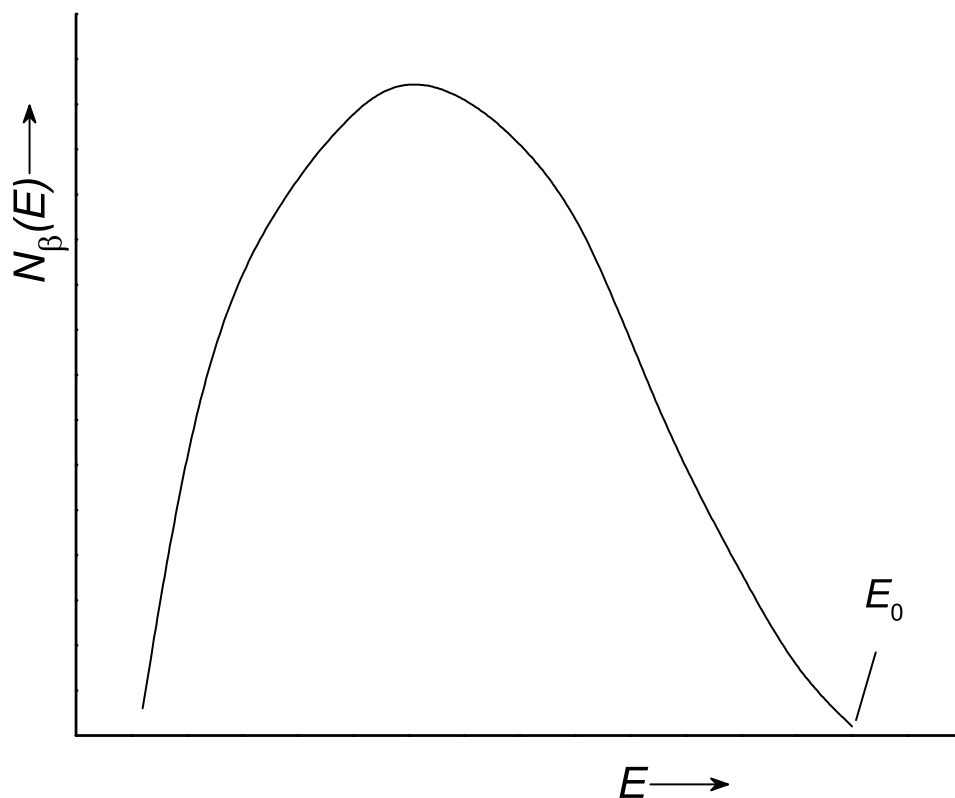


Figure A.1: Example distribution of electron energies in β -decay. E_0 is the maximum energy difference between parent and daughter nuclei; for known β -emitters this ranges between a few keV to about 15 MeV[248].

tum and the rule of statistics for composite systems[250]. For instance, consider the β -decay of tritium: ${}^3\text{H} \rightarrow {}^3\text{He} + e^-$. The angular momentum of ${}^3\text{H}$ is $\frac{1}{2}$, while for the $({}^3\text{He} + e^-)$ system it is either 0 or 1, i.e., ${}^3\text{H}$ is a fermion, while the decay products form a system that is a boson[250].

A solution to these difficulties that does not require abandoning the conservation laws in β -decay was put forth by Pauli, who in 1930 postulated that an additional, undetected particle is emitted in each β -disintegration. This particle is known as the neutrino ν . The electron and the neutrino belong to the class of elementary particles called leptons. Energy is conserved in the β -decay process as the neutrino carries off an amount of energy equal

to the difference between the energy of a given β -electron and E_0 (except in EC where the emitted neutrino is monoenergetic)[250]. Additionally, to preserve charge conservation the neutrino must have a charge of 0 (and thus an extremely small magnetic moment, if any), and the balance of angular momentum requires that the neutrino be a spin- $\frac{1}{2}$ fermion[250].

The neutrino thus has an associated antiparticle— the antineutrino $\bar{\nu}$ — with the same spin, charge, and mass as ν [250]. By definition $\bar{\nu}_e$ is the second particle emitted in β^- -decay,¹² and ν_e is the particle that accompanies β^+ -decay and EC[250]. Thus, the elementary processes (i) and (ii) above are written as:

$$n \rightarrow p + e^- + \bar{\nu}_e \quad (\text{A.1})$$

$$p \rightarrow n + e^+ + \nu_e \quad (\text{A.2})$$

Free neutrons do decay as shown, and while the free proton is stable, it can undergo decay inside a nucleus that as a whole can supply the necessary energy.

The neutrino is a very elusive particle that is hard to detect, but one way to study the neutrino is to investigate its interaction with other matter such as in inverse β -decay processes[249, 250]. For instance, the reaction $\bar{\nu}_e + p \rightarrow n + e^+$ was studied by using antineutrinos produced in a nuclear reactor to bombard a substance containing hydrogen (like H₂O). The emitted positrons are immediately annihilated and the characteristic annihilation radiation is observed. A small amount of Cd salt was added to the water, and the emitted neutron is captured by the Cd with the subsequent emission of characteristic gamma rays $\sim 10^{-5}$ s after the e^+ -annihilation radiation is detected. This sequence is specific enough to be unambiguous and provided experimental evidence (in 1953) for the existence of the neutrino[249, 250]. A second particularly important example is the study of the inverse EC decay of ³⁷Ar: $^{37}\text{Ar} + e^- \rightarrow ^{37}\text{Cl} + \nu_e$. By bombarding ³⁷Cl with ν_e or $\bar{\nu}_e$

¹²The subscript e has been added to indicate that these neutrinos and antineutrinos are associated with β -decay (the electron); there are also neutrinos and antineutrinos associated with the decay of the muon and the tau meson that are not identical to those emitted in β -decay[248, 249, 250]. This leads to the concept of neutrino “flavour.”

produced in a reactor ^{37}Ar should be formed; however, the use of $\bar{\nu}_e$ gave a null result, demonstrating ν_e and $\bar{\nu}_e$ are two different particles[249, 250]. A distinction between the neutrino and antineutrino is on the basis of their *helicities*. The direction of spin of the $\bar{\nu}_e$ is parallel to its momentum, while the direction of spin of the ν_e is antiparallel to its momentum[250]. Thus, the neutrino helicity is -1, it is a left-handed particle, while the antineutrino has helicity of +1 and is a right-handed particle[250].

Lastly, the question of the rest mass of the neutrino m_ν is of fundamental significance to nuclear and astrophysics problems, more so than for beta decay. Experimentally, precise measurements of m_ν are very difficult, and only upper and lower limits are determined[249]. For many years, m_ν was taken to be exactly zero[250]; however, it is now believed that m_ν is different from zero, but still very tiny, e.g., $< 20 \text{ eV}/c^2$ [249], or 0.00004 times the electron rest mass. The notion of a non-zero neutrino rest mass originated from experiments designed to measure the flux of neutrinos originating from the sun's nuclear reactions that strike earth. The results of these measurements (starting with R. Davis' pioneering Homestake Mine experiment and later supplemented/augmented by data from (Super)Kamiokande and the Sudbury Neutrino Observatory) supported theories proposed as early as 1969 that the (anti)neutrino can undergo oscillations in flavour[249], e.g., $\nu_\mu \rightarrow \nu_e$ (see footnote 12). For this to be the case the neutrino can not be truly relativistic— it must have a finite rest mass. The value of m_ν has important consequences for profound questions in cosmology, like (anti)neutrino production during the Big Bang and other tests of models of the origin of the universe[249].

A.2 Fermi's theory of beta decay

Fermi formulated a quantitative theory of β -decay that includes Pauli's (then hypothetical) neutrino in 1934[248]. In 1957 experimental observations (see following Section) required Fermi's theory be modified[249], but many of his results remained valid[250] and the theory provides the foundation for the understanding of β -decay. The fundamental interaction that governs the

A.2. Fermi's theory of beta decay

beta decay process is the weak interaction. By 1933 the quantum theory of radiation was well established, so Fermi formulated his β -decay theory by analogy with the electromagnetic interaction[248, 249, 250]. Just as photons are created at the time of emission as a nucleus or molecule passes from an excited state to the ground state, β^\pm -particles and (anti)neutrinos are created as the nucleus decays. Fermi's theory provides a dynamical description of this process explaining the shape of beta spectra (e.g., Fig. A.1), the relation between E_0 and the mean lifetime of the nucleus, and allows β -decay transitions to be classified on the basis of selection rules[250].

Using time-dependent perturbation theory, the starting point for the β -decay transition rate λ is Fermi's golden rule

$$\lambda = \frac{2\pi}{\hbar} |\mathcal{H}_{fi}|^2 \rho, \quad (\text{A.3})$$

where \mathcal{H}_{fi} is the weak interaction Hamiltonian matrix element between the final and initial states, and $\rho = dN/dE_0$ is the density of the final states, i.e., the number of final states per unit of total decay energy (the "phase space" term). Here, λ represents the total probability per unit time that a β -particle is emitted. A detailed mathematical treatment can be found in Ref. [250]. The final expression is

$$\lambda = \frac{g^2 m_e^5 c^4}{2\pi^3 \hbar^7} |M_{fi}|^2 f(Z, \epsilon_0), \quad (\text{A.4})$$

where g is a constant, M_{fi} is a number that stems from the overlap integral over the parent and daughter nuclear wavefunctions. The function $f(Z, \epsilon_0)$, where $\epsilon_0 = E_0/m_e c^2$, is known as the Fermi function. It gives a correction for the Coulomb interaction between the nucleons of the daughter nuclei and the emitted electron. It gives rise to distortions of the β spectrum from an otherwise "bell-shape"[249] mostly near the maximum energy region (e.g., Fig. A.1).

By defining a mean lifetime for the decaying nucleus as $\tau \equiv \lambda^{-1}$, and noting that the half-life $t_{\frac{1}{2}}$ of the decaying nucleus is given by $t_{\frac{1}{2}} = \tau \ln 2$,

A.2. Fermi's theory of beta decay

Eq. (A.4) leads to

$$f(Z, \epsilon_0)t_{\frac{1}{2}} = \ln 2 \frac{2\pi^3 \hbar^7}{g^2 m_e^5 c^4} \frac{1}{|M_{fi}|^2}. \quad (\text{A.5})$$

Values of $f(Z, \epsilon_0)$ are tabulated in the literature[248, 249, 250].

The constant g represents the strength of the β -decay process and can be determined from Eq. (A.4), provided $|M_{fi}|^2$ is known[249, 250]. In some simple cases (known as “superallowed” transitions, e.g., the decay of the free neutron[248]; see below) $|M_{fi}|^2$ can be calculated, and the coupling constant is found to be[250] $g = 1.435 \times 10^{-62} \text{ J m}^3$. When expressed as a dimensionless value the strength is $\sim 10^{-5}$. For the sake of comparison, take the strength of the strong interaction to be 1. Relative to this, the strength of the electromagnetic interaction is $\frac{1}{137}$, while the strength of the weak (β -decay) interaction is only 10^{-5} , hence the use of the adjective “weak” in describing this interaction[249]. The constant g governs not only the β -decay processes, but many others as well, such as the decay of the muon[248, 250]: $\mu^\pm \rightarrow e^\pm + \nu_\mu + \bar{\nu}_\mu$.

From Eq. (A.4) it can be seen that $f(Z, \epsilon_0)t_{\frac{1}{2}} \propto 1/|M_{fi}|^2$. The quantity on the left is often more simply written as ft and is referred to as the “comparitive half-life”[248, 250]. The ft value can be considered as the reduced half-life corrected for differences in Z and ϵ_0 [[248, 250]]. Small ft values correspond to large matrix elements and indicate some transitions are more favoured, or more “allowed” than others. This gives rise to the notion of selection rules for β -decay transitions that are related to the ft value. Since β -decay half-lives range from fractions of a second to years, the transitions are grouped according to $\log(ft)$ values (Table A.1). The $\log(ft)$ ranges are classified according to transition probability; the larger $\log(ft)$, the greater the reduction in transition probability. The similarity with the selection rules for electromagnetic transitions is noted[250], recalling that Fermi's β -decay theory is based on that of the electromagnetic interaction.

The allowed (or forbidden) character of a transition is obtained from consideration of the parity of the parent and daughter nuclear wavefunctions, *and* the change in nuclear spin ΔI , if any, between the parent and daughter

A.2. Fermi's theory of beta decay

Table A.1: General classification of beta decay transitions[249].

Type	$\log(ft)$
Superallowed	~ 3
Allowed	4–6
First forbidden	6–10
Second forbidden	10–13
Third forbidden	> 15
Fourth forbidden[248]	~ 23

nuclei. Thus, for β -decay, wavefunction parity and angular momentum form the basis of the selection rules.

The first aspect arises because integrals in $|M_{fi}|^2$ over the parent and daughter wavefunctions have non-zero overlap only if the parity of the wavefunctions is unchanged, and vice-versa[249]. The second aspect arises in considering restrictions on the value of the total angular momentum of the leptons, recalling both the electron and neutrino have intrinsic spin of $\frac{1}{2}$. The transition probability is greatest when the lepton wavefunctions at the position of the nucleus $[\psi_e(0)$ and $\psi_\nu(0)]$ that enter into \mathcal{H}_{fi} have the greatest magnitude. A wavefunction of orbital angular momentum l behaves as $(R_n/\lambda_C^e)^l$ near the origin[251], where R_n is the nuclear radius ($\sim 10^{-15}$ m) and λ_C^e is the Compton wavelength of the electron (3.9×10^{-13} m). Thus, the probability that the emitted leptons carry orbital angular momentum is small and decreases rapidly with increasing l . The lepton wavefunctions will be greatest at the origin for $l = 0$ when the leptons are emitted with zero orbital angular momentum, i.e., “ s -wave state” electrons and (anti)neutrinos[248, 250]. However, for a relativistic particle, l is not a constant of motion, but j the total angular momentum is[250]. The most allowed transitions therefore occur when the leptons are emitted with a minimum of orbital angular momentum $j_e = j_\nu = \frac{1}{2}$ [251].

The total amount of angular momentum carried away by the electron and the neutrino is 0 if they are emitted with spins antiparallel, and it is 1 if they are emitted with spins parallel[250]. The former is a singlet state,

A.2. Fermi's theory of beta decay

while the latter is a triplet state. In the case of singlet lepton emission the spin of the nucleus cannot change, so

$$\Delta I = 0 \tag{A.6}$$

without a change of wavefunction parity. This selection rule was proposed by Fermi, F-transition[248, 249, 250]. If the leptons are emitted in a triplet state

$$\Delta I = \pm 1, 0, \text{ but } 0 \rightarrow 0 \text{ forbidden} \tag{A.7}$$

again without a change in wavefunction parity. This selection rule was proposed by G. Gamow and E. Teller, GT-transition[248, 249, 250].

The F and GT selection rules are not mutually exclusive[250]. For instance, the decay of the free neutron mentioned above is a $\frac{1}{2}^+ \rightarrow \frac{1}{2}^+$ transition ($I_i = I_f \neq 0; \Delta I = 0$) and so a mixture of F and GT processes contribute. Thus, in lowest order[249] $|M_{fi}|^2 = |M_{fi}(\text{F})|^2 + \frac{g_{\text{GT}}^2}{g_{\text{F}}^2} |M_{fi}(\text{GT})|^2$. The $0^+ \rightarrow 0^+$ superallowed decays are uniquely F-transitions, and from their study $g_{\text{F}} = g$ can be determined[249]. From the best determinations of the coupling constant strengths $\frac{g_{\text{GT}}}{g_{\text{F}}} = -1.259(4)$ [249].

The transitions classified as forbidden take place via the emission of non- s -state leptons[248], because l cannot be restricted to zero[251]. The emission of leptons with non-zero orbital angular momentum arises from the fact that they are not emitted from a point source, but rather the finite volume of the nucleus must be considered. The wavefunctions $\psi_e(0)$ and $\psi_\nu(0)$ must be evaluated over the entire nuclear volume and this introduces p -, d -, and higher-wave states into the emission[248, 250]. As stated above, as l increases, the probability of the β -transition rapidly decreases, and so transitions with $l = 1, 2, 3, \dots$ are classified as first, second, third, \dots forbidden transitions[248]. These transitions require that higher order terms be considered in the expansion of the plane waves used for the lepton wavefunctions

$$e^{i\mathbf{k}\cdot\mathbf{r}} = 1 + i\mathbf{k}\cdot\mathbf{r} - \frac{(\mathbf{k}\cdot\mathbf{r})^2}{2} + \dots \tag{A.8}$$

Thus, the second term in Eq. (A.8) corresponds to $l = 1$, and if it is this term

that is important in the interaction causing the transition, the leptons are emitted in a p -wave state; the parent and daughter nuclei must have opposite parity[248, 250]. The higher order terms of the plane waves introduce powers of p_e and p_ν into the matrix element[250]. Consequently, the matrix element is no longer independent of the energy partition between the electron and the (anti)neutrino (as it is for allowed transitions)[248], and so the shape of the β spectrum for forbidden transitions is different from that of the typical, allowed Fermi spectrum[250].

A.3 Parity violation in beta decay

The nonconservation of parity in β -decay was an important discovery and is an aspect of this type of radioactive decay that is crucial to the implementation of the β -NMR technique. Processes governed by the weak interaction (like β -decay) have nonconservation of parity in common, and this is a major distinction between the weak interaction and the electromagnetic and strong interactions as parity is conserved for processes involving the latter two alone[250]. Parity (non)conservation can be described at various levels of sophistication. One simple description is that if the mirror image of a phenomenon is also a physically realizable phenomenon, then parity is conserved[250]. Thus, parity conservation implies space-reflection symmetry holds for a given phenomenon.

Consideration of space-reflection symmetry to the β -decay process requires the distinction of two types of vector quantities. Space-reflection of a given point is equivalent to inversion of the coordinates through the origin, i.e., $(x, y, z) \rightarrow (-x, -y, -z)$ [248, 250]. Vectors for which this change of sign of space coordinates occurs are called “polar” vectors, examples of which are linear momentum and electric field[248, 250]. On the other hand, vectors such as angular momentum or magnetic field are characterized not only by direction, but also by a screw sense or handedness, and they do *not* change sign under inversion[248, 250]. Vectors of this second type are termed “axial” vectors (or “pseudovectors”).¹³ The product of any

¹³Axial vectors do not change sign because they are the result of the cross-product of

two axial vectors, or of any two polar vectors, is a number called a scalar; such quantities are invariant under reflection/space inversion[248, 249, 250]. However, the scalar product of an axial vector and a polar vector is a number that *does* change sign under reflection/inversion; these quantities are called “pseudoscalars”[248, 249, 250]. Any observed quantity resulting from a physical measurement may be a scalar or a pseudoscalar, but for parity to be conserved reflection symmetry must hold (object and image be indistinguishable[250]), and this requires that all pseudoscalar quantities vanish[248, 249, 250]. Thus, the observation of a non-zero pseudoscalar quantity indicates nonconservation of parity; however, nothing can be said about parity conservation until a pseudoscalar has been measured[250].

In 1956 Lee and Yang pointed out that none of the experimental data on the weak interaction could address the question of parity conservation since all the experiments up to that point were designed to measure scalar quantities[248, 249, 250]. The first experiment specifically designed to observe a pseudoscalar quantity in β -decay was the experiment of Wu *et al.* in 1957 using spin-polarized ^{60}Co nuclei[248, 249, 250]. In this historic experiment the expectation value of the pseudoscalar $\langle \mathbf{p}_e \cdot \mathbf{J}_n \rangle$ was measured, where \mathbf{p}_e is the velocity of the β -electron (polar vector), and \mathbf{J}_n the nuclear spin (axial vector)[249, 250]. The ^{60}Co nuclei had their spins aligned parallel by an external magnetic field at very low temperature (~ 10 mK[249, 250]). The β -electron emission in the decay to ^{60}Ni ($5^+ \rightarrow 4^+$ GT-transition[249]) was observed to be preferentially *opposite* to the nuclear spin direction[248, 249, 250]. Thus, the observed β -ray asymmetry established the pseudoscalar $\langle \mathbf{p}_e \cdot \mathbf{J}_n \rangle$ was non-zero, thereby proving nonconservation of parity in β -decay (weak interaction)[248, 249, 250]. The experiment is shown pictorially in Fig. A.2(a). In the case of β^+ -decay, the positrons are emitted preferentially in the same direction of the nuclear spin[252].

The ^{60}Co experiment was later repeated by Chirovsky *et al.* with the purpose of measuring the scalar product of two vectors that *do* change sign under inversion, and so the components of the resulting vector are left unchanged by the inversion[250].

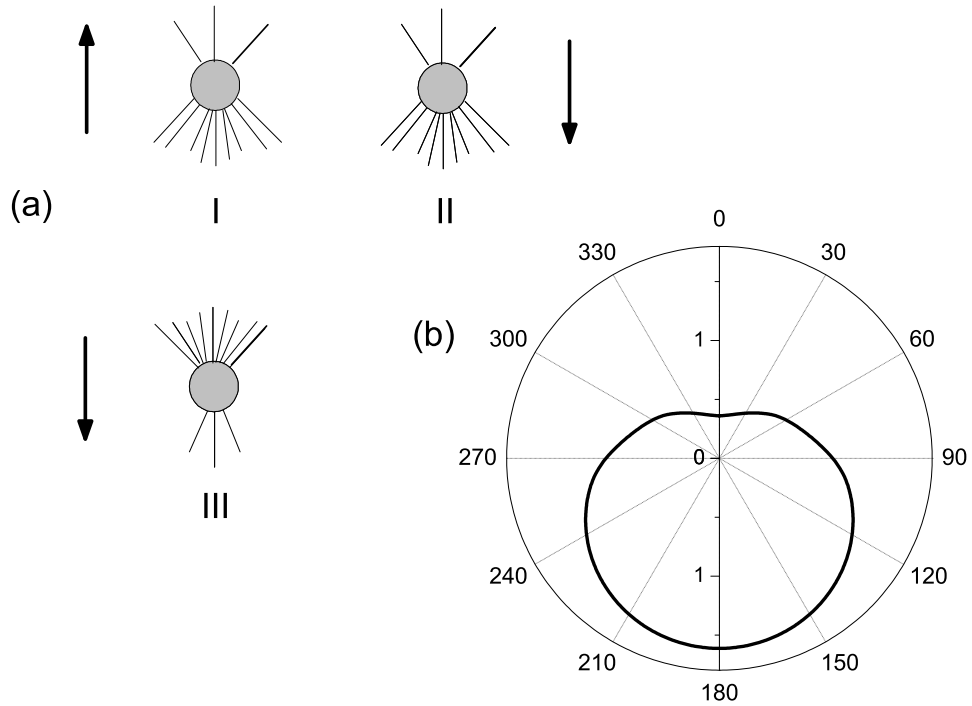


Figure A.2: (a) Diagrammatic illustration of parity violation in β -decay. A sample of β -emitters is contained in the grey spheres and their nuclear spins are oriented at low temperature in the direction of an external magnetic field represented by the heavy arrows. The anisotropy of the emitted electrons is represented by the the lines. The mirror image of I is shown in II, and III results from I being flipped by 180° . Space-reflection symmetry does not hold as II is *not* an experimentally realizable process, while III is. (b) Polar diagram representation of the β -electron intensity as a function of the angle θ relative to the nuclear polarization direction. The solid curve is generated by Eq. (A.9) for the arbitrary case of $\mathcal{A} = -1$ and $\frac{v_e}{c} = P = 0.8$. Adapted from Ref. [249].

A.3. Parity violation in beta decay

pose of measuring the angular asymmetry of the β -electron distribution[253]

$$N_{\beta}(\theta) = 1 + \mathcal{A}P\left(\frac{v_e}{c}\right) \cos \theta. \quad (\text{A.9})$$

$N_{\beta}(\theta)$ stands for the β -electron intensity as a function of the angle θ with respect to the nuclear polarization vector, $\frac{v_e}{c}$ is the ratio of the velocity of the β -electron to the speed of light, P the polarization of the nuclei, and \mathcal{A} is the beta-spin correlation or asymmetry coefficient. The parameter \mathcal{A} depends on the parent nucleus, i.e., the specific interaction causing the decay[250]. For the case of ^{60}Co , $\mathcal{A}_{\text{theory}} = -1$, and the experimental results are in excellent agreement, giving $\mathcal{A}_{\text{exp}} = -1.01(2)$ [253]. As an illustration of the directional anisotropy of the β -radiation from an oriented nucleus, $N_{\beta}(\theta)$ is shown in Fig. A.2(b) for $\mathcal{A} = -1$ and 0.8 for the other two terms. The fundamental origin of parity violation is still not fully understood, and β -decay experiments continue to provide details into parity violation for the weak interaction[252]. Experiments of the type described above for ^{60}Co are usually conducted using a β -source in the form of a solid sample, and as such are limited in precision due to effects of scattering or magnetic deflection on the β -particle trajectories[252, 253]. Modern experiments aim to overcome this limitation by using magneto-optic traps to confine “clouds” of spin polarized β -active atoms, thereby allowing quantities such as \mathcal{A} to be extracted with even greater precision[252]. Since the ^{60}Co experiment of Wu *et al.* several other experiments have corroborated nonconservation of parity in the weak interactions; for these processes nature can distinguish between right and left[248].

Parity-nonconserving terms were omitted from the Hamiltonians for the weak interactions until experiment showed they must be included[250], highlighting the historical importance of such experiments. It was by analogy to the strong and electromagnetic interactions that these terms were initially omitted[250]. For instance, in equations for the energy of the electromagnetic field, scalar terms such as \mathbf{H}^2 and \mathbf{E}^2 are allowed, but a term such as $\mathbf{H} \cdot \mathbf{E}$ is a pseudoscalar which is not permissible (as it would change sign under inversion)[250]. As mentioned, Fermi constructed his theory of β -decay

by analogy to the electromagnetic interaction, and so the theory described in Sec. A.2 is formulated on the assumption that parity is conserved[250]. However, it is important to note that the main results of Fermi’s theory regarding β spectra shapes and lifetimes are essentially unaffected by the nonconservation of parity since his calculations involve only scalar quantities[248, 250].

A.4 Decay of ${}^8\text{Li}$

The β -emitter ${}^8\text{Li}$ is used for the present β -NMR experiments. Some physical properties of this nucleus are given in Table A.2. It decays according to



The ground state of the ${}^8\text{Li}$ nucleus is of spin 2^+ and it decays to a 2^+ excited state of ${}^8\text{Be}$ that is situated 2.9 MeV above its ground state[254]. This decay is thus allowed by both F and GT selection rules (Sec. A.2); however, as discussed below, it is dominated by the strength of the GT coupling[254]. The value of E_0 for this decay is 13.1 MeV and $\log(ft) = 5.4$ [254], and is thus an “allowed” transition. An advantage in using ${}^8\text{Li}$ for β -NMR experiments is that the high energy β -electrons are easy to discriminate from low energy background radiation[254].

The excited daughter ${}^8\text{Be}$ nucleus can relax to the ground state by the emission of gamma radiation, after which it promptly disintegrates into two α -particles (${}^4_2\text{He}$ nuclei). The ${}^8\text{Be} \rightarrow 2\alpha$ decay is termed “prompt” as $t_{\frac{1}{2}}$ is just 7×10^{-17} s[255]. This means the daughter nuclei do not remain in the sample which is another advantage of using ${}^8\text{Li}$ for β -NMR.

The ground state of ${}^8\text{Li}$ is a member of the isospin triplet: ${}^8\text{Li}$, ${}^8\text{Be}$, ${}^8\text{B}$ [254]. The concept of isospin (or isobaric spin) T is used in nuclear structure models and is based on the idea that the force acting on the proton and neutron is independent of charge and therefore the two nucleons can be considered as different quantum states of a single particle[248]. This is analogous to the quantum mechanical description of the two spin states of the electron, i.e., “spin-up” or “spin-down.” Just as the electron may be assigned

A.4. Decay of ${}^8\text{Li}$

Table A.2: Physical properties of the ${}^8\text{Li}$ nucleus.

Quantity	Symbol	Value
Nuclear spin	I^π (units of \hbar)	2^+
Lifetime	τ	1.21 s
Half-life	$t_{\frac{1}{2}} = \tau \ln 2$	0.839 s
End-point energy of decay	E_0	13.1 MeV
Gyromagnetic ratio	${}^8\gamma/2\pi$	6.3015 MHz/T
Electric quadrupole moment	Q/e	+31 mb[167]

to either of these spin states ($+\frac{1}{2}$ or $-\frac{1}{2}$), the z component of the isospin T_z of each nucleon may be assigned in a similar manner: the $+\frac{1}{2}$ state is taken to correspond to the neutron, and the $-\frac{1}{2}$ state is taken to correspond to the proton[248]. A pair of neutrons(protons) gives $T_z = +1(T_z = -1)$, and $T_z = 0$ for a neutron-proton pair.

A simplified description of the ${}^8\text{Li} \rightarrow {}^8\text{Be}$ decay in terms of isospin can be seen by considering the numbers of neutron-proton pairs in the parent and daughter nuclei: $(5n, 3p) \rightarrow (4n, 4p)$, or in terms of total T_z , $\sum T_z = +1 \rightarrow \sum T_z = 0$. Thus, $\Delta T_z = -1$ and the transition is allowed by the GT selection rule. Indeed, this is reflected in the relative strength of the matrix elements as M_F is only $\simeq 3\%$ of M_{GT} [254].

Appendix B

Ion Implantation in Metals

B.1 General concepts of ion implantation in solids

The processes governing the implantation of ions into solids (or passage through them at sufficient energies) are complex, but generally well-understood as this subject has been intensely studied since the early twentieth century[256, 257]. The earliest theoretical considerations of the stopping (slowing down) of a projectile ion into a solid have evolved into modern computer simulation programs that are both fast and quite accurate. Experiments on the stopping of ions in solids provided data with which to test theories or aid in computer simulation, and have given way to two major technological applications of ion implantation: microanalysis and controllable modification of materials. Ion implantation allows for reproducible modification of surface and near-surface properties of materials and is used frequently in device fabrication. For example, it can be used to form alloys of desired compositions without the loss of crystal structure and does not suffer from potential miscibility problems associated with other alloying techniques[258]. An important example is the introduction of selective concentrations of dopant atoms into semiconductors. On the other hand, high-energy ion bombardment of materials can be employed to impart desired degrees of disorder to a crystal, transform a crystalline lattice into a fully amorphous state, or create regions of intermixing at the interface of two dissimilar crystals[258]. Ion implantation can also be used to create nanometer sized clusters embedded in various hosts to form nanocomposite materials[259], while both ion implantation and irradiation can be employed for topographical patterning of

materials[260]. Ion beams— especially those of protons or α particles— are also used to analyze the composition of materials as a function of depth below the surface, for example, Rutherford backscattering spectrometry[261].

The ^8Li ions used in these β -NMR experiments do not remain in the samples (nor do the daughter nuclei; see Appendix A); however, the processes by which they lose energy and eventually stop in the hosts are important to consider. In this Appendix, the mechanisms of ion implantation are briefly summarized— mostly qualitatively. As well, the possible types of damage that may be produced during the implantation are summarized. In the final Section the computer simulation program TRIM.SP that has been used to obtain the $^8\text{Li}^+$ stopping distributions for the studies in this thesis is reviewed. In keeping with the topic of this thesis, the present survey focuses on implantation into metallic hosts.

Two important aspects to consider are the scattering of the projectile ion by collisions with the host atoms, and the energy transferred from the former to the latter. These in turn affect the overall path length (i.e., mean stopping depth) of the implanted ion, and the degree of damage to the host. The two major modes of energy loss for the incident ions are the direct collisions with the host nuclei, and the excitation of the electrons of the host. Both of these processes are energy-dependent and so make varying contributions along the path of the ion x : $(dE/dx)_{\text{loss}} = (dE/dx)_{\text{nucl}} + (dE/dx)_{\text{elec}}$. An overview of these two processes is given next, then more details are provided in regards to the particular computer simulation program employed here.

The dominant mode of energy loss for implanted ions with energies less than ~ 0.5 MeV (pertinent to β -NMR) is through the elastic interactions with the target nuclei. These nuclear collisions give rise to “Rutherford scattering” as the electrostatic Coulomb repulsion from the screened nucleus will deflect the ion. Being elastic in nature, both energy and momentum are conserved, and these collisions are treated as two body events in a centre-of-mass coordinate system. The important parameters being the energy lost by the impinging ion, the cross-section for the energy transfer, and the scattering angle Θ . If the mass of the impinging and target atoms differs significantly, the scattering angle is small.

An important consideration in the evaluation of nuclear collision events is the choice of the interatomic potential $V(r)$, where r is the interatomic separation. This repulsive potential is chosen such that the particles can be assigned a definite radius, and thus predict Θ . The earliest treatments used analytical expressions for $V(r)$, typically containing a $1/r$ Coulombic term multiplied by a screening term. As there is no definitive expression for $V(r)$ that is appropriate for all ion pairs at all energies, these functions are often modified through the addition of empirically adjustable parameters. With the advent of the computer, descriptions of $V(r)$ spanning a wide range of r can now be made numerically. Both head-on and glancing angle collisions are considered by defining a total cross-section for energy transfer; the probability of energy transfer (loss) for a given scattering angle can then be related to the total cross-section.

The electronic energy losses occur through inelastic interactions with the electron clouds of the target. As the energy of the impinging ion increases, the energy loss due to elastic (nuclear) collisions decreases (essentially $\propto 1/E$), and the inelastic (electronic) events dominate. At high velocities, the projectile ion is fully stripped of its electrons. This occurs when the ion's velocity is greater than the Bohr velocity of the target atom electrons. In this regime, the rate of energy loss is related to the closeness of the ion to the target atoms and thereby the number of electronic excitations it can produce, i.e., proportional to the degree of "penetration" through the target electron shells. The electronic energy losses do not cause significant deflection of the ion. It is emphasized that this type of energy loss is important for ion energies greater than hundreds of keV/amu, and so makes little contribution to the much lower energy ${}^8\text{Li}^+$ stopping in the studies of this thesis.

Upon considering the above mechanisms for energy loss of a projectile ion, the total distance (path length) travelled by the ion until it is brought to rest in a given target can be predicted. This is expressed through the *mean range* R and the *range straggling* ΔR . First, it is noted that overall a crystalline target may be treated in a similar fashion as an amorphous one. The reason for the similarity is because the range is determined by averaging over many individual events. The range is defined as the mean

depth from the surface at which the ion stops.¹⁴ The random nature of the interactions experienced by an ion as it penetrates a solid causes fluctuations in the energy lost per collision, as well as the total number of collisions over the path length. This imparts a “spreading” of the energy of the initially monoenergetic ions resulting in a scatter of the stopping distance of individual ions about R . This distribution is classified as range straggling, and it generates implantation profiles that have an overall quasi-Gaussian shape, especially when the projectile ion is of lower mass than the target (e.g., ^8Li in transition metals). As an example, R and ΔR are shown in Fig. B.1 for the $^8\text{Li}^+$ implantation profile in a 100 nm Au film on MgO (obtained using TRIM.SP; see below).

An important distinction between the ranges of ions implanted into amorphous and crystalline targets is the effect of channeling[256]. This phenomenon is also well understood. Channeling results in a more extensive R for ions than would be predicted, but this only occurs when the incident beam is aligned parallel to certain high symmetry directions of the crystal. The atomic rows and planes of a single or polycrystalline target can act as walls that effectively “steer” the ion deeper into the target compared to random collisions. As channeled ions do not suffer the same reduction in energy from nuclear collisions along their trajectories, R can be an order of magnitude larger than in the absence of channeling. Carefully focused beams with small angular divergence are required as the incident beam must be aligned to within a *fraction of a degree* of a crystalline axis for channeling to be significant. Thus, for ion implantation in general, the relative fraction of ions that will become channeled is minor unless specific attempts are made to direct the beam along a channeling direction. It is possible that during random collisions ions may be deflected into a channel, and this is characterized as quasi-channeling. Briefly, in channeling theory the target atoms are treated as stationary, and the average of the individual collision events

¹⁴This range is technically the projected range R_p , the average depth an ion will penetrate for the incident beam normal to the target surface. The total range R_t , or the total path length of the ion’s trajectory is generally larger than R_p due to the possible in-plane (lateral) spreading of the beam R_\perp . R_t is given by the hypotenuse of the right-angled triangle formed by R_p and R_\perp .

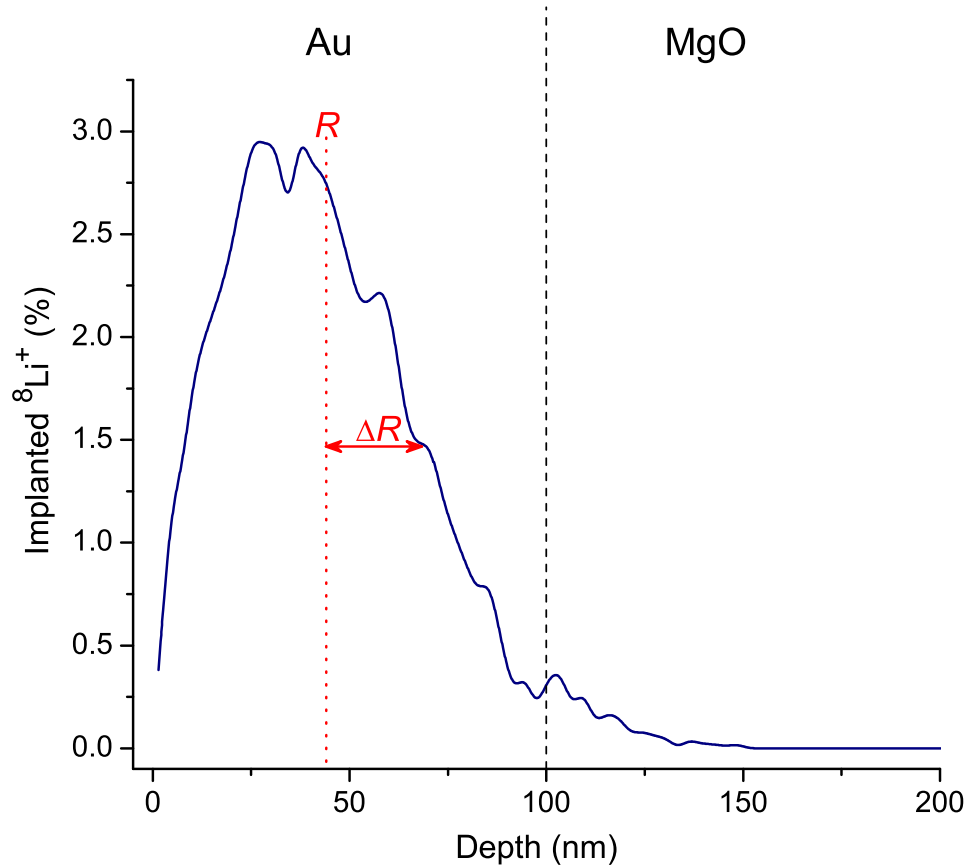


Figure B.1: Stopping profile for 13 keV $^8\text{Li}^+$ implanted into a 100 nm Au film on MgO. The mean range $R = 44$ nm, and the range straggling $\Delta R \sim \pm 25$ nm. The small peaks in the curve are numerical noise due to the relatively small number of particles used in the simulation (1×10^4).

is treated by replacing the rows of atoms by a continuous potential; yet, precise predictions of R for channeled ions is difficult. Empirical corrections to R determined for amorphous targets are often necessary.

B.1.1 Damage produced by ion implantation

As stated above, during the elastic nuclear collisions a projectile ion will scatter off of the target atoms, and in doing so transfer some of its kinetic energy to them over the length of the implantation trajectory, as well as generate local heating. The energy may be sufficient to displace an atom of the target material, disrupting the atomic order and impart some degree of disorder to the lattice[188, 256]. This perturbation caused by the implanted ion is referred to as radiation damage. The response of the target lattice is a dynamic event, and at a given temperature, the perturbed atoms may rearrange (relax) into various defect structures. Often these radiation-induced defects may result in superior mechanical properties for a given material over the original lattice, and may be thermodynamically difficult to produce by other processing techniques. The disordered region is limited to the region surrounding the implantation track. Just as the ranges of ions in solids have been extensively studied for many years, so too have the effects of radiation damage.

There are two broad classes of defects that result from radiation damage. The first involves one or two disrupted target atoms. These are therefore analogous to the point defects encountered normally in solids, i.e., vacancies and interstitials. A vacancy is simply a missing atom (or ion) in a lattice, and at finite T , there is always a thermodynamic equilibrium concentration of such vacancies in otherwise “perfect” crystals as the entropy of the lattice is increased by the presence of disorder[3]. For metals the energy required to form a monovacancy E_{v1}^f is typically 1 – 2 eV. As specific examples, E_{v1}^f for Au is ~ 0.9 eV, while for Pd it is ~ 1.8 eV. The probability of a vacant lattice site is given by the Boltzmann factor at thermal equilibrium[3] ($\exp[-E_{v1}^f/k_B T]$). For $E_{v1}^f = 1$ eV at 1000 K, the equilibrium concentration of vacancies is $\simeq 10^{-5}$, which for one mole of atoms is $\sim 10^{18}$ lattice sites.

There are two types of vacancy defects: (i) the Schottky defect is a lattice vacancy in which the missing atom is considered to be transferred to the surface of the crystal; (ii) in the Frenkel defect the missing atom is moved into an interstitial lattice site not normally occupied by an atom. For this latter defect the vacancy-interstitial pair thus remain in the bulk of the crystal. The interstitial is an important defect as it perturbs the surrounding lattice rather strongly and can significantly affect bulk properties. Vacancies also provide a means for thermally-activated atomic transport in pure materials.

Much of the knowledge of the properties and behaviour of complex defects in metals has come from the study of point defects. Since vacancies can be formed at high temperatures, they may be studied under thermal equilibrium conditions by heating a sample, often to just below the melting point. The high temperature concentration can then be quenched, or “frozen” into the sample by rapid cooling. Point defects produced by quenching or irradiation are formed under non-equilibrium conditions and are metastable as they can be thermally annealed out of the sample. At certain temperatures particular defects begin to migrate and can form complexes, undergo annihilation reactions, or become trapped at grain boundaries, dislocations, impurity atoms, etc. In simple metals, the interstitial defect generally becomes mobile at low temperatures (less than about 50 K), while for vacancies this is nearer to room temperature.

A vast amount of data on the annealing properties of defects in metals has come from measurements of the electrical resistivity. The “recovery curves” for many metals exhibit general features that are quite similar. Using copper as the prototype, the annealing of metals has been divided into three principle characteristic stages, that are subdivided into five (I–V). It should be noted that annealing of defects in insulators often corresponds to these stages as well; however, in non-metallic systems, the charge state of the lattice plays an important role in defect formation and stability. For example, stage I (which itself is subdivided into five stages) is described by interstitial migration and recombination with vacancies, while stage III corresponds to vacancy migration and agglomeration. Finally, although much information has been obtained from resistivity measurements, techniques

like NMR, X-ray spectroscopy, and electron microscopy have further contributed to the understanding of defect formation and dynamics.

The collisions between a projectile ion and the target atoms often result in the displacement of the target atom from its regular lattice site creating an interstitial and a vacancy, i.e., a Frenkel defect, or what is commonly called a Frenkel pair. The displaced atom is referred to as the primary knock-on atom (PKA), and it may in turn lose the energy transferred to it by displacing other target atoms from their lattice sites. This gives rise to the concept of “radiation damage cascades.” However, because these damage cascades are formed under dynamic, non-equilibrium conditions, the target lattice may not relax and the energy required to displace an atom is greater than the equilibrium E_{v1}^f . Instead, the threshold energy for atom displacement E_d must be considered. For most metals E_d is usually in the range of $\approx 20\text{--}50$ eV, and it is frequently both temperature- and orientation-dependent[262, 263]. Values of E_d are directly measurable using high voltage electron microscopy. If the energy transferred to a PKA is less than E_d , the atom is not displaced and the energy goes into lattice vibrations.

B.2 Simulations of $^8\text{Li}^+$ implantation profiles using TRIM.SP

Computer simulations of ion implantation based on the binary collision approximation using Monte Carlo calculations are available that can yield ion range distributions for multilayered targets over a wide energy range[257]. One such program is TRIM (TRansport of Ions in Matter). A variation of this code called TRIM.SP (the SP stands for sputtering)[265] has been used to obtain the $^8\text{Li}^+$ stopping distributions for the β -NMR studies in this thesis. In this Section a brief summary of the basics of the TRIM methodology is given[264]. The program provides high computer efficiency without sacrificing accuracy. It uses a specially developed analytical formulae to account for the nuclear scattering. As it uses a Monte Carlo method it can

more rigorously treat the elastic scattering events and explicitly treat surfaces and interfaces (the latter two being difficult to account for in analytical treatments based on transport theory).

The simulations consist of following a large number of individual ions (particles) in a specified target. These are referred to as “histories.” For each history a particle is assigned an energy, a direction and starting position. The path of the particles is changed as a result of nuclear collisions, while they are assumed to move in straight free-flight paths between collisions. The particles lose energy as a result of the nuclear and electronic mechanisms, and the program is valid for incident ions with energies in the range of 0.1 keV to several MeV. TRIM considers the target to be completely amorphous with atoms in random positions (but maintaining a density specified by the user), and so can not account for things such as channeling, isotopic distributions, or variations in stoichiometry (where applicable). Recall that overall range distributions for crystalline and amorphous materials are similar as it is the average of many particles undergoing many random collisions that is important. The program provides data on implanted, reflected and transmitted particles for planar targets.

Nuclear scattering is important for energy loss, but it also dominates the spatial distribution of the ions as the trajectories are little deflected by electronic loss events. This involves solving the scattering integral for Θ that is dependent on $V(r)$. Numerical solutions to this are not practical for large numbers of histories or for personal computers. Instead the authors of the TRIM code have developed a universal interatomic potential that is a single analytic function. The universal $V(r)$ adopted is then used in the calculation of Θ by means of a formula that contains five fitting coefficients. These fitting coefficients can be found for any choice of $V(r)$, not just their universal one. The authors report the 5-coefficient formula fits to within 2% of the full scattering integral. The energy transferred during a collision is proportional to Θ and the masses of the particle and target atoms.

The electronic and nuclear energy losses are taken to be independent of one another. The neglect of correlations between the two increases computer efficiency and does not drastically affect the mean (projected) range results

B.2. Simulations of ${}^8\text{Li}^+$ implantation profiles using TRIM.SP

for low-energy, light ions. The incident particles lose energy in discrete amounts in the nuclear collisions, but lose energy continuously from the electronic interactions as the electrons act like a dissipative “fluid.” The solid (target) is treated as an electronic plasma of appropriate density. The electronic energy loss is proportional to the product of the distance traveled between collisions and the electronic stopping cross-section. The authors develop this using Lindhard’s approach to the perturbation of a charged particle in an initially free electron gas of uniform density using density functional theory. The electronic stopping power was determined for protons in the plasma. This was used to obtain heavy ion stopping cross-sections by means of the “scaling” formalism in which heavy ion stopping powers scale proportional to proton stopping powers for identical velocities and targets.

As mentioned above, free surfaces or interfaces present no problems for Monte Carlo simulations, and TRIM.SP can easily handle multilayered targets consisting of up to seven layers. The maximum thickness of a given layer allowed is 5,000 nm. So, for the TRIM.SP simulations of the substrates studied in this thesis, only the top-most 0.005 mm are considered. Two types of TRIM.SP results for ${}^8\text{Li}^+$ (particle of mass 8, charge +1) implanted into Pd films are shown in Fig. B.2.

For the purposes of β -NMR, the TRIM.SP simulations are quite satisfactory. For example, predictions of the maximum E_{Li} for which only a resonance from Li ions stopping in the metal layer will be observed [like that shown in Fig. B.2(a)] is generally good to within a few keV. Again, the simulations do not take channeling into account. Also, real samples may not be continuous, or may not be of uniform thickness. The predictions of TRIM.SP for ${}^8\text{Li}^+$ implantation into Pd are summarized in Fig. B.3, where quadratic interpolation curves have been added parameterizing R and ΔR as a function of E_{Li} . Note the implantation distributions become narrower as E_{Li} is reduced.

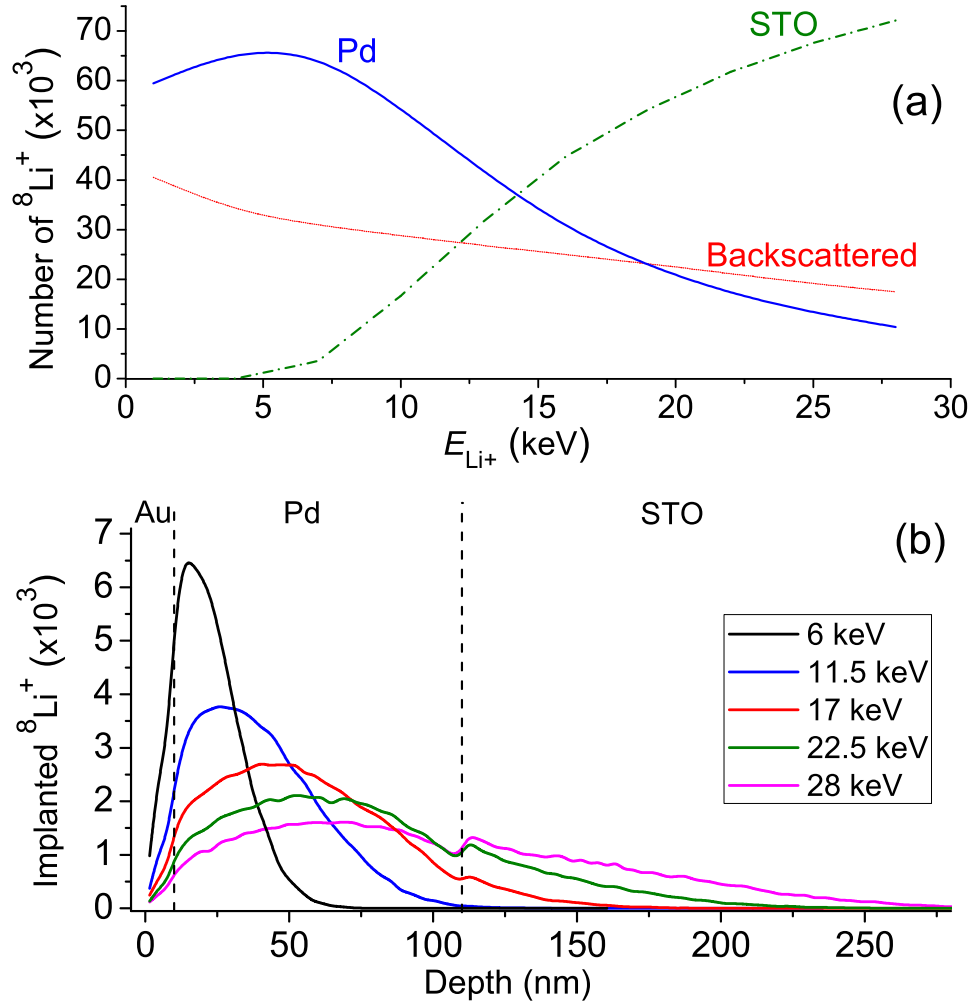


Figure B.2: Examples of results from TRIM.SP simulations of $^8\text{Li}^+$ implantation into Pd films. (a) Fraction of ions predicted to be implanted into the metal or substrate, and those that are backscattered as a function of ion energy for 50 nm of Pd on STO. (b) Range profiles in Au(10 nm)/Pd(100 nm)/STO for various implantation energies. In both (a) and (b), 1×10^5 particles were used in the simulations.

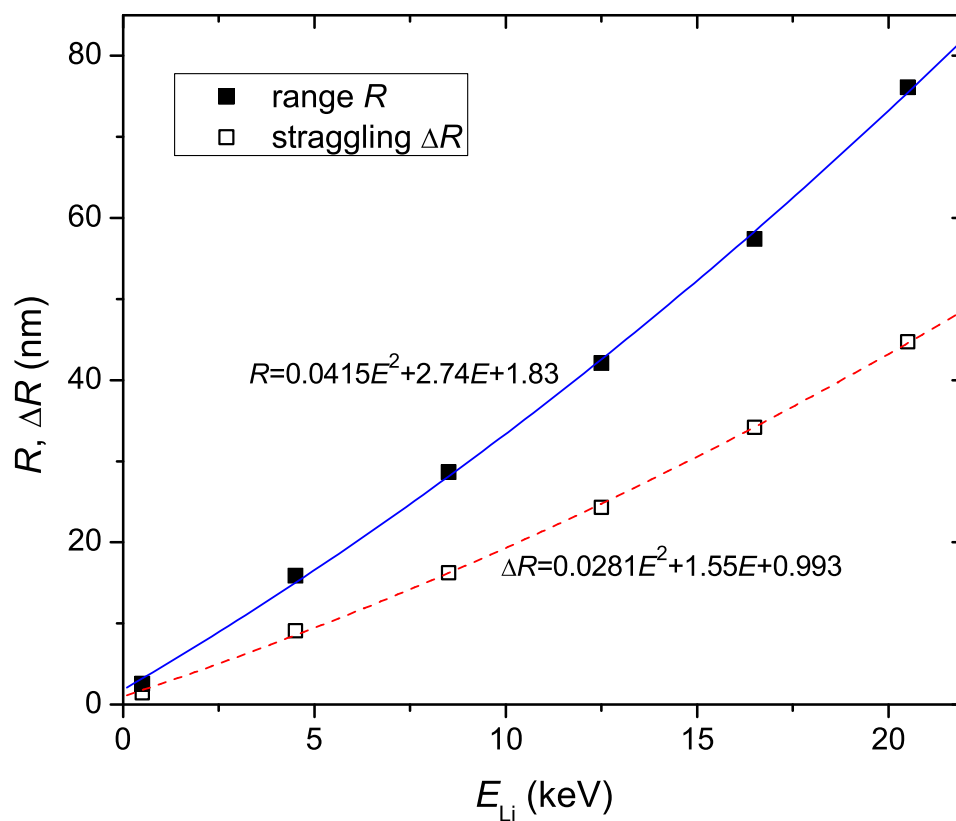


Figure B.3: Mean stopping range R and straggling ΔR of ${}^8\text{Li}^+$ implanted into Pd as a function of energy as predicted by TRIM.SP. Equations for the associated quadratic interpolation curves are indicated.